EVALUATION OF NANOCOMPOSITES AS LIGHTWEIGHT ELECTRONIC ENCLOSURES FOR SATELLITES' APPLICATIONS

THESIS

Benjamin T. Harder, Captain, USAF

AFIT/GMS/ENY/08-J01

DEPARTMENT OF THE AIR FORCE
AIR UNIVERSITY

AIR FORCE INSTITUTE OF TECHNOLOGY

Wright-Patterson Air Force Base, Ohio

AFIT/GMS/ENY/08-J01

EVALUATION OF NANOCOMPOSITES AS LIGHTWEIGHT ELECTRONIC ENCLOSURES FOR SATELLITES' APPLICATIONS

THESIS

Presented to the Faculty

Department of Aeronautics and Astronautics

Graduate School of Engineering and Management

Air Force Institute of Technology

Air University

Air Education and Training Command

In Partial Fulfillment of the Requirements for the

Degree of Master of Science in Materials Engineering

Benjamin T. Harder, BS

Captain, USAF

June 2008

AFIT/GMS/ENY/08-J01

EVALUATION OF NANOCOMPOSITES AS LIGHTWEIGHT ELECTRONIC ENCLOSURES FOR SATELLITES' APPLICATIONS

Benjamin T. Harder, BS

Captain, USAF

Approved: Date:

//signed// 30 May 08
Dr. Shankar Mall (Chairman)

//signed// 30 May 08
Dr. James C. Petrosky (Member)

//signed// 30 May 08
Dr. Som Soni (Member)

Abstract

The United States military is exploring the use of nanocomposite materials for satellite structural applications. Current composite spacecraft structures are nonconductive and must have expensive shielding materials applied in order to protect the spacecraft from catastrophic damage that can be caused by electromagnetic interference (EMI) and/or electrostatic discharge (ESD) which are characteristics of the space environment. Conductive nanocomposites are being developed for spacecraft structures that will provide ESD and EMI shielding protection without the need for expensive secondary shielding materials. This thesis studied one such material consisting of M55J/RS-3 composite combined with nickel nanostrands™. Four different configurations were tested for their ultimate tensile strength (UTS) and EMI shielding properties before and after exposure to the space environment. The four configurations tested were a baseline panel consisting of M55J/RS-3 and three configurations with different layers of nickel nanostrands™ added to the control specimen: exterior, interlaminar, and mid-plane. These four were further tested for their EMI and resistivity properties before, during and after monotonic tension tests of increasing loads up to fracture. This study found that the UTS and Young's modulus (E) do not change after exposure to the space environment, EMI shielding of the exterior specimen is 25% better than the control specimen, sheet resistance measurements show that exterior specimens are 11% better at ESD protection than the control, and failure mechanisms are the same regardless of composite configuration: The 90° plies failed first, causing delamination in the 0/90 plies leading to transverse matrix cracking and delamination in the ±45 plies resulting in ultimate failure, and in all configurations the nanostrand layers were not damaged.

Acknowledgements

I would like to thank my thesis advisor, Dr. Mall for his patience and guidance in completing this thesis. I would like to thank Dr. Petrosky and Dr. Farlow for their assistance with the space environment tests on my specimens. I would also like to thank Dr. Alexander for his assistance with the EMI shielding and resistance measurements of my specimens. Finally, I would like to thank my wife for believing in me and supporting my efforts to see my master's degree through to the end.

Benjamin T. Harder, Captain, USAF

Table of Contents

Page

Abstract…… iv

Acknowledgements……v

Table of Contents……...vi

List of Figures……viii

List of Tables……. xii

List of Symbols and Acronyms……..xiii

I. Introduction……1

II. Background……7

2.1 Overview and Challenges of the Space Environment……..7

2.2 Nanocomposites……...9

2.3 Radiation Environments and their Damage to Materials…….15

2.4 Summary……..17

III. Method of Experimentation……... 18

3.1 Introduction……..18

3.2 Specimen Preparation…….. 18

3.3 Monotonic Tension and Resistance Test Equipment and Procedures…. 21

3.4 EMI Test Equipment and Procedures…….. 25

3.5 Simulated Space Environment Test Equipment and Procedures…….28

3.6 Test Plan……...29

IV. Analysis and Results……..31

4.1 Introduction……..31

Page

4.2 Monotonic Tension and Resistance……. 32

4.3 EMI Shielding……..37

4.4 Simulated Space Environment…….41

4.5 Failure Mechanisms…….45

V. Conclusions and Recommendations…….. 59

5.1 Summary……..59

5.2 Conclusions……..60

5.3 Recommendations for Future Work…….62

Appendix A. Stress-Strain Curves of 15.25 cm (6 in) Specimens…….. 63

Appendix B. Stress-Strain Curves of 7.62 cm (3 in) Specimens…… 69

Appendix C. Additional SEM Micrographs and Photos……. 71

Bibliography…….. 80

Vita…….83

List of Figures

Figure Page

1. 200 nm Diameter Nickel Nanostrands™……..... 3
2. Cross-Sectional View of the Four Systems…… 5
3. Factors Affecting Spacecraft in the Space Environment [28]…… 7
4. Nanostrand lattice that has been compressed to about 20% volume solid [13]..11
5. Volume resistivity of nanostrands in polymers veil vs. mix [13]……...12
6. Specific conductivity (S/cm/gm/cc) of composites with black cloth or nickel coated cloth and neat resin or 5% nickel nanostrand resin [13]……. 13
7. A 625,000 volt discharge readily passes through a non-conductive composite at the left. But with the addition of 5% volume nanostrands to the resin, the same discharge is effectively controlled [13]……. 14
8. Electromagnetic shielding properties of nanostrands [13]……..14
9. Test Specimens, dimensions in cm……. 19
10. Soldering the M55J/RS-3 with exterior nickel nanostrands™……... 20
11. M55J/RS-3 with exterior nickel nanostrands™ tensile specimen…….. 20
12. MTS Machine……. 22
13. Keithly 2400 Source Measure Units……... 22
14. Typical Tension Test Procedure……. 24
15. Mechanical Testing Station…….25
16. EMI Testing Equipment……..26
17. Secondary Resistance Testing Equipment…….. 26
18. Space Environment Test Equipment……...29
19. Mounted Specimen in Beam Tube……..29

Page

20. M55J/RS-3 Composite Configurations……...32

21. Sheet Resistance Data…….35

22. Sheet Resistance Plotted Against Stress……. 36

23. Sheet Resistance Normalized to Control Specimen……36

24. EMI Attenuation Data…….38

25. EMI Attenuation Plotted Against Stress to Failure…….39

26. Normalized EMI Attenuation Data…….40

27. EMI Attenuation Pre- and Post-Exposure to Space Environment……..42

28. Modulus Comparisons…… 44

29. 15.25 cm Specimens After Testing…….46

30. Fractured Control Specimen: a) width view; b) thickness view at 100x; c) thickness view at 5x magnification…….46

31. SEM Picture of Control Specimen Origin of Fracture……47

32. Fractured Mid-Plane Specimen: a) width view; b) thickness view at 100x; c) thickness view at 5x magnification…….48

33. SEM photos of the Mid-Plane Specimen: a) fracture surface; b) origin of delamination leading to fracture; c) 250x view of origin of fracture……..49

34. Additional SEM photos of the Mid-Plane Specimen: a) nickel nanostrands™ intact prior to failure; b) 500x view of origin of fracture……... 49

35. Fractured Interlaminar Specimen: a) width view; b) thickness view at 100x; c) thickness view at 5x magnification…….51

36. SEM photos of the Interlaminar Specimen: a) fracture surface; b) origin of delamination leading to fracture; c) 500x view of origin of fracture……..52

37. Additional SEM photos of the Interlaminar Specimen: a) 200x view of fracture surface; b) nickel nanostrands™ intact prior to failure…….52

Page

38. Fractured Exterior #1 Specimen: a) width view; b) thickness view at 100x; c) thickness view at 5x magnification…….53

39. Fractured Exterior #2 Specimen: a) width view; b) thickness view at 100x; c) thickness view at 5x magnification…….54

40. SEM Pictures of Fractured Exterior Specimens at 50x Magnification: a) exterior #1; b) exterior #2……... 55

41. SEM Pictures of Fractured Exterior Specimens at 200x Magnification: a) exterior #1; b) exterior #2……... 55

42. SEM photo of control specimen post irradiation…… 56

43. SEM photo of exterior specimen post irradiation……... 57

44. SEM photo of interlaminar specimen post irradiation…… 57

45. SEM photo of mid-plane specimen post irradiation……... 58

46. Failure Mechanism……..62

47. Stress-Strain Curves of 15.25 cm (6 in) Specimens at 159 MPa (23 ksi)……...63

48. Stress-Strain Curves of 15.25 cm (6 in) Specimens at 324 MPa (47 ksi)……...64

49. Stress-Strain Curves of 15.25 cm (6 in) Specimens at 386 MPa (56 ksi)……...65

50. Stress-Strain Curves of 15.25 cm (6 in) Specimens at 407 MPa (59 ksi)……...66

51. Stress-Strain Curves of 15.25 cm (6 in) Specimens at 427 MPa (62 ksi)……...67

52. Stress-Strain Curves of 15.25 cm (6 in) Specimens at 441 MPa (64 ksi)……...68

53. Stress-Strain Curves of 15.25 cm (6 in) Specimens to Failure (476 MPa (69 ksi) and 496 MPa (72 ksi)……68

54. Stress-Strain Curves of Control & Exterior 7.62 cm Specimens……69

55. Stress-Strain Curves of Interlaminar & Mid-Plane 7.62 cm Specimens…… 70

56. Fracture Surface of 15.25 cm Control Specimen, 50x……71

Page

57. Origin of Fracture Surface of 15.25 cm Control Specimen, 50X……... 71

58. Origin of Fracture Surface of 15.25 cm Control Specimen, 200X……. 72

59. Origin of Delamination Growth of 15.25 cm Exterior #1 Specimen, 200X…... 72

60. Origin of Delamination Growth of 15.25 cm Exterior #1 Specimen, 50X……. 73

61. Origin of Failure of 15.25 cm Exterior #1 Specimen, 400X…….. 73

62. Delamination of 15.25 cm Exterior #2 Specimen, 130X…… 74

63. Matrix Cracks & Delamination of 15.25 cm Exterior #2 Specimen, 200X…… 74

64. Origin of Failure of 15.25 cm Exterior #2 Specimen, 150X…….. 75

65. Fracture Surface of 15.25 cm Interlaminar Specimen, 50X……... 75

66. Fracture Surface of 15.25 cm Interlaminar Specimen, 200X……. 76

67. Matrix Cracking & Delamination of 15.25 cm Interlaminar Specimen, 400X.. 76

68. Matrix Cracking & Delamination of 15.25 cm Mid-Plane Specimen, 400X…. 77

69. Matrix Cracking & Delamination of 15.25 cm Mid-Plane Specimen, 200X…. 77

70. Matrix Cracking of 15.25 cm Mid-Plane Specimen, 400X…… 78

71. Fiber Failure of 15.25 cm Mid-Plane Specimen, 800X…….. 78

72. Fracture of 7.62 cm Irradiated Specimens…….. 79

List of Tables

Table Page

1. Calibration Procedure……... 27

2. Test Matrix……30

3. Specimen Configurations……..31

4. Summary of Tensile Test and Resistance Data…….34

5. Young's Modulus (E), UTS, and Strain Comparisons……. 43

List of Symbols and Acronyms

A	Area of Cross Section
E	Modulus of elasticity
L	Length of Electrode
R	Resistance
ρ	Resistivity
R_s	Sheet Resistance
ε	Strain
σ	Stress
T	Thickness of Specimen
EMI	Electromagnetic Interference
ESD	Electrostatic Discharge
NS	Nickel Nanostrands™
UTS	Ultimate Tensile Strength

EVALUATION OF NANOCOMPOSITES AS LIGHTWEIGHT ELECTRONIC ENCLOSURES FOR SATELLITES' APPLICATIONS

I. Introduction

Space offers a global prospective. The higher you are, the more of Earth's surface you can see. For thousands of years, kings and rulers took advantage of this fact by putting lookout posts atop the tallest mountains to survey more of their realm and warn of would-be attackers. Throughout history, many battles have been fought to "take the high ground." Space takes this quest for greater perspective to its ultimate end. From the vantage point of space, we can view large areas of Earth's surface. Orbiting spacecraft can thus serve as "eyes and ears in the sky" to provide the ultimate high ground [28]. The United States military's push for global reach and response requires that advanced systems be deployed in orbit around the world, taking advantage of this ultimate high ground, to aid in intelligence gathering, navigation, communications, control, remote sensing, and other military missions. These orbiting systems have to be lighter (to decrease launch costs), more reliable, less expensive, and operate at a higher total power than ever before. Additionally, they need to be survivable from electromagnetic phenomena resulting from the harsh space environment.

A spacecraft system's structure must be strong and stiff to provide integrity during launch as well as operations in space. Furthermore, the structure should be capable of removing heat from the high power components and satisfy crucial electromagnetic interference (EMI) requirements. Aluminum was the structural material

of choice up to the early 1990s because it is lightweight, cheap, strong, easy to machine, and available. The aluminum structure accounted for approximately 18% of the spacecraft's total dry weight. Lightweight composites such as graphite/epoxy and Kevlar/epoxy were introduced in the early 1990s to reduce the structural mass while increasing strength and stiffness. Since costs range from $2,000 to $10,000 per pound to launch an object into space, reducing the structural mass of the spacecraft can potentially save hundreds of thousands of dollars in launch costs [28]. Current high performance composite technology has reduced the structural weight to approximately 6 – 8% of the spacecraft's total dry weight [6]

Although these high performance structural components have dramatically reduced weight, unfortunately they are not capable of protecting critical spacecraft components from the harsh space environment on their own. The threats of spacecraft charging and uncontrolled electrostatic discharge, electromagnetic interference, and radiation from the sun can cause irreparable damages and are still critical concerns for these spacecraft composite structures [31]. To combat these threats, current composite spacecraft structures are electrically shielded by secondary materials such as foils, wires/straps, and conductive paint or tape coatings. While these secondary shielding materials are effective, they add additional manufacturing processes, are labor intensive, and increase structural weight, resulting in an increase in cost [4, 24-25]. In order to further reduce the spacecraft structural weight, while simultaneously eliminating the need for secondary shielding materials, new innovative materials are needed. Recent advances in nanocomposites offer the technology to meet this challenge.

Recently, the Materials and Manufacturing Directorate, Air Force Research Laboratory, WPAFB (AFRL/RX), working with Metal Matrix Composites of Heber, Utah have developed a new form of nano-structured nickel [1, 13]. This new material is called nickel nanostrands™, which are strands of 50 ~ 1000 nm diameter nickel particles linked in chains, microns to millimeters in length as shown in Figure 1. They are very similar to carbon nanofibers but provide the additional features of nickel, such as electromagnetic, chemical, catalytical and metallurgical properties. Nickel nanostrands™ provide a wide band of EMI shielding protection from the harsh space

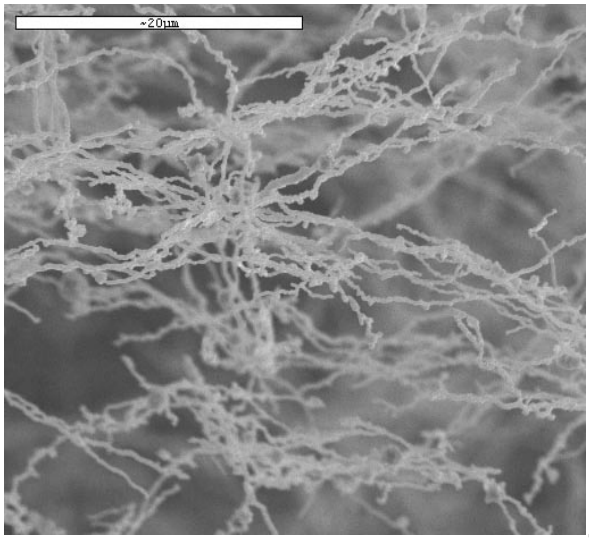

Figure 1. 200 nm Diameter Nickel Nanostrands™

environment due to their unique combination of electrical dc conductivity and ferromagnetism. Their complex nanostructured geometry provides for a high surface area and multiple angles of reflection and absorption. Preliminary tests conducted by AFRL/RX have shown that a thin film (0.1016 mm) containing 20% volume fraction of nickel nanostrands™ in polyimide is capable to shield about 80 decibels between the frequencies of 8 to 12 GHz with dc conductivity of 1,400 S/cm. Furthermore, this thin film has also survived a simulated space environment and was tested to shield 75 decibels

with a dc conductivity of 1,100 S/cm after this exposure [2]. However, many more studies are needed to fully understand the nanocomposites behavior for spacecraft applications because spacecraft deployed for military purposes must be engineered to survive the harshest space environments as orbit and apogee are dictated by operational requirements regardless of any temporal or geospatial radiation condition. This study is a step in this direction.

This thesis focuses on the synergism and interrelationship between the EMI shielding protection capability and mechanical properties before and after exposure to the space environment of nickel nanostrands™ when used in conjunction with M55J/RS-3 composite (i.e. graphite fiber in a toughened polycyanate resin matrix). Four different systems were tested for their ultimate tensile strength and EMI shielding protection properties before and after exposure to a representative five year space environment to determine their effectiveness in space operations. The four systems were additionally tested for their EMI shielding protection and resistive properties before, during and after monotonic tension tests of increasing loads up to fracture to determine what effect the tensile loading conditions have on EMI shielding protection and resistivity.

The systems include a baseline control panel of M55J/RS-3 and three systems with different layers of nickel nanostrands™ to determine which are superior for use in space. The four systems are shown in Figure 2. The baseline control specimen consists of a composite configuration of M55J/RS-3 in an 8-ply, quasi-isotropic, balanced symmetric lay-up of $[0/90/\pm45]_s$ with a corresponding fiber volume fraction, V_f, of 0.717. The three additional systems with nickel nanostrands™ (NS) include: mid-plane, exterior, and interlaminar. The mid-plane specimen has 200 grams per square meter

(GSM) of NS located at the mid-plane of the baseline. The exterior specimen has 100 GSM of NS each located at the top and bottom surfaces of the baseline. The interlaminar has four layers, each 50 GSM of NS, located between every second ply as Figure 2 indicates.

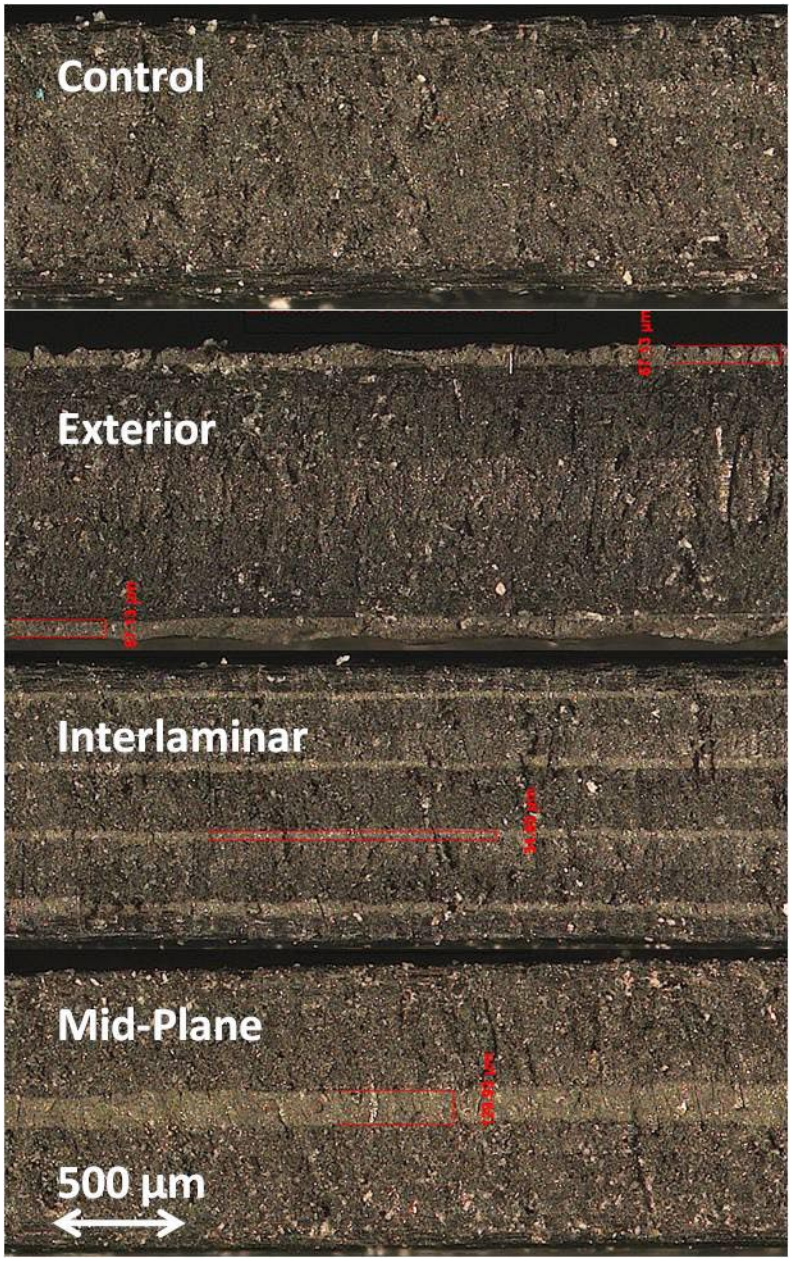

Figure 2. Cross-Sectional View of the Four Systems

A variety of research is being done into several areas of nanocomposites, but none that covers nickel nanostrands™ in conjunction with M55J/RS-3 composites and their potential ability to reduce spacecraft structural weight (i.e. launch costs) while simultaneously providing protection from the harmful space environment alone. The following chapters will provide background information on nanocomposites used in spacecraft structural applications and the harmful space environment, details of the methodology behind the specific tests conducted with this research, analysis and results of all tests, and will end with conclusions reached through the research in this thesis.

II. Background

2.1 Overview and Challenges of the Space Environment

The space environment presents one of the most, if not the most, challenging environments for materials design. To build spacecraft that will survive the harsh space environment, it is paramount to understand what hazards they will face. The Earth, Sun, and cosmos combine to provide unique challenges to spacecraft designers, as shown in Figure 3.

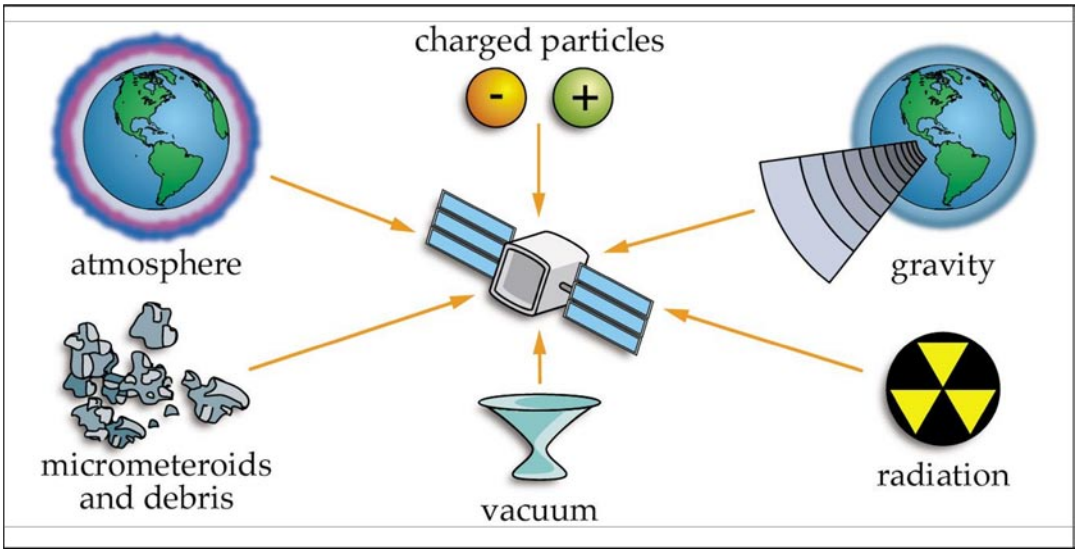

Figure 3. Factors Affecting Spacecraft in the Space Environment [28]

Earth exerts a gravitational pull which keeps spacecraft in orbit but presents fluid containment problems. The Earth's atmosphere can cause drag, which shortens orbit lifetimes, and is also full of atomic oxygen, which can damage exposed surfaces. In the vacuum of space, spacecraft can experience out-gassing, cold welding, and heat transfer problems. Out-gassing occurs when the atmospheric pressure drops to near zero, causing

a material to evaporate or sublimate. Cold welding is a condition that can cause metal parts to fuse together. Heat transfer problems may occur because the only way for a spacecraft to rid itself of heat is through radiation. Another danger to spacecraft is micrometeoroids and space junk that can collide at high speeds to damage the spacecraft. The final two dangers to spacecraft, that are most relevant to this study, are radiation and charged particles from the sun. Radiation can cause heating on exposed surfaces, damage to electronic components and disruption in communication, and solar pressure, which can change a spacecraft's orientation. Charged particles come from the solar wind and flares, galactic cosmic rays, and the Van Allen radiation belts. Spacecraft charging results when charges build up on different parts of the spacecraft as it moves through concentrated areas of charged particles. Once this charge builds up, discharge can occur with disastrous effects: damage to surface coatings, degrading of solar panels, loss of power, or switching off or permanently damaging electronics [28].

As previously mentioned, the high performance composites are now routinely used in nearly all spacecraft bus structures which had reduced the total structures' dry weight to approximately 6 ~ 8% to date. These lightweight composite structures carry all inertial loads and provide stiffness and dimensional stability better than their aluminum predecessors. Additionally, they are selected for their ability to transfer or manage waste heat produced from the high power components of the spacecraft. Unfortunately, these composite materials pale in comparison to aluminum when it comes to protection from the harsh space environment. They require additional steps to electrically shield and prevent charging and consequential discharging damage to the payload electronic components. These additional steps add undesirable weight that drives manufacturing,

and most importantly, launch costs upward. To reduce the structures' weight further from the present levels of 6 ~ 8% of the total weight, new innovative materials are needed. Recent advances in nanocomposites offer an opportunity to meet this challenge.

2.2 Nanocomposites

Since the advent of single-wall carbon nanotubes (SWNTs) more than a decade ago [16], there has been significant interest in the scientific and engineering communities to utilize the extraordinary physical and mechanical properties of numerous nano or sub-micron size structural materials. Carbon nanotubes and nanofibers have received an incredible amount of attention over the past five years as they are candidates for use in several applications. They also provide tremendous opportunities in the design of multifunctional materials systems. Particularly, they promise to provide solutions to many vexing problems encountered during the application of traditional composite materials. They are electrically conductive and therefore are suitable for applications that require the capability to discharge electrostatic potentials. They provide sufficient conductivity for electrostatic painting. Further, they shield from the radio frequency interference (RFI) or lightening strikes while keeping or enhancing the inherent high strength/modulus to weight ratio [27, 30]. Therefore, when combined with traditional graphite composite materials, these nanocomposites can accomplish what traditional aluminum did in spacecraft structures but at a much lower mass: provide mechanical support, remove excess heat, and protect from EMI. Furthermore, the lower mass equates to a much lower launch cost. However, there have been a very limited number of studies which have shown that SWNTs are radiation tolerant under high energy neutrons

(upper atmosphere), medium energy protons (LEO), and high energy protons and iron ions (interplanetary space) [6].

One of the major roles of carbon nanotubes and nanofibers is to make nanocomposites a more electrically conductive material. Unfortunately, these new materials, carbon nanofibers in particular, are sometimes limited by the intrinsic properties of carbon and its molecular orientation in the nanostructure. Alternatively, the highly conductive carbon nanotubes are extremely expensive to manufacture. In order to utilize the conductive capabilities of nanotubes, the creation of a highly nanostructured high aspect ratio filamentary pure metal is a candidate to extend the art of rendering normally dielectric materials as conductive, especially if the nanostructure could be made in a fully interconnected three dimensional nano-lattice. Incidentally, this lattice is exactly what nanostrands are when they are created. As previously mentioned, the Materials and Manufacturing Directorate, Air Force Research Laboratory, WPAFB (AFRL/RX), working with Metal Matrix Composites of Heber, Utah as developed a new form of nano-structured nickel. This new material, called nickel nanostrands^{TM}, is made up of strands of 50 ~ 1000 nanometer diameter nickel particles linked in chains, microns to millimeters in length. They are very similar to carbon nanofibers but provide the additional features of nickel, such as electromagnetic, chemical, catalytical, and metallurgical properties at less cost than SWNTs [1, 13].

When the nanostrand veil or cake is pressed by hand, it can be pressed in a controlled fashion up to about 20% as shown in Figure 4. At this level, the conductivity is truly extraordinary, i.e. 5000 Siemens/cm, which equates to a resistivity of 0.0002 ohm-cm. Additionally, this fine structure allows for the easy capillary infiltration into a

wide variety of polymers, including thermosets such as epoxy and polyimide, thermoplastics such as polyethylene, elastomers such as silicone, thermoplastic polyurethane, and paints such as acrylic, epoxy and urethane [13]. All of these media have been rendered conductive. Figure 5 shows an example when nickel nanostrands™ are added to epoxy. The upper line in this figure is for nanostrands when mixed in a typical way in epoxy adhesive. This exhibits volume resistivity that is similar to or better than that of competing technologies. The lower line in this figure is typical of the volume resistivity of the continuous nanostrand lattice that has been pressed to a

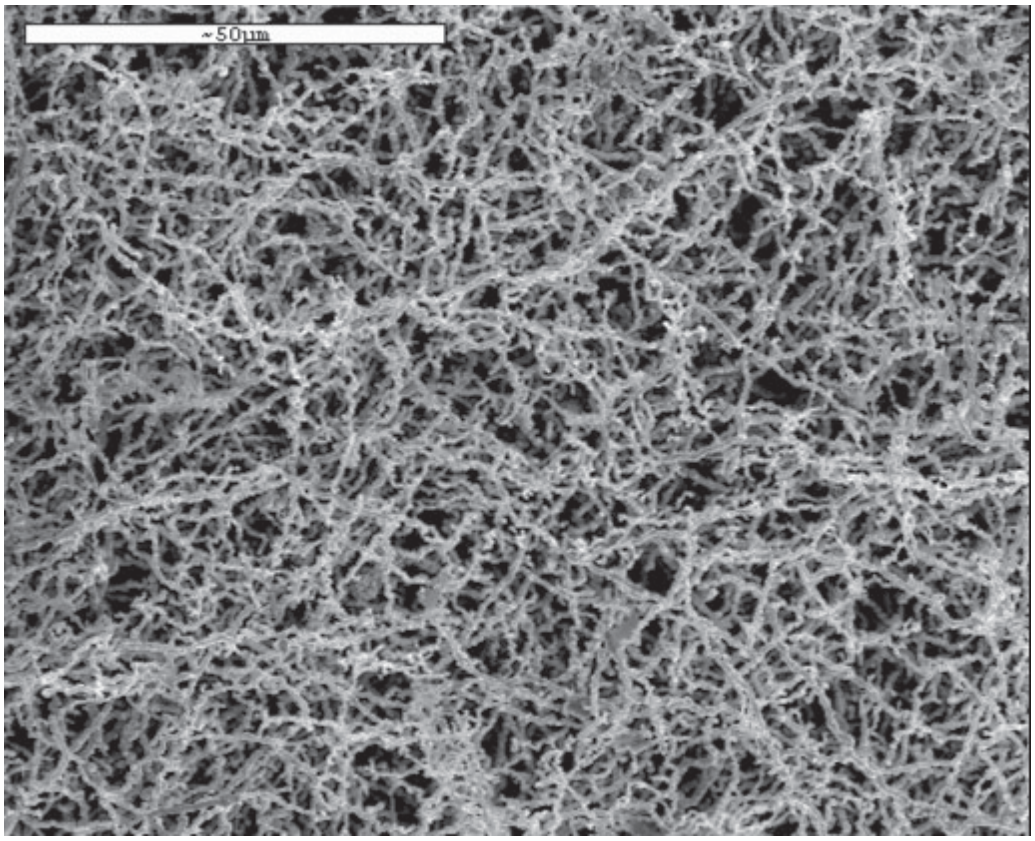

Figure 4. Nanostrand lattice that has been compressed to about 20% volume solid [13]

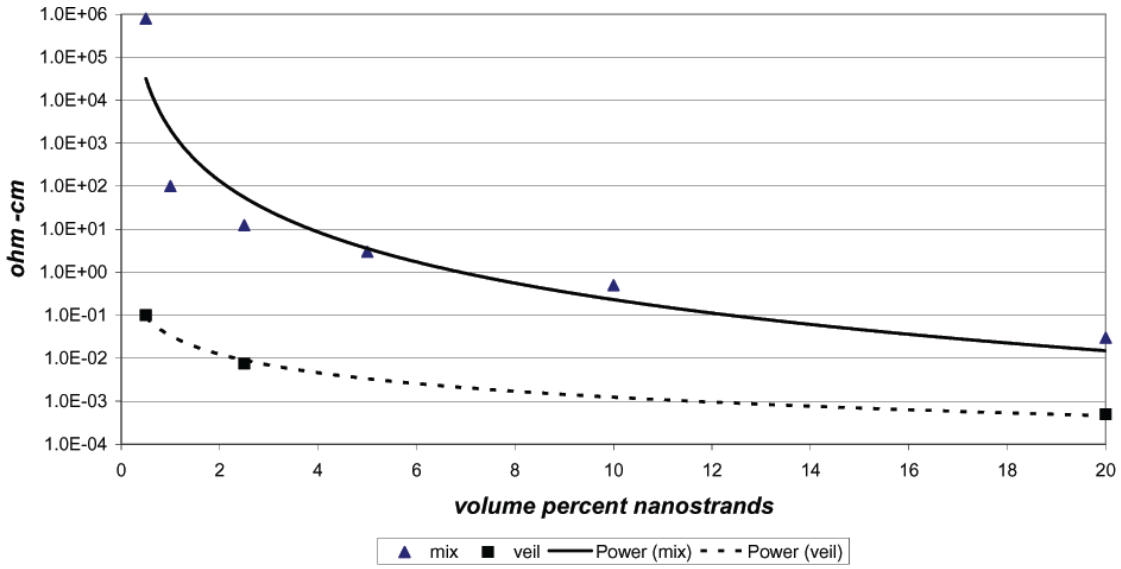

Figure 5. Volume resistivity of nanostrands in polymers veil vs. mix [13]

desired volume fraction and then infiltrated with resin, referred as a veil. The veil exhibits volume resistivities on the order of 10^{-2} at very low volume fractions, and approaches 10^{-4} at higher fractions. These are excellent levels of conductivity for a composite. [13]

The advantage of adding nanostrands to a conductive fiber composite system is that it only requires a small amount of nanostrands to create increasingly conductive paths from fiber to fiber and throughout the resin. In addition, the nanostrands tend to fill in a previously resin rich area of the polymer, so that even these regions are conductive. Thus, not only can a fully conductive composite be created, the specific conductivity of the composite can be engineered to any desired level and orientation. The dramatic increases in composite conductivity as a function of adding nickel coated fibers or nickel nanostrands™, or both, are shown in Figure 6 [13].

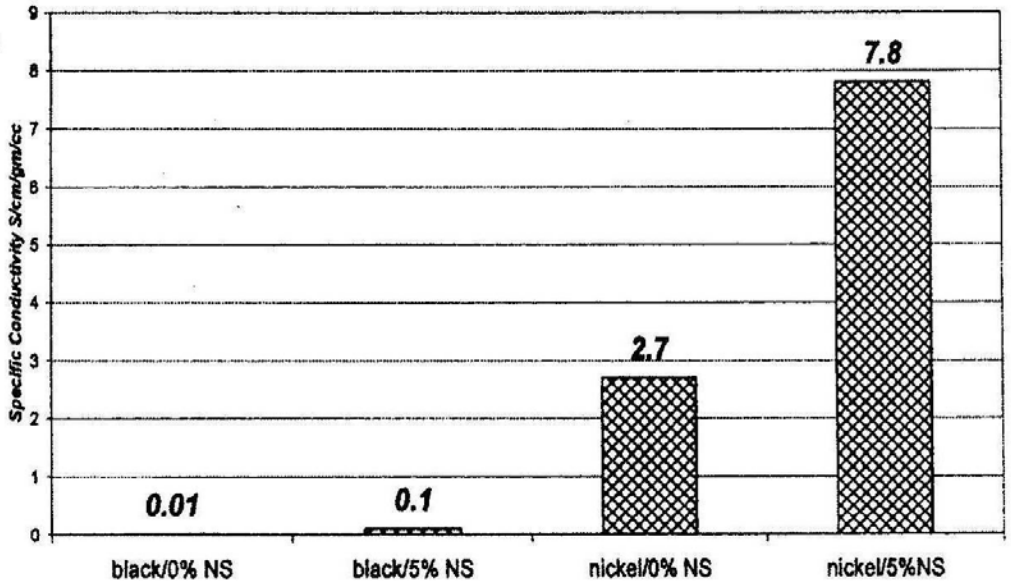

Figure 6. Specific conductivity (S/cm/gm/cc) of composites with black cloth or nickel coated cloth and neat resin or 5% nickel nanostrand resin [13]

Nickel nanostrands™ also show promising capabilities of electrostatic dissipation (ESD) and electromagnetic interference (EMI) shielding protection which is crucial in the space environment. With respect to ESD, the nanostrands provide sufficient conductivity, even in low concentrations, to stop a hefty discharge. As shown in Figure 7, a small concentration of nanostrands in an otherwise non-conductive system (silicon rubber on a polyester cloth), provided conductive protection against a 625,000 volt discharge [13]. Nickel nanostrands™ are also effective in shielding electromagnetic radiation. Preliminary studies have also shown that they provide a wide band of EMI shielding protection. In Figure 8, only a few mils of a nanostrand composite film are found to create a highly effective EMI shield across a wide band-width. While 60 dB is a respectable shielding level, it is anticipated that thicker or more concentrated nanostrands, particularly in concert with conductive fibers may provide for excellent

broadband shielding. The unique attribute of nanostrands appears to be their increasing effectiveness at decreasing frequencies; a phenomenon which is opposite to most other shielding materials [13].

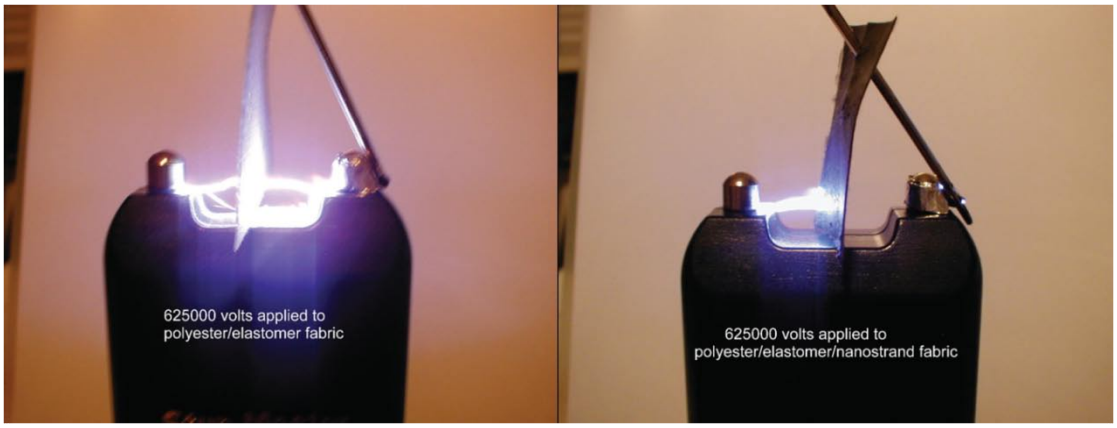

Figure 7. A 625,000 volt discharge readily passes through a non-conductive composite at the left. But with the addition of 5% volume nanostrands to the resin, the same discharge is effectively controlled [13]

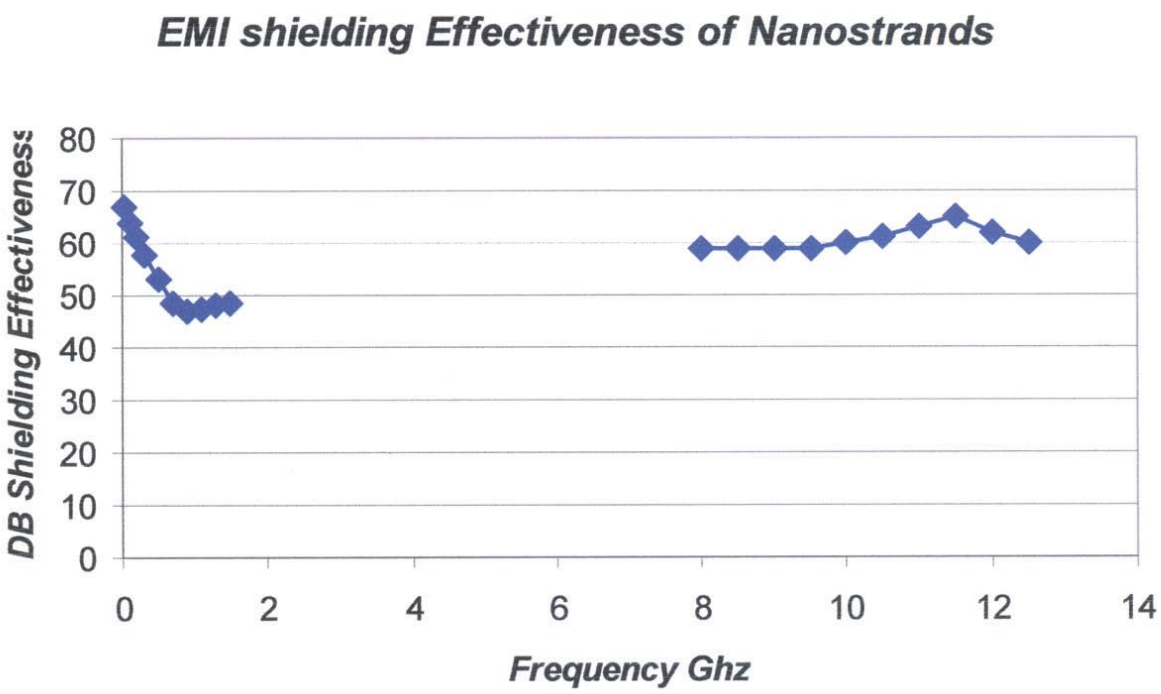

Figure 8. Electromagnetic shielding properties of nanostrands [13]

2.3 Radiation Environments and their Damage to Materials

The space environment presents a hazardous radiation situation which can have serious effects on spacecraft electronics as well as spacecraft structures. There are three major sources of radiation: long term exposure within the Van Allen radiation belts, galactic cosmic rays (GCR), and solar proton events (SPE). Exposure to any of these types of radiation can drastically degrade the mechanical and electrical properties of materials. Specifically, materials can fail and/or electronic systems can become completely disabled due to spacecraft charging, deep dielectric charging, single event upsets (SEUs), and high energy solar radiation particles. This is most important because the nanocomposites studied in this thesis will be the first line of defense for the spacecraft structure in the harsh space environment.

Technically, spacecraft charging is a variation in the electrostatic potential of a spacecraft surface with respect to the surrounding plasma caused by photoemission and plasma bombardment. Although the buildup of large static charges may confuse or blind certain sensors, the real danger lies in the resulting discharge because structural damage is a real possibility. Even weak discharges have been related to a variety of problems which include: spurious electronic switching activity (such as turning off a recorder or activating a radio), breakdown of vehicle thermal coatings, amplifier and solar cell degradation, and degradation of optical sensors [31].

Deep dielectric charging occurs when electrons with energies between 2 and 10 MeV have enough energy to burrow deep into satellite surfaces. This excess charge spreads out evenly on conducting surfaces, but the charge accumulates on dielectric surfaces resulting in uneven electric potential between different portions of the satellite.

Eventually, potential differences can reach the breakdown threshold and a static discharge will then occur. Unlike surface charging, deep dielectric charging can form strong potential differences on the inside surfaces of satellites, and thus the resulting discharges can arc directly into the satellite's internal electrical circuitry [31].

Single event upsets (SEUs) are bit flips in digital microelectronic circuits. SEUs can cause: damage to stored data, damage to software, the central processing unit (CPU) to halt, the CPU to write over critical data tables, and various unplanned events due to faulty commands. SEUs in spaceborne electronics are caused by the direct ionization of silicon material by a high energy ion passing through it. The near Earth particle environment includes GCR, energetic particles from the Sun, and trapped protons. The normal factor in SEU production is the heavy ion cosmic ray, although large solar flares can produce a substantial increase in SEUs. Fortunately, such large flares occur only once every few years [31].

At high altitudes (geostationary orbit, GEO), solar radiation accounts for the majority of radiation exposure. The two primary phenomena that present the solar radiation environment are solar flare events (SFEs) and corona mass ejections (CMEs). These events are highly unpredictable but activity commonly comes and goes based on the 22 year solar cycle. What is predictable from two events is the type of radiation they present to spacecraft. Generally, SFEs and CMEs exhibit a large flux of high-energy solar protons, electrons, and alpha particles enhancing an already steady flow from typical solar activity. These particles are the primary source of damage in the natural space environment [31].

2.4 Summary

The natural space environment poses many threats to spacecraft structures as well as electronics. The most dangerous threats are radiation and spacecraft charging which can lead to catastrophic failure of spacecraft structure and/or electronics. It is paramount that any improvements made in spacecraft structures provide EMI shielding protection and be highly conductive to avoid ESD. Nickel nanostrands™ coupled with a M55J/RS-3 composite have the potential to eliminate these risks.

III. Method of Experimentation

3.1 Introduction

The purpose of this chapter is to explain precisely how the tests were run so they may be easily repeated in future research efforts. Topics covered in this chapter include: cutting and preparing the specimens, tensile test and resistance measurement equipment and procedures, electromagnetic interference (EMI) test equipment and procedures, simulated space environment test equipment and procedures, and the test plan for this study.

3.2 Specimen Preparation

The M55J/RS-3 nickel nanostrand^{TM} specimens used for this research effort were cut from a 15.25 x 15.25 cm (6 x 6 in) panel by the AFIT machine shop using a high pressure waterjet cutter. To prevent edge delamination, the panel was sandwiched between two thin plastic sheets with double sided adhesive tape. Average thickness of the panel was 1.016 mm (0.04 in). Rectangular shaped specimens of constant rectangular cross-section were used in all tests. The nominal size of specimens was 15.25 x 2.7 x 0.1016 cm. Monotonic tensile and EMI tests were conducted with 15.25 cm coupons with copper tape laminated at both ends of the composite in order to measure the resistance across samples. However, space environment tests utilized 7.62 cm (3 in) coupons cut out of a 15.25 cm coupon with the copper tape removed in order to fit into the test apparatus and to maximize the number of samples. These specimen geometries are shown in Figure 9.

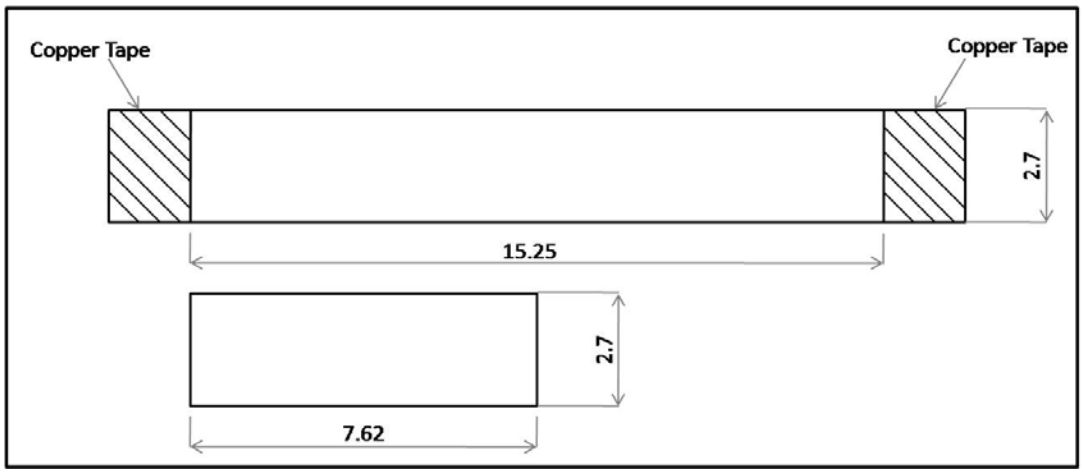

Figure 9. Test Specimens, dimensions in cm.

After machining, the specimens were cleaned to remove any debris created during the cutting process, ensuring a good clean bond between the glass/epoxy tabs and the specimens at the gripping sections. These glass/epoxy tabs are necessary to protect the specimen against possible surface cracks caused by the grips of the tensile testing machine that could lead to premature failure. The 2.54 x 2.7 cm (1 x 1.0625 in) tabs were attached to the specimens using M-Bond 200 adhesive.

The last step in preparing the specimens for testing was to solder solid core copper wire to the copper tabs in order to be able to measure the resistance before, during, and after each monotonic tension test. The soldering technique is shown in Figure 10. Once soldering was complete, electrical tape was wrapped around the soldered area numerous times to provide protection and stability. A final soldered and tabbed specimen can be seen in Figure 11.

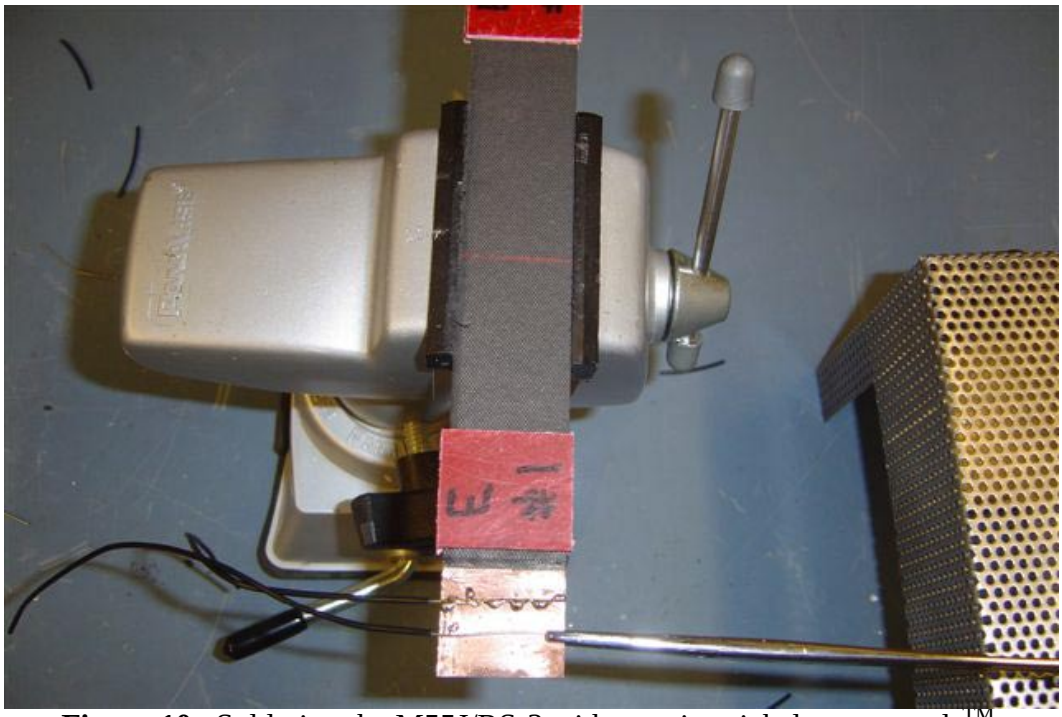

Figure 10. Soldering the M55J/RS-3 with exterior nickel nanostrands™

Figure 11. M55J/RS-3 with exterior nickel nanostrands™ tensile specimen.

3.3 Monotonic Tension and Resistance Test Equipment and Procedures

Ultimate tensile strength (UTS) tests were conducted with an MTS 810 servo-hydraulic testing machine with a maximum load capacity of 22 kips (98 kN) as shown in Figure 12. The machine was equipped with MTS 647 hydraulic wedge grips that applied a grip pressure of 8.2 MPa (1.2 ksi) in all tests. Top and bottom grips were spaced so they gripped the same amount of the specimen. When inserting the specimen into the grips it is crucial to ensure complete vertical alignment so as to avoid premature failure and/or inaccurate elastic data.

Resistance measurement was conducted simultaneously with UTS tests in order to determine how resistance changes under given loading conditions. Resistance measurement was performed with two Keithly 2400 source measure units (SMUs) as shown in Figure 13. One SMU sourced in the current and the other SMU sensed the voltage output. The sourced current was fixed at 1 mA and the sensed voltage was on the order of mV. Gator clips were connected to the soldered wires on the specimen and the tests were run. As current and voltage are known values, the resistance can be calculated from Ohm's law:

$$V = IR \tag{1}$$

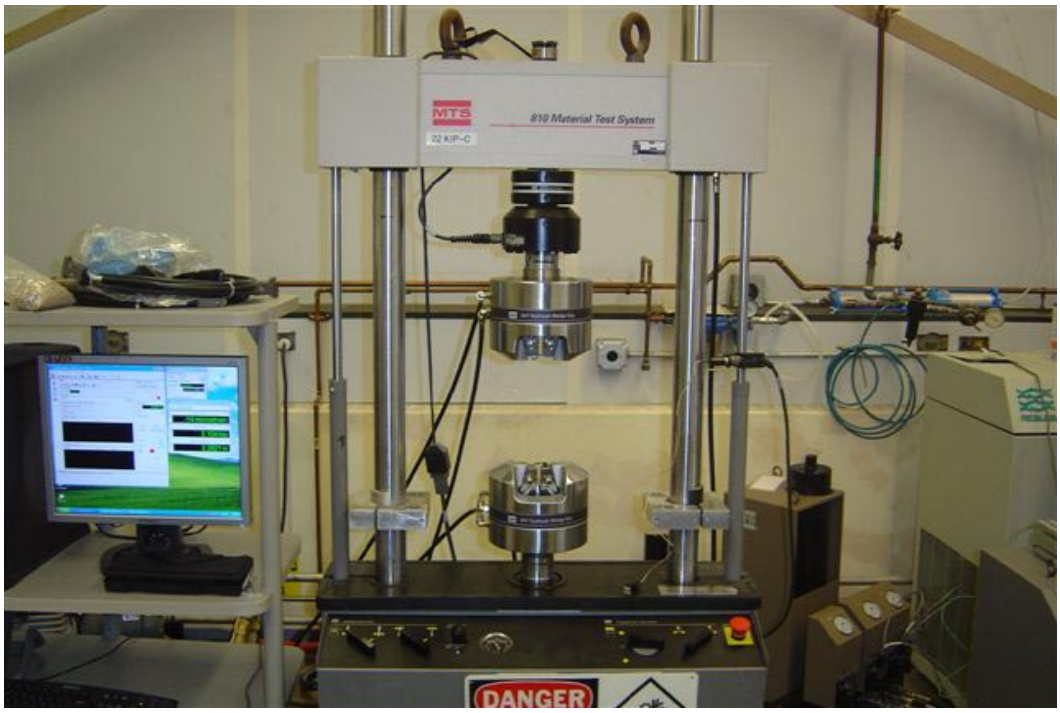

Figure 12. MTS Machine.

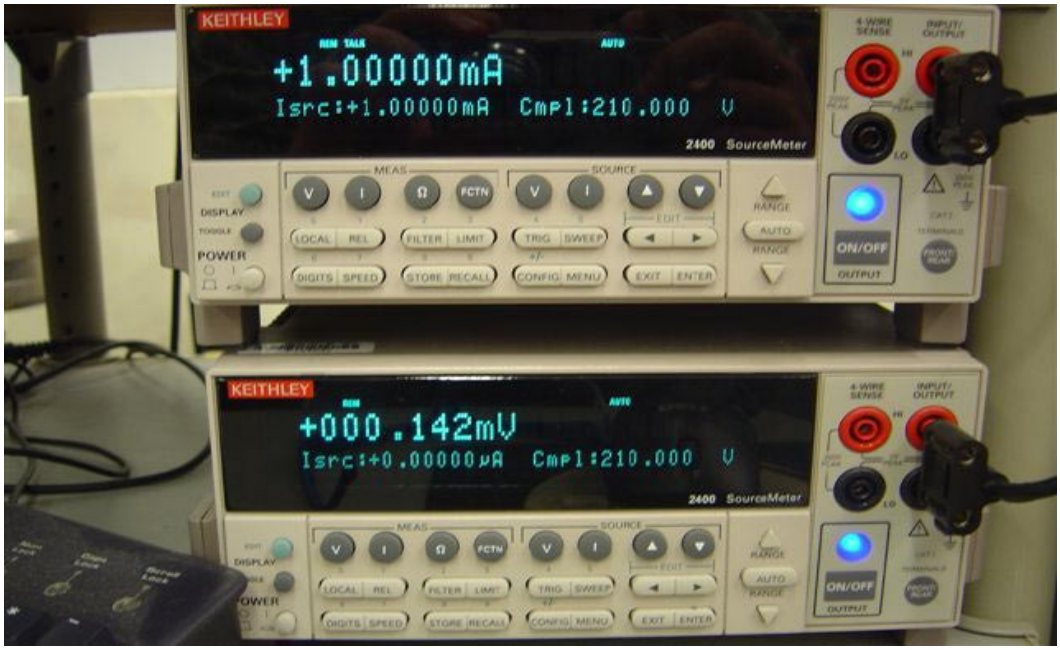

Figure 13. Keithly 2400 Source Measure Units.

Tensile tests for this study were run in a laboratory at room temperature. Prior to mechanical testing, the MTS 810 machine was warmed up by cycling the actuator in the displacement control mode for 20-30 minutes to ensure the hydraulic fluid was at operating temperature. Per the manufacturer's recommendation, the function generator was programmed to deliver a cyclic command in displacement control using a square wave at a frequency of 3 Hz and amplitude of 0.0762 mm (0.003 in). Once the MTS 810 machine was warmed up, the grips were brought to the appropriate testing height, and the specimen was mounted and checked for proper positioning and alignment. Once both top and bottom grips were closed the force was zeroed using the force control mode and the MTS clip-on strain gage was mounted to the specimen and strain was also zeroed before running the test.

Before beginning the tension test, the Keithly 2400 SMUs were connected to the four soldered wires on the specimen with gator clips in order to source the 1 mA current and sense the mV voltage. The SMUs were connected to a separate laptop computer, courtesy of the Materials and Manufacturing Directorate of the Air Force Research Laboratory (AFRL/RX), which had a program set to record the voltage, current, and resistance data once every half second in mV, mA, and mΩ respectively during the tension test. The MTS Multipurpose Testware (MPT) software allowed for the programming of automated test procedures and facilitated real time data collection. Procedures were written in a manner so that after the specimen was in place, the test ran autonomously to the end of the procedure or until specimen failure. An example of a typical tension test procedure is shown in Figure 14.

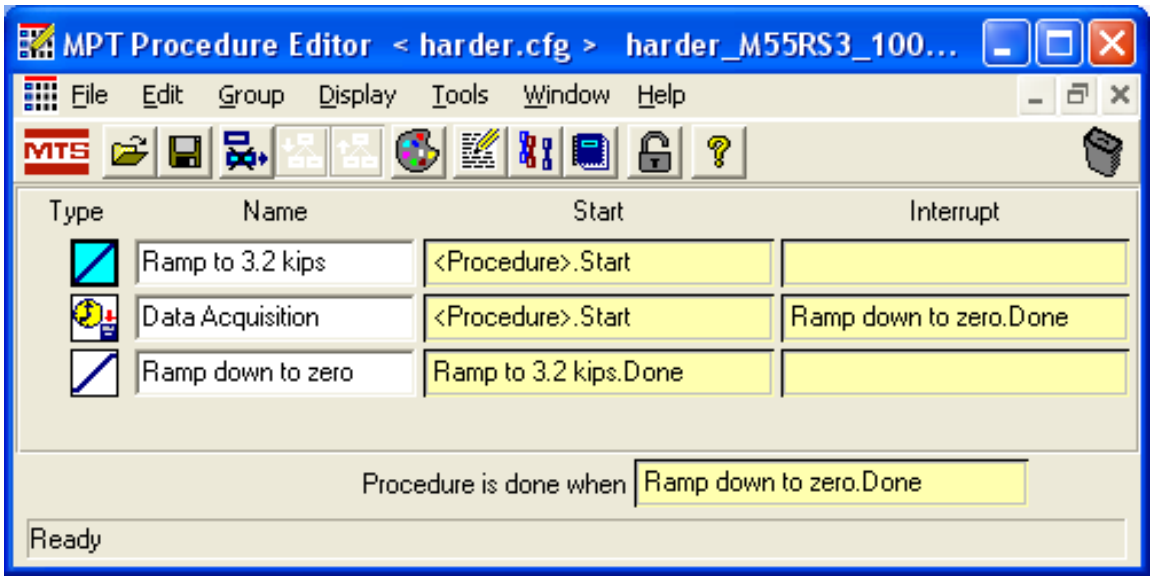

Figure 14. Typical Tension Test Procedure

Testing began once the specimen was properly mounted in the MTS 810 and connected to the Keithly 2400 SMUs. Start buttons were pushed simultaneously on the MTS 810 and laptop computers and the data collection process began. All specimens were loaded at a speed of 22.25 newtons/sec (0.005 kips/sec). The MTS 810 computer collected data on applied force (kips), strain (in/in), displacement (in), and time (sec) whereas the laptop computer recorded data on sourced current (mA), sensed voltage (mV), resistance (mΩ), and time (sec). Once the test was complete, the specimen was removed from the fixture and data analysis began. A complete test set-up is shown in Figure 15.

Figure 15. Mechanical Testing Station

3.4 EMI Test Equipment and Procedures

All EMI tests were conducted at the Materials and Manufacturing Directorate of the Air Force Research Laboratory (AFRL/RX). EMI tests were performed before and after each tension test by the Agilent Technologies E8362B PNA Series Network Analyzer as shown in Figure 16. This was done in order to determine how tensile loading affects the shielding capabilities of the composite. Additional resistance tests were performed before and after each tension test by the EXTEC 380560 ohm-meter located in the same AFRL facility as the Network Analyzer as shown in Figure 17. The additional resistance test was a quick and easy way to verify any resistance changes due to the prescribed tensile load.

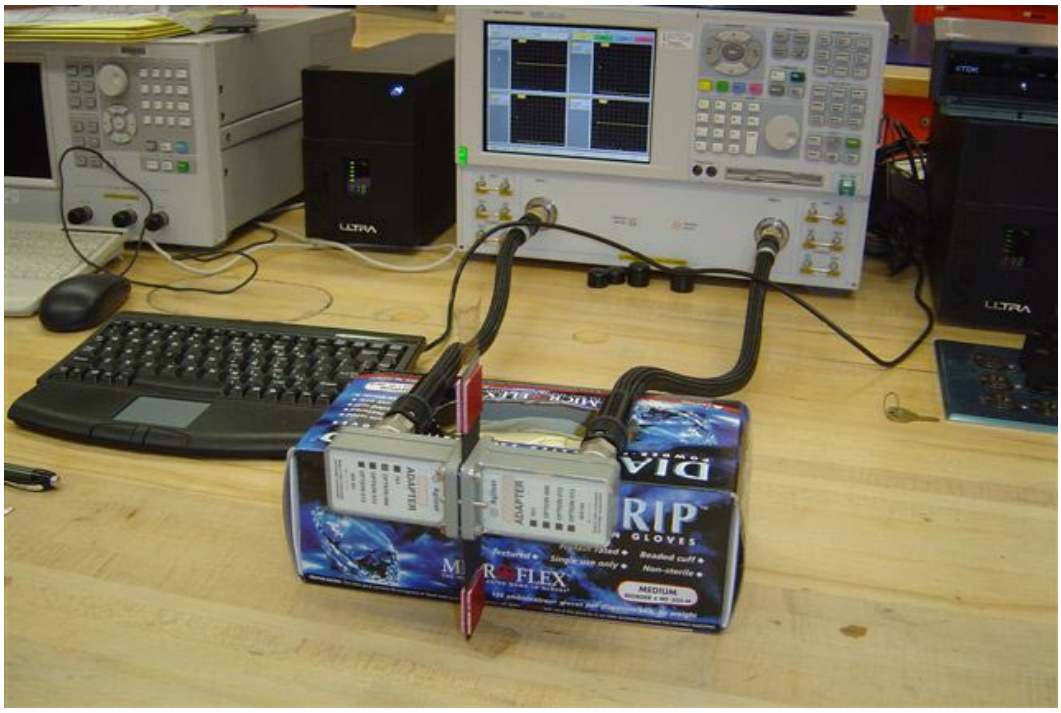

Figure 16. EMI Testing Equipment

Figure 17. Secondary Resistance Testing Equipment

The Network Analyzer for EMI measurement must be properly calibrated before each set of testing. The purpose of the calibration is to determine several undesired parameters that may be removed or suppressed from the test sample data by subsequent mathematical operations. When properly calibrated (measured) for each frequency in the data set, these undesired parameters include the effects of the directivity of and reflection from the couplers, reflections due to mismatches in the input and output test lines, and direct coupling of signals between the input and output ports of the device along external bypass routes [17]. A complete step-by-step calibration procedure is presented in Table 1.

Table 1. Calibration Procedure

1	Open Network Analyzer software
2	File, recall previous test
3	Set frequency range to: yellow = 8.2 GHz; green = 12.4 GHz
4	Select Calibration Wizzard
5	Click the boxes for: unguided, TRL, 1-2 ports, and cal kit #28
6	Click Next, Through Standard, & Line Standard
7	Clamp the SHORT piece into the sample holder (piece without middle holes)
8	Click both SHORT buttons
9	Remove SHORT piece
10	Clamp LINE piece into the sample holder (thickest piece with middle holes)
11	Click LINE button; select X-Band 1/4 wavelength line; select Next
12	Remove LINE piece
13	Clamp the ends of the sample holder together with nothing in between
14	Click THRU
15	Click Next
16	Click Finish

After calibration was complete EMI testing began. It was critical to measure the EMI attenuation in exactly the same spot on the sample test after test in order for the data to be accurate. Therefore a red wax marker was used to draw a line on each specimen, that when inserted in the sample holder, accurately lined up with the top. This ensured

repeated testing was performed on the same area of the specimen. After the specimen was clamped to the sample holder and properly aligned with the red line, each of the four windows on the computer screen was right-clicked and auto-scale was selected. This provided the EMI attenuation data measurement in decibels (dB) where the larger the number the better. The EMI measurements were not absolute values but were recorded after each successive tension test as deltas or changes. This was due to the scattering on the macroscopic carbon fibers. If testing a slightly different spot on the specimen the standing wave would be scattered differently because the fibers act like diffraction gratings.

3.5 Simulated Space Environment Test Equipment and Procedures

Simulated space environment testing was conducted at Wright State University (WSU) with a High Voltage Engineering, Europa, Electron Van de Graaf Accelerator, model number SN-A94 as shown in Figure 18. All irradiations were performed by the WSU operating staff. The 7.62 cm (3 in) specimens were mounted onto a conductive copper sample station at the end of the electron beam using a silicon paste as shown in Figure 19. The mount was affixed to the beam tube and the chamber was evacuated to 10^{-7} Torre for 24 hours. The specimen was irradiated with 1.2 MeV electrons which were scanned across the surface utilizing a steering magnet in a 3.175 cm (1.25 in) diameter spot across the midsection of the specimen. The total electron fluence was 10^{14} electrons/cm^2. Specimens were irradiated for approximately five minutes which produced a simulated five year exposure to the space environment. After this exposure to the electrons, the specimens were tested for EMI shielding properties as well as ultimate

tensile strength to determine what affects, if any, the space environment had on these material properties.

Figure 18. Space Environment Test Equipment

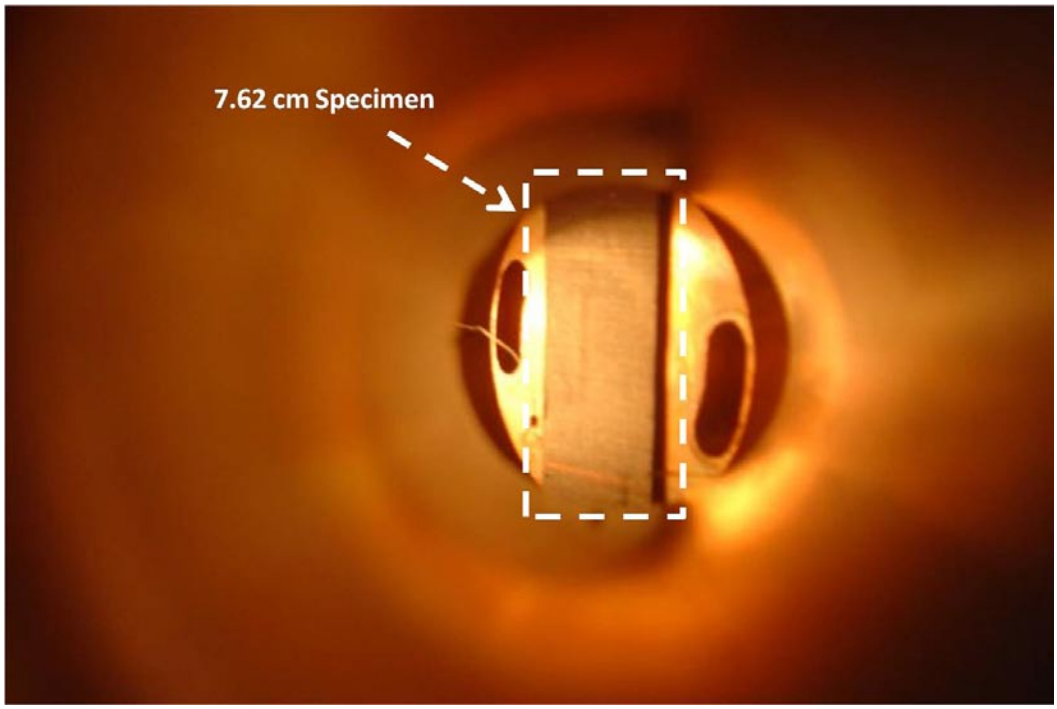

Figure 19. Mounted Specimen in Beam Tube

3.6 Test Plan

In order to compare and contrast the four different systems which were described in Chapter I, they were each tested in four different environments: monotonic tension,

resistance measurements, EMI shielding protection, and the simulated space environment. Monotonic tension tests were performed on each of the four different specimens at the following intermittent tensile loading conditions up to final fracture: 159 (23), 324 (47), 386 (56), 407 (59), 427 (62), 441 (64), and 483 (70) MPa (ksi). This equates to approximately 33, 66, 80, 86, 90, 93, and 100% of the ultimate tensile strength (UTS), respectively. Resistance measurements were conducted simultaneously to determine how the increasing tensile loading conditions affected resistance in each of the four types of specimens during the monotonic tension tests. EMI shielding tests were conducted on each of the four different specimens before and after each monotonic tension test in order to determine how the increase in the intermittent tensile loading conditions up to the UTS affected their EMI shielding properties. Finally, simulated space environment tests were run on each of the four types of specimens to understand what effects, if any, the harmful space environment has on the EMI shielding and mechanical properties. The test matrix is shown in Table 2.

Table 2. Test Matrix

Testing Method:	# of 15.25 cm Specimens	# of 7.62 cm Specimens
Monotonic Tension	1C*, 1E*, 1I*, 1M*	1C, 1E, 1I, 1M
EMI Attenuation	1C, 1E, 1I, 1M**	1C, 1E, 1I, 1M
Resistance Measurement	1C, 1E, 1I, 1M**	N/A
Space Environment***	N/A	1C, 1E, 1I, 1M

* C = control; E = exterior; I = interlaminar; M = mid-plane

** One specimen of each lay-up used in all tests with 15.25 cm specimens for a total of 4 specimens

*** Two 7.62 cm specimens of each lay-up were used in space environment tests: one each for monotonic tension and EMI and one each for scanning electron microscope analysis

IV. Analysis and Results

4.1 Introduction

This chapter reports the experimental results obtained during the course of this research. In order to compare and contrast the four different systems, they were each tested in four different environments: monotonic tension, resistance measurements, EMI shielding protection, and the simulated space environment. Every specimen had a baseline composite configuration of M55J/RS-3 with a 8-ply, quasi-isotropic, balanced symmetric lay-up of $[0/90/\pm45]_s$ and a corresponding fiber volume fraction, V_f, of 0.717. Three additional systems having nickel nanostrands™ (NS) layers were also tested which had these layers at: mid-plane, exterior, and distributed evenly at four interlaminar levels. The last one will be referred to as interlaminar for the sake of brevity. The mid-plane specimen had 200 grams per square meter (GSM) of NS located at the mid-plane of the baseline. The exterior specimen had 100 GSM of NS each located at the top and bottom surfaces of the baseline. The interlaminar specimen had four layers, each 50 GSM of NS, located between every second ply as shown in Table 3 and Figure 20. Each NS lay-up had 200 GSM NS total and the lay-ups are shown in Table 3 from one surface (ply) to the other one.

Table 3. Specimen Configurations

Panel Type	Composite Configurations													
Control		0		90	45		-45		-45		45	90		0	
Exterior	(100 GSM NS)	0		90	45		-45		-45		45	90		0	(100 GSM NS)
Mid-Plane		0		90	45		-45	(200 GSM NS)	-45		45	90		0	
Interlaminar		0	(50 GSM NS)	90	45	(50 GSM NS)	-45		-45	(50 GSM NS)	45	90	(50 GSM NS)	0	

Each tension specimen was tested for EMI shielding and resistance measurements before monotonic tension testing began in order to establish the baseline values. This

enabled comparisons to be made between each of the four specimens as to how their EMI shielding and resistance properties would change after each load increase all the way to fracture. However, each space environment specimen was only tested for EMI shielding measurements before irradiation as the copper tape had to be removed in order to fit on the testing fixture. This enabled comparisons to be made between each of the four specimens as to how their EMI shielding and tensile properties changed after exposure to the simulated space environment.

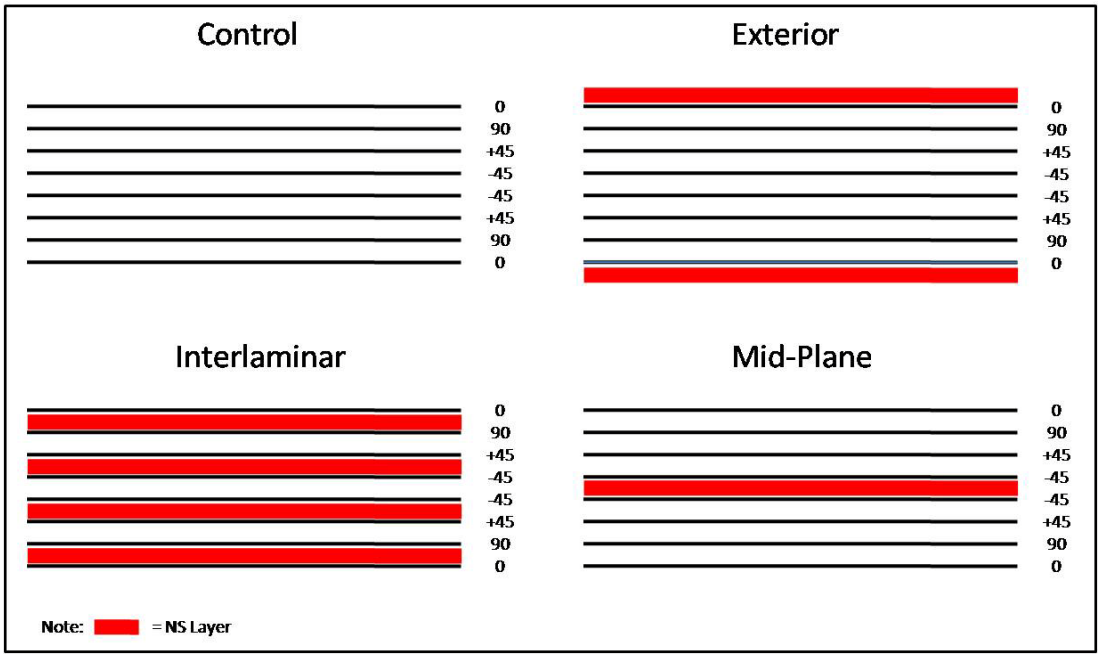

Figure 20. M55J/RS-3 Composite Configurations

4.2 Monotonic Tension and Resistance

Monotonic tension tests were run on each of the four different 15.25 cm specimens at the following intermittent loading conditions up to fracture: 159 (23), 324 (47), 386 (56), 407 (59), 427 (62), 441 (64), and 483 (70) MPa (ksi). This equates to approximately 33, 66, 80, 86, 90, 93, and 100% of the ultimate tensile strength (UTS),

respectively. Resistance tests were conducted simultaneously to determine how the tensile loading conditions affected resistance in each of the four types of specimens during the monotonic tension tests. Note that there are two exterior samples due to the fact that exterior #1 was accidentally tested to failure on the third tension test stage. However, the properties of both exterior samples mirror each other which show that there was minimal scatter between replicate tests. The control specimen fractured on the fourth loading cycle at a stress level of 407 MPa (59 ksi). The interlaminar specimen fractured on the fifth loading cycle at a stress level of 414 MPa (60 ksi). The exterior #2 and mid-plane specimens fractured on the seventh loading cycle at a stress level of 476 and 496 MPa (69 and 72 ksi), respectively. Stress-strain curves for all 15.25 cm specimens and loading levels are shown in Appendix A.

The resistance values utilized in this thesis were measured from the EXTEC 380560 ohm-meter. Resistance values were measured before and after each tension test. During the monotonic tension tests, the maximum and minimum values of resistances were within ± 0.015 ohms from the average values and were on the average only 0.007 ohms away from the mean. This means that resistance does not fluctuate a large amount throughout monotonic tensile loading conditions since resistance values fluctuate at only ± 6% of the mean values. Thus resistance did not fluctuate considerably throughout the tension tests. Table 4 summarizes these testing results. Although the unit of sheet impedance is ohms, measured results are typically labeled *ohms per square* to emphasize that a thin sheet, not a lumped element, was measured [17]. Therefore, resistance values recorded in ohms were converted to sheet resistance values in ohms per square, utilizing the following two equations for resistivity (ρ) and sheet resistance (R_s):

$$\rho = \frac{RA}{L} \tag{2}$$

where R = resistance; A = cross sectional area; L = electrode length, and

$$R_s = \frac{\rho}{T} \tag{3}$$

where T = specimen thickness.

Table 4. Summary of Tensile Test and Resistance Data

Step	Specimen	Stress MPa (ksi)	Strain (mm/mm)	E GPa (MSI)	Average In-Test Resistance (Ω)	Pre- and Post-Test Resistance (Ω)	Restivity (Ω-cm)	Sheet Resistance (Ω/square)
I	Control	0	0	0	0	0.144	0.0042	0.0410
	Exterior #1	0	0	0	0	0.150	0.0042	0.0393
	Exterior #2	0	0	0	0	0.145	0.0041	0.0392
	Interlaminar	0	0	0	0	0.196	0.0055	0.0518
	Mid-Plane	0	0	0	0	0.169	0.0048	0.0453
II	Control	159 (23)	0.00154	105 (15.3)	0.086	0.151	0.0044	0.0429
	Exterior #1	159 (23)	0.00166	97 (14.1)	0.102	0.155	0.0043	0.0406
	Exterior #2	159 (23)	0.00156	97 (14.1)	0.069	0.146	0.0042	0.0394
	Interlaminar	159 (23)	0.00153	103 (15)	0.111	0.219	0.0061	0.0579
	Mid-Plane	159 (23)	0.00157	100 (14.5)	0.104	0.182	0.0052	0.0488
III	Control	324 (47)	0.00282	117 (16.9)	0.106	0.151	0.0044	0.0429
	Exterior #1	324 (47)	0.00316	101 (14.7)	0.100	0.155	0.0043	0.0406
	Exterior #2	303 (44)	0.00324	93 (13.5)	0.074	0.146	0.0042	0.0394
	Interlaminar	317 (46)	0.00288	110 (16)	0.131	0.224	0.0063	0.0593
	Mid-Plane	317 (46)	0.00341	93 (13.5)	0.124	0.183	0.0052	0.0490
IV	Control	386 (56)	0.00384	112 (16.3)	0.100	0.156	0.0046	0.0444
	Exterior #2	359 (52)	0.00395	92 (13.3)	0.088	0.146	0.0042	0.0394
	Interlaminar	379 (55)	0.00353	108 (15.6)	0.125	0.231	0.0065	0.0611
	Mid-Plane	379 (55)	0.00373	102 (14.8)	0.114	0.187	0.0054	0.0501
V	Control*	407 (59)	0.00353	116 (16.8)	0.112	n/a	n/a	n/a
	Exterior #2	393 (57)	0.00389	101 (14.7)	0.104	0.146	0.0042	0.0394
	Interlaminar	414 (60)	0.00417	99 (14.4)	0.144	0.255	0.0071	0.0675
	Mid-Plane	414 (60)	0.00399	103 (15)	0.140	0.197	0.0056	0.0528
VI	Exterior #2	427 (62)	0.00430	97 (14.1)	0.099	0.146	0.0042	0.0394
	Interlaminar*	414 (60)	0.00408	101 (14.7)	0.148	n/a	n/a	n/a
	Mid-Plane	427 (62)	0.00430	100 (14.5)	0.144	0.198	0.0057	0.0530
VII	Exterior #2	427 (62)	0.00477	100 (14.5)	0.086	0.146	0.0042	0.0394
	Mid-Plane	441 (64)	0.00444	100 (14.5)	0.125	0.198	0.0057	0.0530
VIII	Exterior #1*	482 (70)	0.00829	96 (14)	0.095	n/a	n/a	n/a
	Exterior #2*	476 (69)	0.00799	96 (14)	0.098	n/a	n/a	n/a
	Mid-Plane*	496 (72)	0.00519	98 (14.2)	0.137	n/a	n/a	n/a

* Specimen Fractured

Sheet resistance values of all four specimen types are compared in Figures 21 to 23. Figures 21 and 22 illustrate that sheet resistance slightly increases in the interlaminar and mid-plane specimens as stress levels increase up to the UTS, whereas sheet resistance remains relatively constant for the control and exterior samples. This is due to the fact that the highly conductive nanostrands on the exterior specimens carry the current directly across the exterior nanostrand surfaces without having to go through the thickness of the composite panel. Current must pass through the thickness of the interlaminar and mid-plane specimens because their external surfaces are the 0° plies of M55J/RS-3.

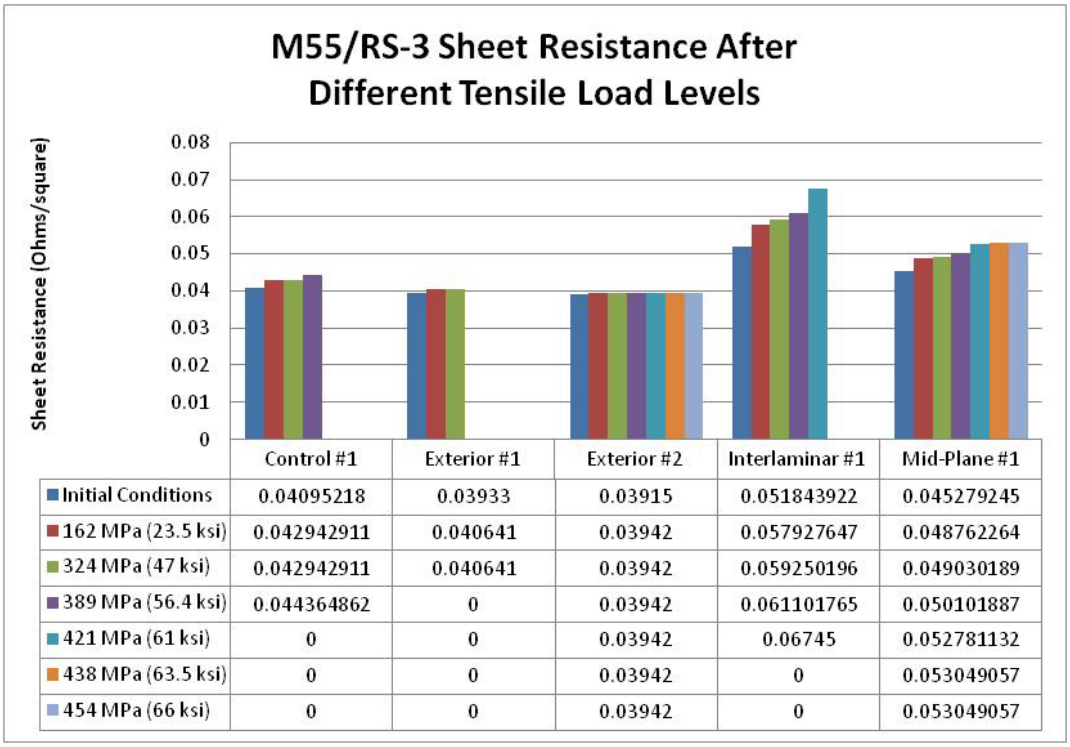

	Control #1	Exterior #1	Exterior #2	Interlaminar #1	Mid-Plane #1
Initial Conditions	0.04095218	0.03933	0.03915	0.051843922	0.045279245
162 MPa (23.5 ksi)	0.042942911	0.040641	0.03942	0.057927647	0.048762264
324 MPa (47 ksi)	0.042942911	0.040641	0.03942	0.059250196	0.049030189
389 MPa (56.4 ksi)	0.044364862	0	0.03942	0.061101765	0.050101887
421 MPa (61 ksi)	0	0	0.03942	0.06745	0.052781132
438 MPa (63.5 ksi)	0	0	0.03942	0	0.053049057
454 MPa (66 ksi)	0	0	0.03942	0	0.053049057

Figure 21. Sheet Resistance Data

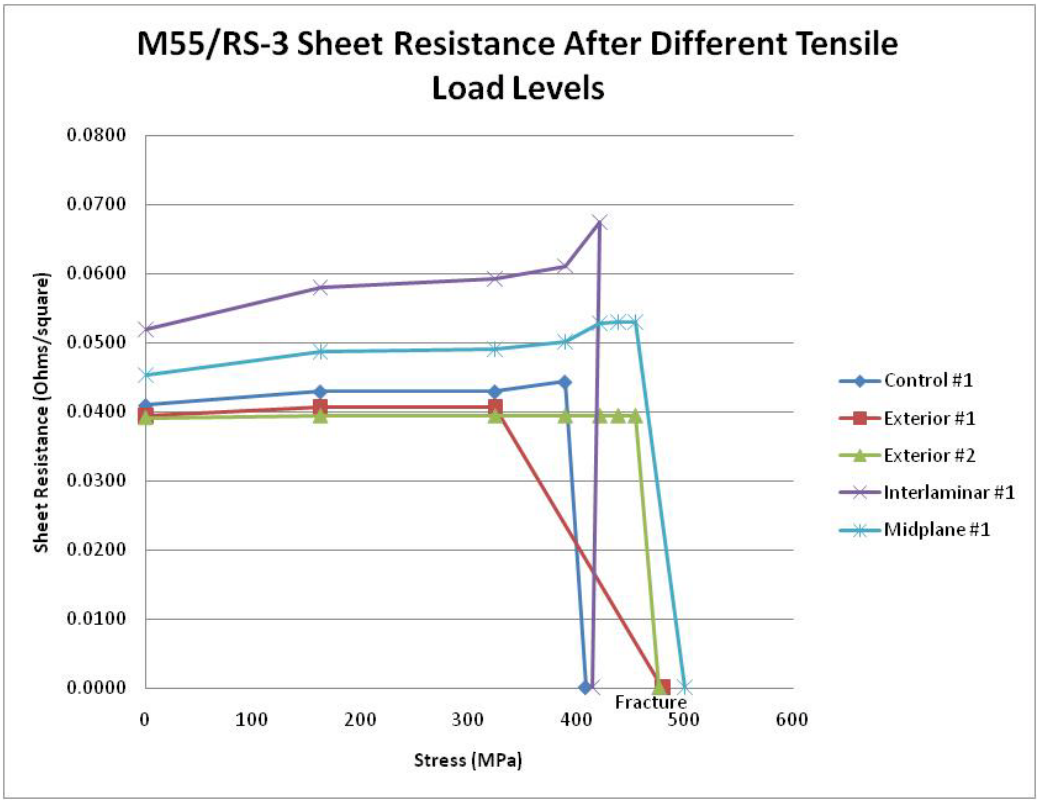

Figure 22. Sheet Resistance Plotted Against Stress

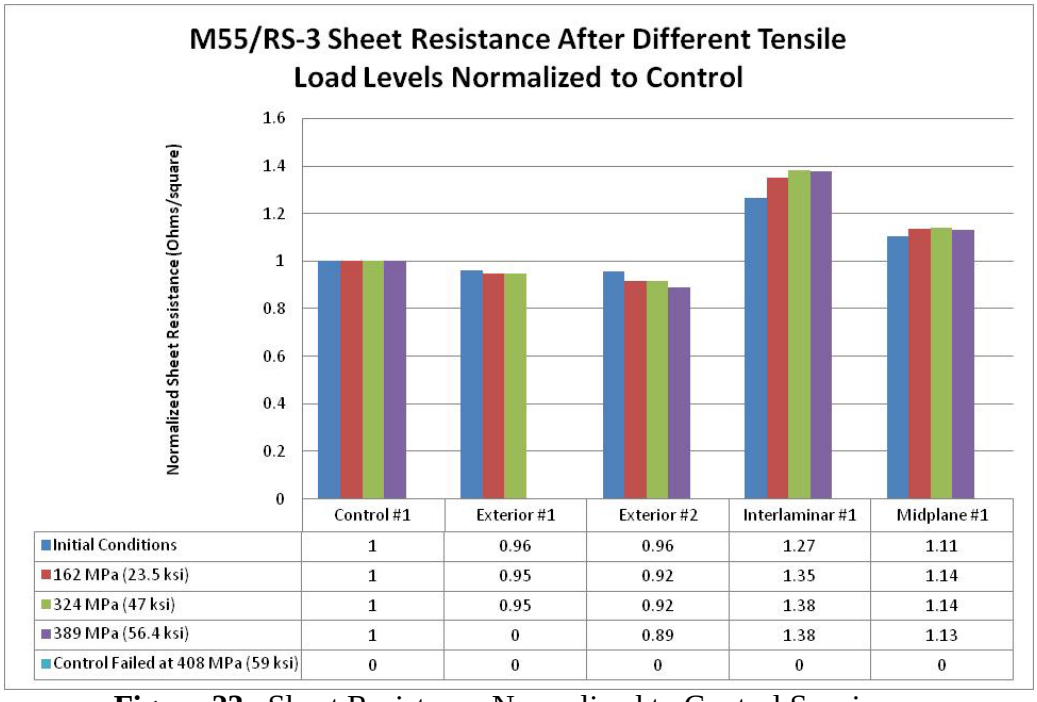

	Control #1	Exterior #1	Exterior #2	Interlaminar #1	Midplane #1
Initial Conditions	1	0.96	0.96	1.27	1.11
162 MPa (23.5 ksi)	1	0.95	0.92	1.35	1.14
324 MPa (47 ksi)	1	0.95	0.92	1.38	1.14
389 MPa (56.4 ksi)	1	0	0.89	1.38	1.13
Control Failed at 408 MPa (59 ksi)	0	0	0	0	0

Figure 23. Sheet Resistance Normalized to Control Specimen

Figure 23 shows the sheet resistance data normalized to that of the control specimen. In order to normalize the data, all specimen values of sheet resistance for each corresponding tensile loading level are divided by the control specimen's value for sheet resistance. This allows for a direct percentage comparison between the control and nanostrand specimens. Before the application of any load, the sheet resistance of the exterior specimens was 4% lower than that of the control specimen. However, the sheet resistance of the interlaminar and mid-plane specimens was 27 and 11% higher; respectively. After the application of the monotonic tensile loading conditions, the sheet resistance of the exterior specimens decreased up to 11%, whereas, the sheet resistance of the interlaminar and mid-plane specimens increased up to 38 and 14%, respectively, when compared to the control specimen. This means that as the monotonic tensile load increases, the exterior specimens were 11% more conductive than the control specimen whereas the interlaminar and mid-plane specimens were 38 and 14% less conductive. Given that conductivity is of utmost importance in the space environment in order to be able to protect against charge buildup and subsequent electrostatic discharge (ESD), the exterior specimens were superior to all in this regard.

4.3 EMI shielding

EMI shielding tests were run on each of the four different specimens before and after each monotonic tension test in order to determine how the increase in the applied stress levels up to the UTS affected their EMI shielding properties. EMI attenuation

values recorded in decibels (dB) of all four specimen types are compared in Figures 24 to 26.

The EMI attenuation data in Figures 24 and 25 clearly shows that there is negligible change to the EMI shielding properties of each of the four specimens after each sequential increase in tensile loading up to the UTS. This is an important observation because it demonstrates that the EMI shielding properties of the NS composites do not degrade under tensile loading conditions up to the UTS. Furthermore, Figure 26a shows the data normalized to the control specimen. It is evident that the exterior, interlaminar, and mid-plane specimens' EMI shielding properties are about 25, 21, and 6% better to that of the control specimen, respectively. The exterior specimens demonstrated better EMI shielding protection versus the control specimen than the interlaminar and mid-plane specimens. This means that in the harsh space environment,

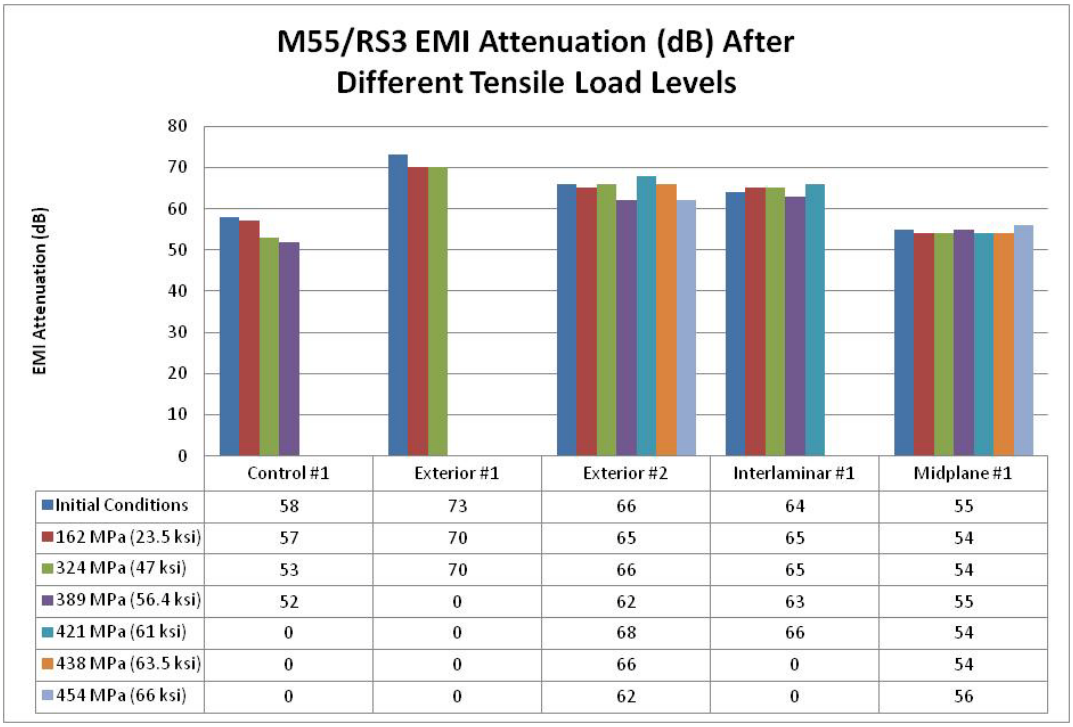

	Control #1	Exterior #1	Exterior #2	Interlaminar #1	Midplane #1
Initial Conditions	58	73	66	64	55
162 MPa (23.5 ksi)	57	70	65	65	54
324 MPa (47 ksi)	53	70	66	65	54
389 MPa (56.4 ksi)	52	0	62	63	55
421 MPa (61 ksi)	0	0	68	66	54
438 MPa (63.5 ksi)	0	0	66	0	54
454 MPa (66 ksi)	0	0	62	0	56

Figure 24. EMI Attenuation Data

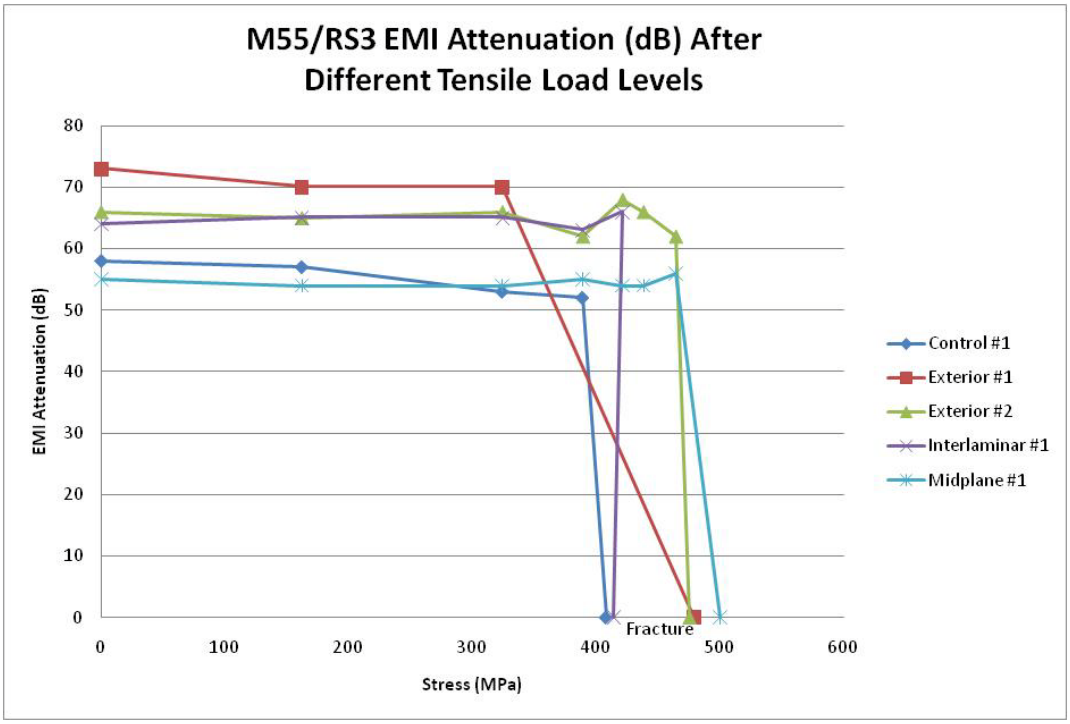

Figure 25. EMI Attenuation Plotted Against Stress to Failure

the exterior specimens outperform the other three specimens not only in terms of conductivity as previously discussed, but in terms of EMI shielding protection as well. Figure 26b shows the EMI data normalized to each specimen's initial conditions. Again, EMI shielding protection for all nanostrand specimens proved to be relatively constant when compared to each one's initial condition. Only the control specimen shows a constant decrease down to 10% EMI shielding protection when compared to its original value.

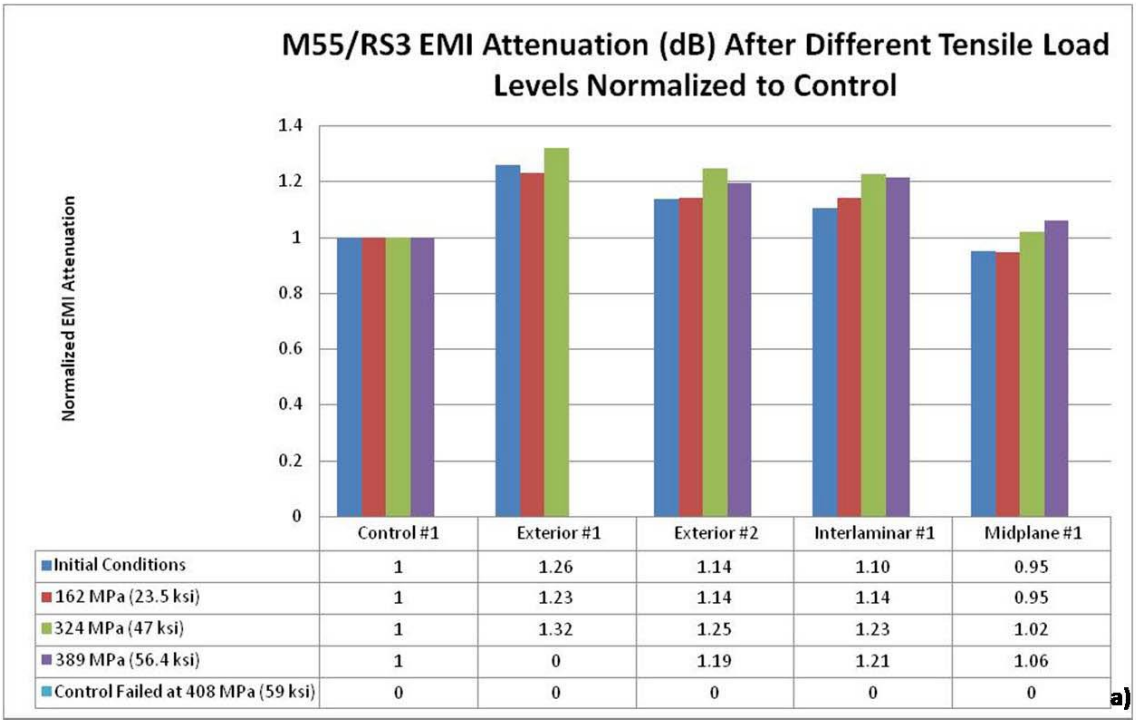

	Control #1	Exterior #1	Exterior #2	Interlaminar #1	Midplane #1
Initial Conditions	1	1.26	1.14	1.10	0.95
162 MPa (23.5 ksi)	1	1.23	1.14	1.14	0.95
324 MPa (47 ksi)	1	1.32	1.25	1.23	1.02
389 MPa (56.4 ksi)	1	0	1.19	1.21	1.06
Control Failed at 408 MPa (59 ksi)	0	0	0	0	0

a)

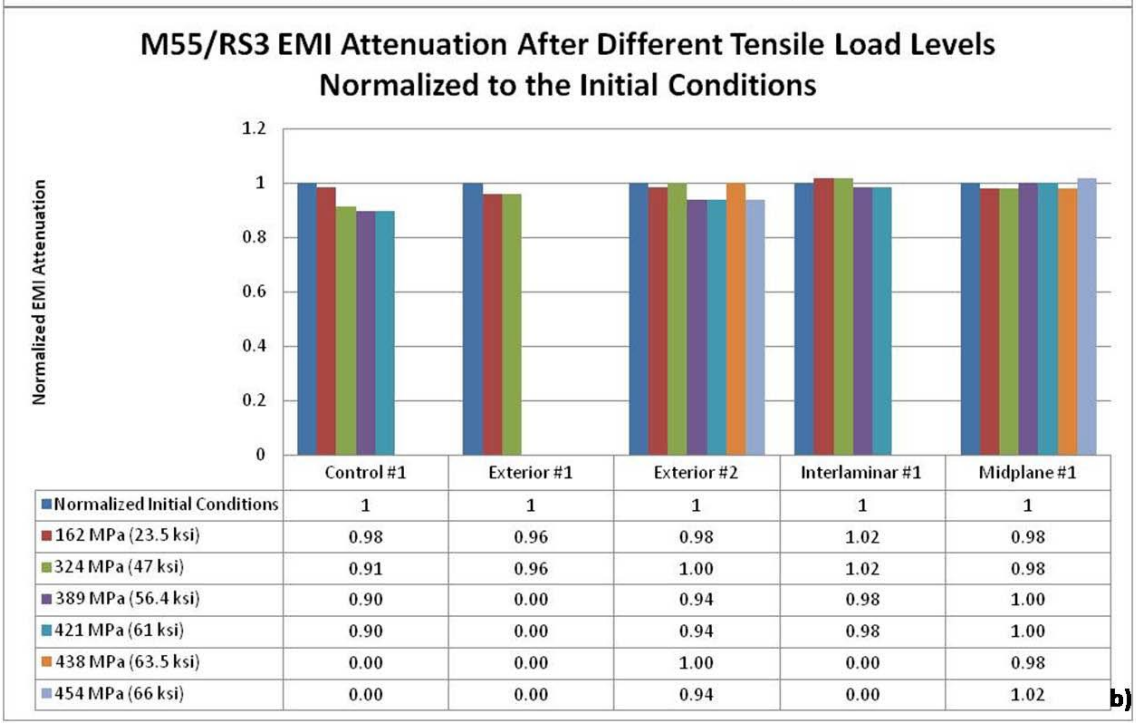

	Control #1	Exterior #1	Exterior #2	Interlaminar #1	Midplane #1
Normalized Initial Conditions	1	1	1	1	1
162 MPa (23.5 ksi)	0.98	0.96	0.98	1.02	0.98
324 MPa (47 ksi)	0.91	0.96	1.00	1.02	0.98
389 MPa (56.4 ksi)	0.90	0.00	0.94	0.98	1.00
421 MPa (61 ksi)	0.90	0.00	0.94	0.98	1.00
438 MPa (63.5 ksi)	0.00	0.00	1.00	0.00	0.98
454 MPa (66 ksi)	0.00	0.00	0.94	0.00	1.02

b)

Figure 26. Normalized EMI Attenuation Data

4.4 Simulated Space Environment

Simulated space environment tests were run on each of the four types of 7.62 cm specimens to understand what effects, if any, the harmful space environment has on the EMI shielding and mechanical properties. EMI attenuation data was recorded pre-and post-irradiation (1.2 MeV irradiation, which lasted five minutes) as shown in Figure 27a.

Pre-exposure measurements resulted in the exterior and mid-plane specimens having 17 and 41% better shielding properties, respectively, when compared to the control specimen. The interlaminar and control specimens' values were equal. This trend was different from the previous case because as mentioned in Chapter III, the EMI measurements are not absolute values but are recorded as deltas or changes. Again, this is due to the scattering on the macroscopic carbon fibers. If testing a slightly different spot on the specimen the standing wave will be scattered differently because the fibers are acting like diffraction gratings which will produce a different EMI attenuation value.

As expected, there was no change in the EMI shielding properties of the control specimen post-exposure because there were no NS present to interact with the electrons. However, all NS specimens slightly decreased their EMI shielding properties post-exposure. The exterior, interlaminar, and mid-plane specimens EMI shielding properties degraded 7, 6, and 2% respectively; however, the exterior and mid-plane specimens were still 9 and 38% better, respectively, when compared to the control specimen. The corresponding value of the interlaminar specimen was 6% less than when compared to the control specimen. These are shown in Figure 27b where the values were again normalized with the control specimen from pre-irradiation tests. While these values are not absolute as previously mentioned, they do indicate that after a five year exposure to

the space environment, the NS specimens' EMI shielding capabilities will slightly degrade. Despite this slight degradation, the NS specimens will still be at an acceptable level of EMI shielding protection.

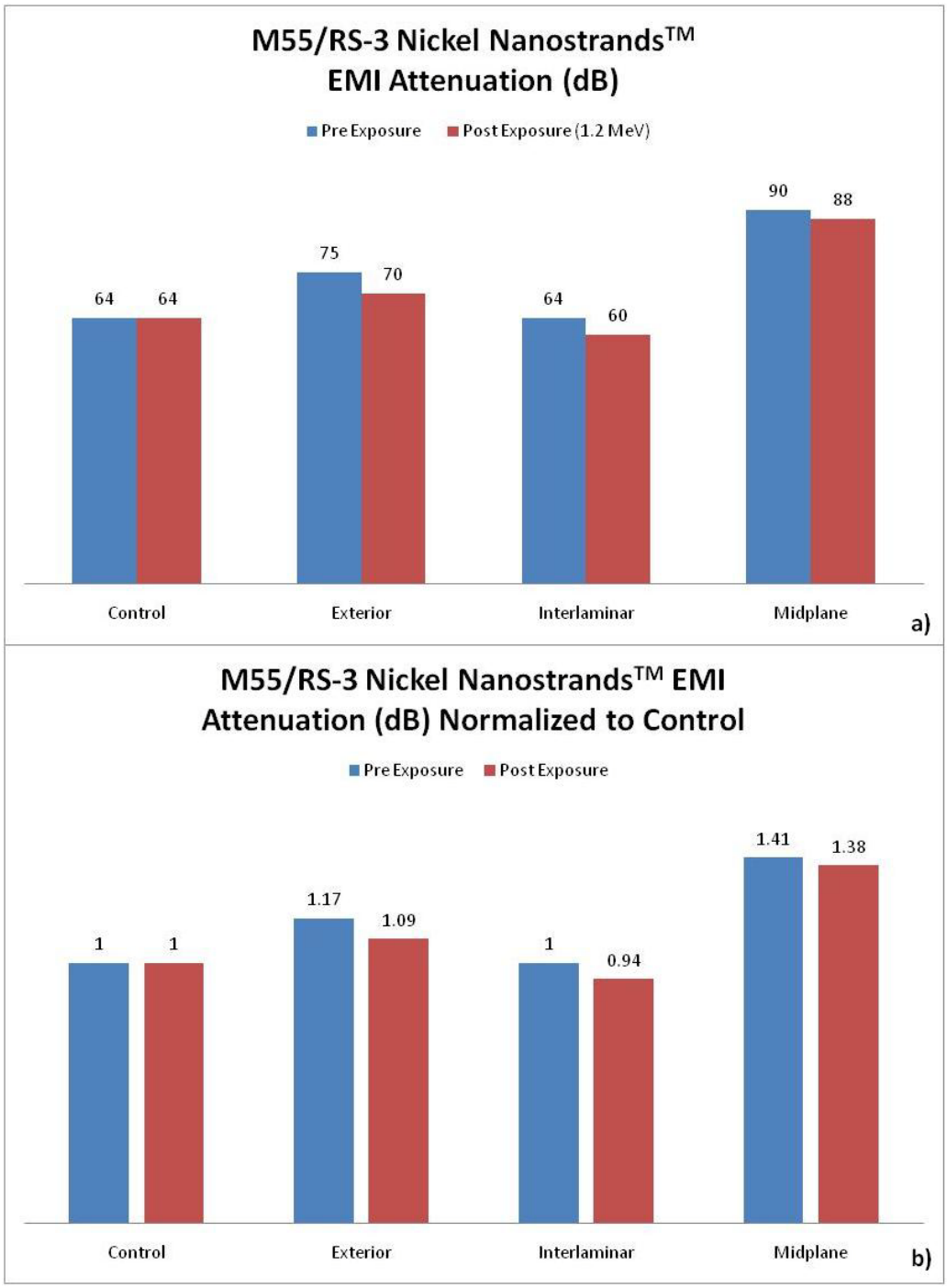

Figure 27. EMI Attenuation Pre- and Post-Exposure to Space Environment

Monotonic tension tests were also conducted on post-exposure specimens to determine what affects the simulated space environment had on the mechanical properties of all four 7.62 cm (3 in) specimens. The irradiated control specimen was loaded until it fractured at 496 MPa (72 ksi) with a corresponding Young's Modulus of 110 GPa (16 MSI). The exterior, interlaminar, and mid-plane specimens each fractured in the MTS grips at 393 (57), 221 (32), and 310 MPa (45 ksi) respectively, before reaching the expected UTS of between 414 (60) to 496 MPa (72 ksi) as demonstrated by the 15.25 cm (6 in) specimens. However, when compared to the 15.25 cm specimens, the irradiated 7.62 cm control specimen fractured within the expected stress range with an equivalent Young's Modulus. Table 5 shows Young's Modulus, UTS, and strain comparisons between the 15.25 and 7.62 cm specimens. Figure 28 graphically compares the Young's Modulus of the 7.62 cm irradiated specimens to that of the non-irradiated 15.25 cm specimens and shows that throughout all monotonic tensile loading conditions, the average moduli remains relatively constant. Stress-strain curves for all 7.62 cm specimens and loading levels are shown in Appendix B.

Table 5. Young's Modulus (E), UTS, and Strain Comparisons

Specimen	Unexposed UTS MPa (ksi)	Irradiated UTS MPa (ksi)	Unexposed Average E GPa (MSI)	Irradiated Average E GPa (MSI)	Unexposed Strain (mm/mm)	Irradiated Strain (mm/mm)
	15.25 cm	7.62 cm	15.25 cm	7.62 cm	15.25 cm	7.62 cm
Control	408 (59)	496 (72)	112 (16.3)	110 (16)	0.0035*	0.0038
Exterior	475 (69)	393 (57)**	98 (14.2)	99 (14.4)	0.0022	0.0022*
Interlaminar	414 (60)	221 (32)**	104 (15.1)	106 (15.4)	0.0042	0.0042*
Mid-Plane	500 (72.5)	310 (45)**	99 (14.4)	100 (14.5)	0.0032	0.0032*

* Ultimate Strain

** Fractured in the MTS grips

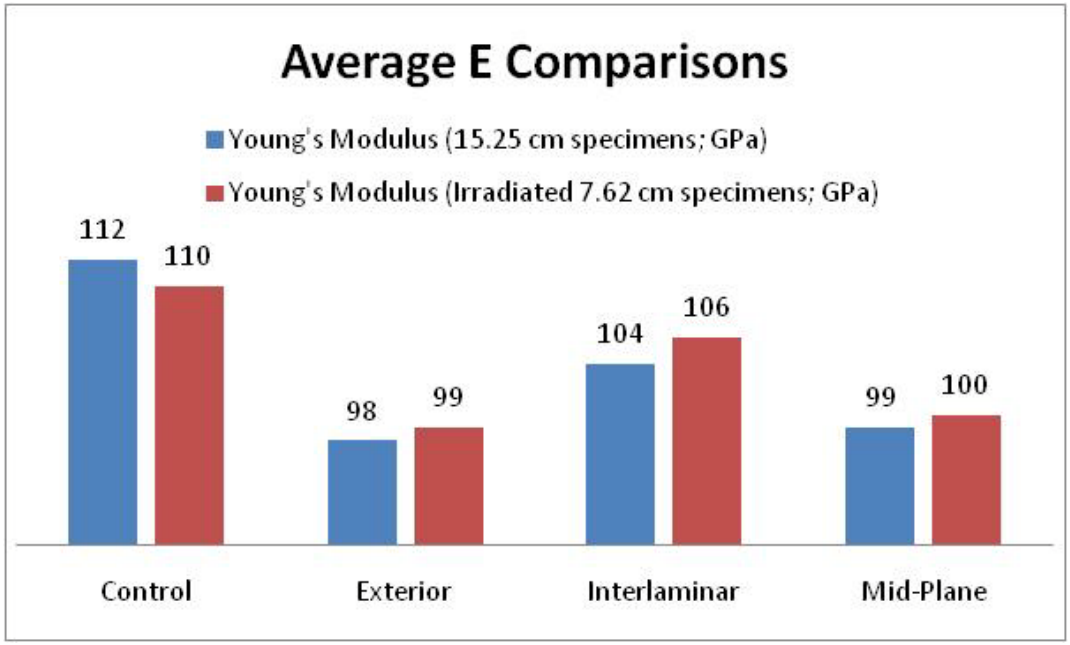

Figure 28. Modulus Comparisons

The 7.62 cm control, exterior, interlaminar, and mid-plane specimens, which fractured prematurely in the MTS grips, demonstrated equivalent average moduli to those of their 15.25 cm counterparts. The ultimate strain at the precise point of fracture of the 7.62 cm NS specimens also matches that of their 15.25 cm counterparts at the same levels of stress. The 7.62 cm control specimen fractured at 496 MPa (72 ksi), which is 88 MPa (13 ksi) larger than the 15.25 control specimen; however the ultimate strain of the 15.25 cm control specimen at a UTS of 407 MPa (59 ksi) matches strain of the 7.62 cm control specimen. These facts, coupled with the 7.62 cm control specimen fracturing as expected, and by utilizing the equation:

$$\sigma = E\varepsilon \qquad (4)$$

in which σ = stress; E = modulus; ε = strain, allows for the extrapolation that the 7.62 cm exterior, interlaminar, and mid-plane NS specimens fracture stresses would have been

within the expected stress range had they not broken in the MTS grips. This means that the space environment does not affect the mechanical properties of all four specimens.

4.5 Failure Mechanisms

Failure Mechanisms were investigated through an optical microscope and the SEM to determine if there are different modes of failure between the four different systems. This section will systematically walk through each system's mode of failure under monotonic tensile loading. After the tension testing, all specimens showed failure at similar places. The 15.25 cm (6 in) control, exterior, interlaminar, and mid-plane specimens are shown in Figure 29. In order to establish a basis for comparison throughout the remainder of the chapter, the first system under optical observation was the control panel.

The M55J/RS-3 control specimen has a symmetric balanced lay-up consisting of eight layers of carbon fiber M55J with a $[0/90/\pm45]_s$ orientation and does not have a layer of nickel nanostrands™. The first step in the failure mechanism of a typical $[0/90/\pm45]_s$ composite consists of transverse matrix cracking in the 90° layer. These cracks increase in density up to a limiting value or the characteristic damage state. Thereafter, as the load increases, cracking starts in the ± 45 plies, precipitating ultimate failure [7]. Figure 30 shows this is indeed the case. The 90° layers fractured first which lead to the ±45 plies shear failure and then ultimate failure of the specimen.

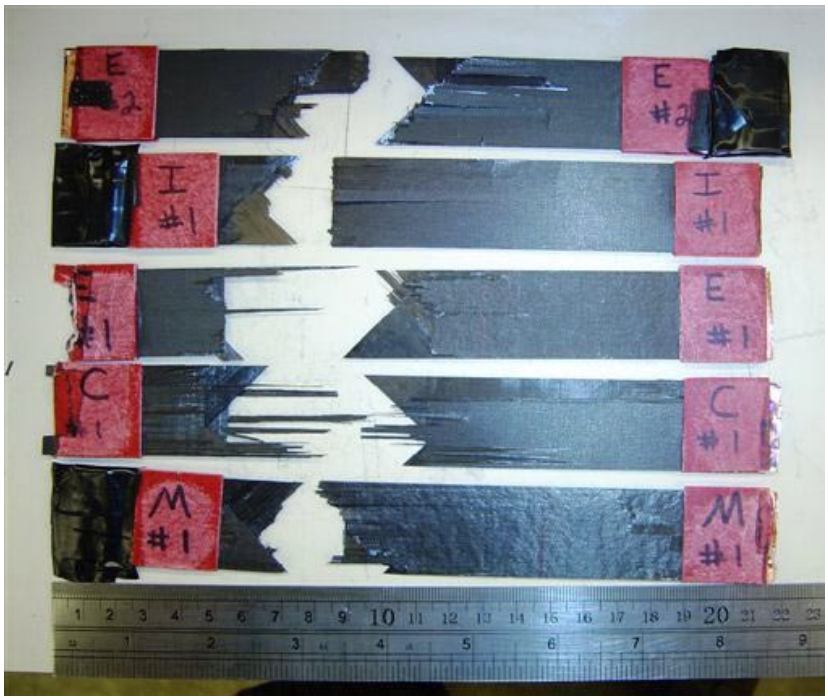

Figure 29. 15.25 cm Specimens After Testing

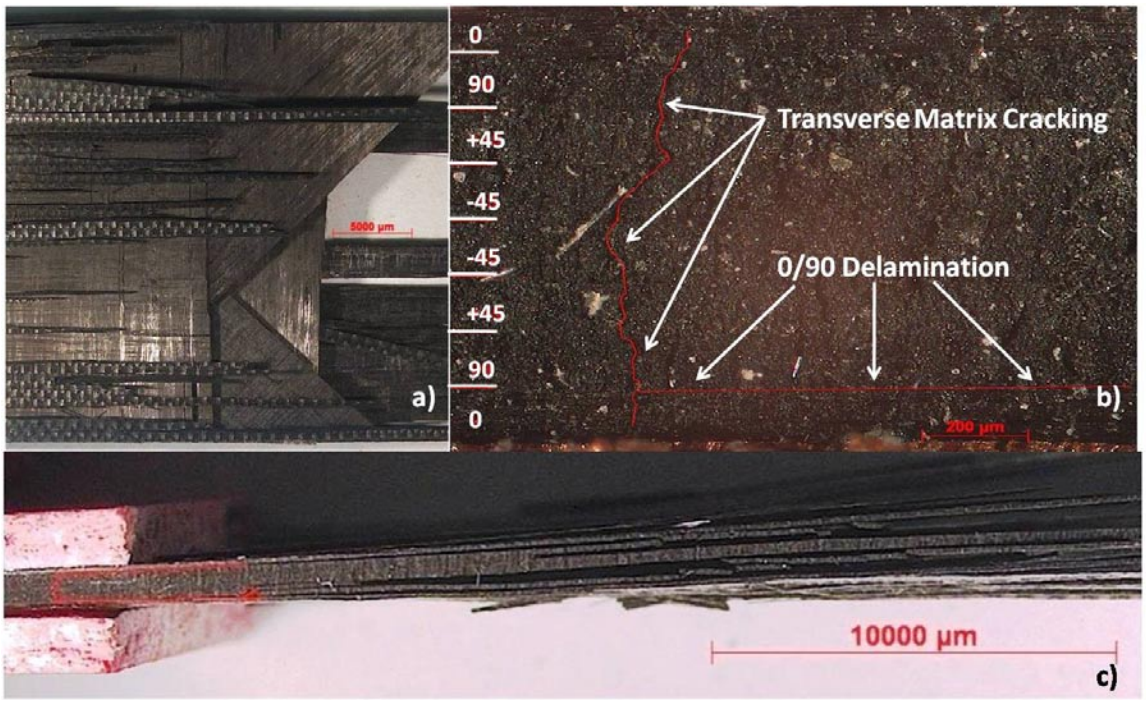

Figure 30. Fractured Control Specimen: a) width view; b) thickness view at 100x; c) thickness view at 5x magnification

In order to accurately determine the modes of failure the sample must be analyzed from the thickness view as shown in Figures 30 b and c. From this viewpoint, the area highlighted with arrows depicts the origin of the failure. Scanning electron microscope (SEM) pictures were taken of the highlighted area to determine the details of the failure mechanisms as shown in Figure 31. As mentioned earlier, the 90° fibers broke which caused delamination in the 0/90 ply which precipitated transverse matrix cracks from the 90° ply to the ±45 ply which caused delamination directly resulting in the ±45 shear and specimen failure.

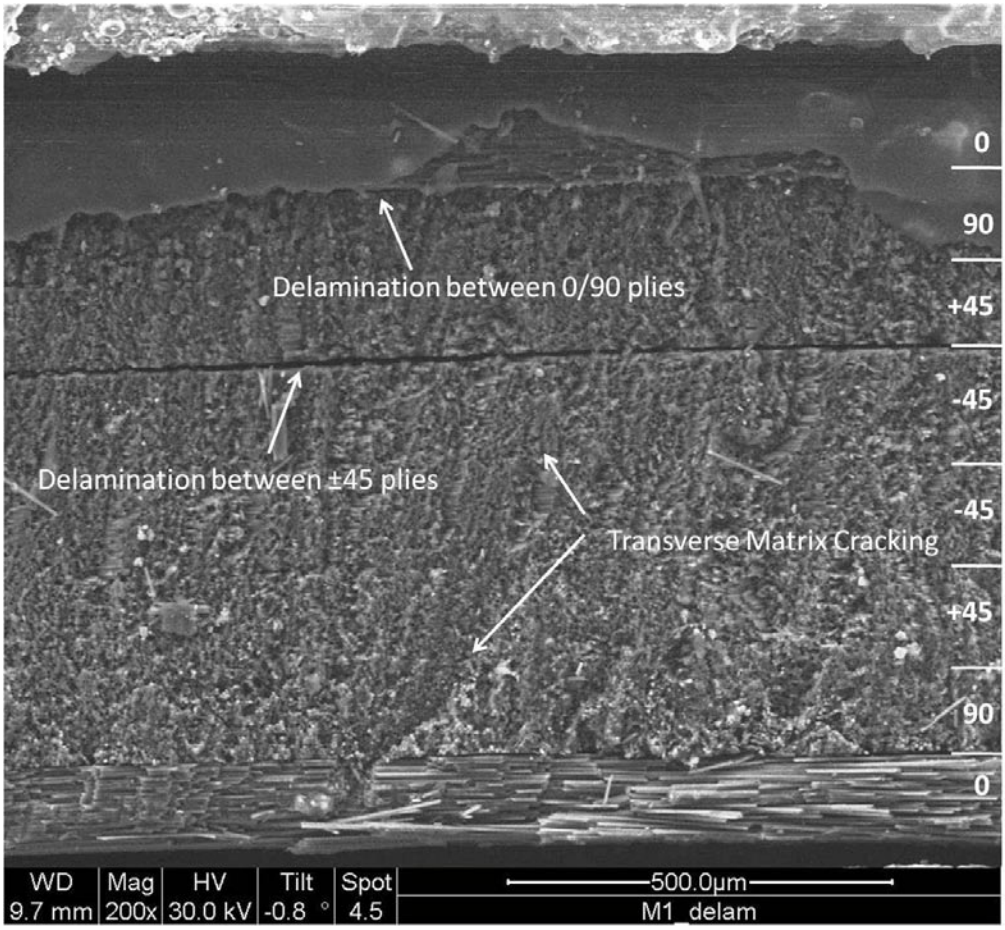

Figure 31. SEM Picture of Control Specimen Origin of Fracture

The M55J/RS-3 mid-plane specimen has a symmetric balanced lay-up consisting of eight layers of carbon fiber M55J with a $[0/90/\pm45]_s$ orientation combined with a layer of nickel nanostrands™ located at the mid-plane of the specimen as previously indicated. Figure 32 shows the width view as well as the thickness view of the fractured specimen. Again it is evident that the mid-plane specimen failed in the same manner as the control specimen. SEM pictures were taken to validate the mode of failure as shown in Figures 33 and 34.

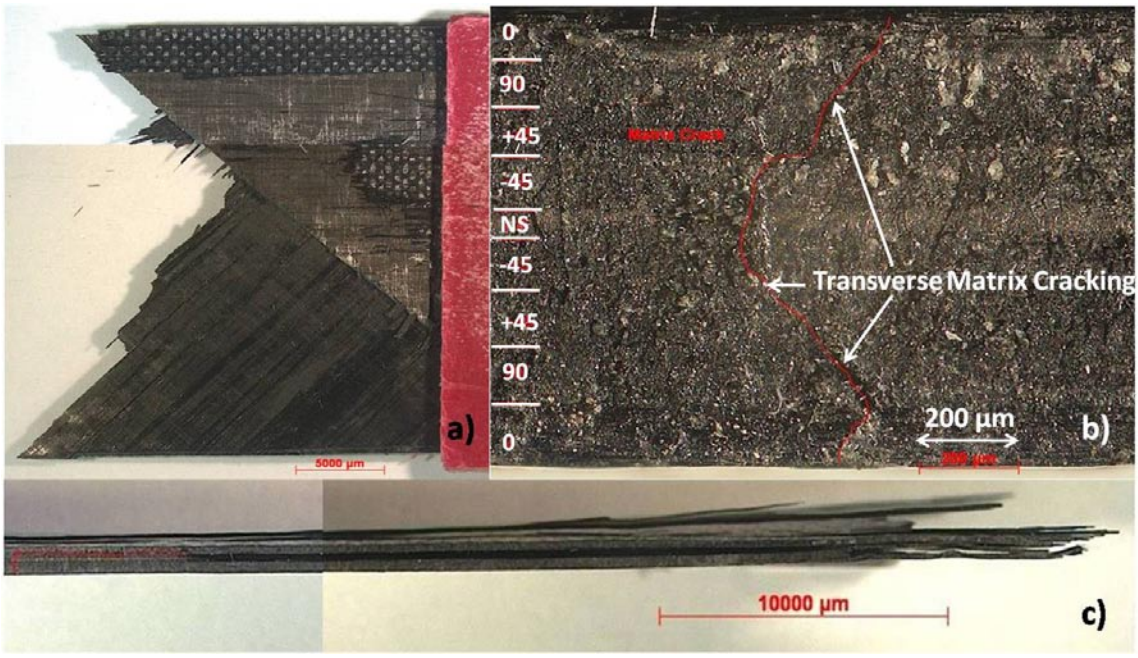

Figure 32. Fractured Mid-Plane Specimen: a) width view; b) thickness view at 100x; c) thickness view at 5x magnification

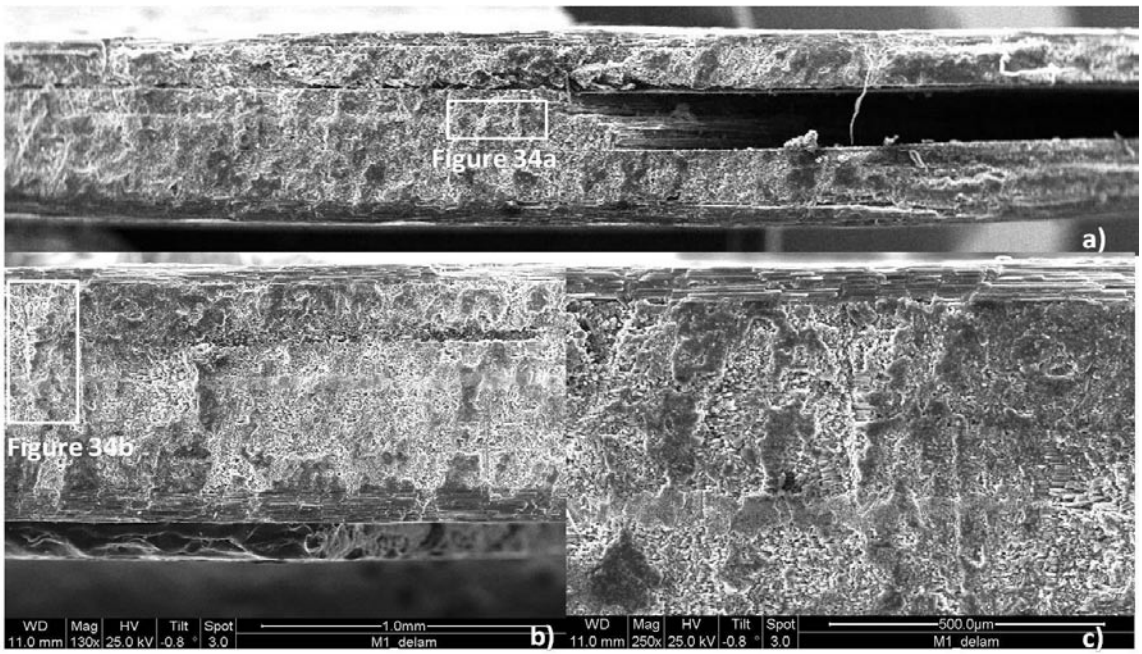

Figure 33. SEM photos of the Mid-Plane Specimen: a) fracture surface; b) origin of delamination leading to fracture; c) 250x view of origin of fracture

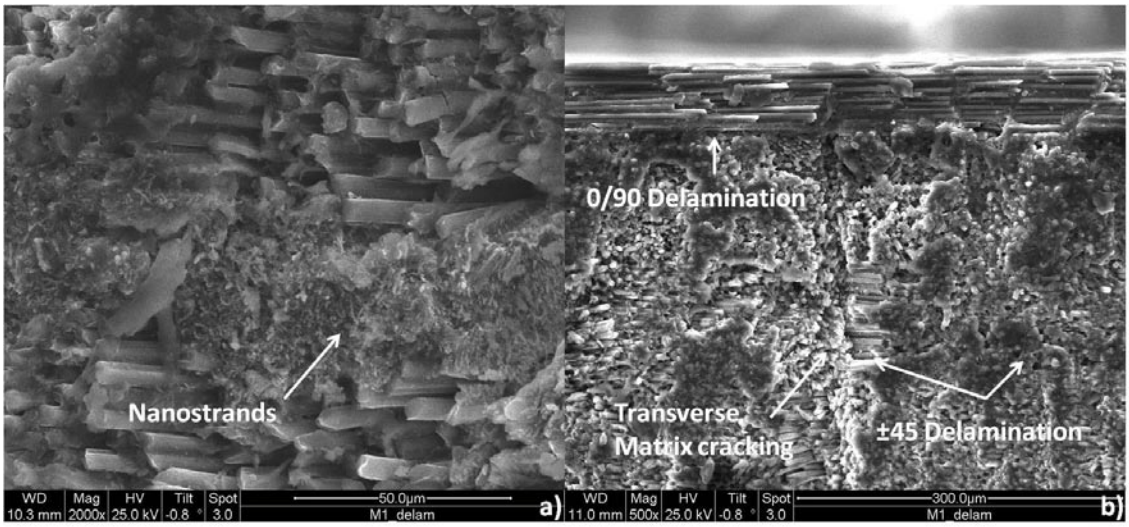

Figure 34. Additional SEM photos of the Mid-Plane Specimen: a) nickel nanostrands™ intact prior to failure; b) 500x view of origin of fracture

The SEM pictures of the mid-plane sample indicate failure in the same manner as the control sample with the nickel nanostrands™ completely intact up to failure. The 90° plies failed which resulted in delamination between the 0/90 plies which lead to

transverse matrix cracking causing delamination in the ±45 plies that resulted in the shear failure of the composite. Complete ±45 shear and specimen failure is shown in Figure 33a. It is important to note that the nanostrands were undamaged up until the point of fracture as indicated in Figure 34a. This fact leads to the conclusion that because the nanostrands were intact until fracture, the composite would maintain its ESD and EMI shielding capabilities until UTS, which was proved via the monotonic tension tests in conjunction with the EMI and resistivity measurements.

The M55J/RS-3 interlaminar specimen has a symmetric balanced lay-up consisting of eight layers of carbon fiber M55J with a $[0/90/\pm45]_s$ orientation combined with 4 layers of alternating nickel nanostrands™ evenly dispersed as previously indicated. Figure 35 shows the width view as well as the thickness view of the fractured surface. Again it is evident that the interlaminar specimen failed in the same manner as the control and mid-plane specimens. SEM pictures were taken to validate the mode of failure as shown in Figures 36 and 37.

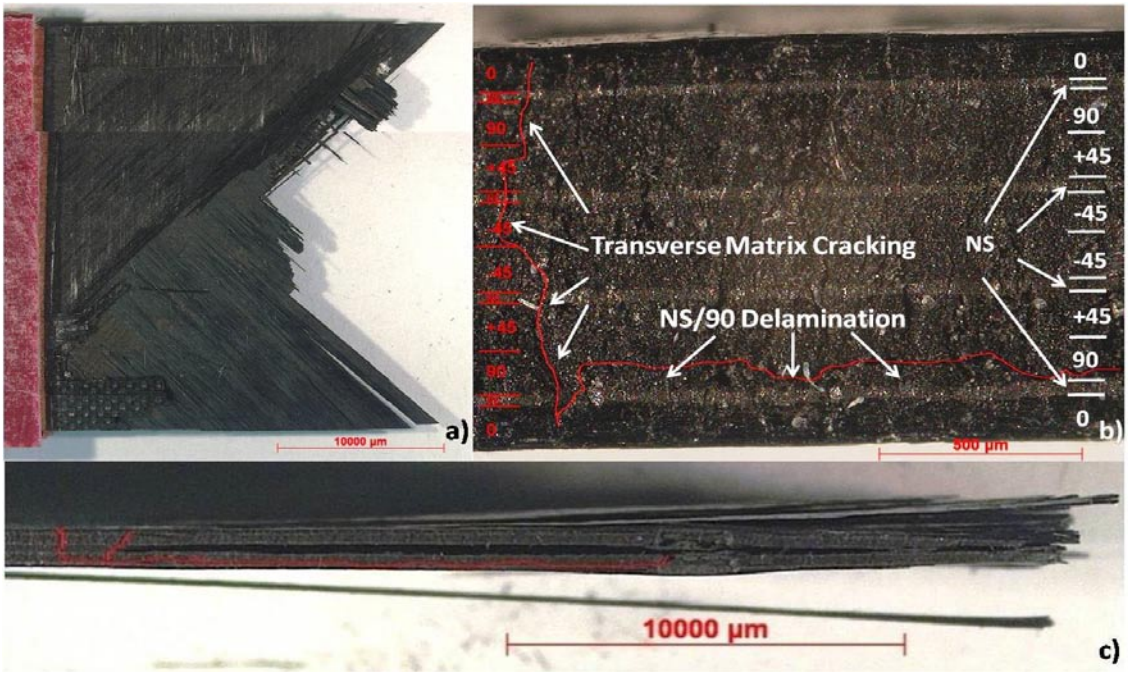

Figure 35. Fractured Interlaminar Specimen: a) width view; b) thickness view at 100x; c) thickness view at 5x magnification

The SEM pictures of the interlaminar sample indicate failure in the same manner as the control and mid-plane specimens with the nickel nanostrands^{TM} completely intact up to failure. The 90° plies failed which resulted in delamination between the nanostrand/90 plies which lead to transverse matrix cracking causing delamination in the ±45 plies that resulted in the shear failure of the composite. Complete ±45 shear and specimen failure is shown in Figure 36a. It is important to note that the nanostrands again, were undamaged up until the point of fracture as indicated in Figure 37b. This fact further enables the conclusion that because the nanostrands were intact until fracture, the composite would maintain its ESD and EMI shielding capabilities until UTS, which was proved via the monotonic tension tests combined with the EMI and resistivity measurements.

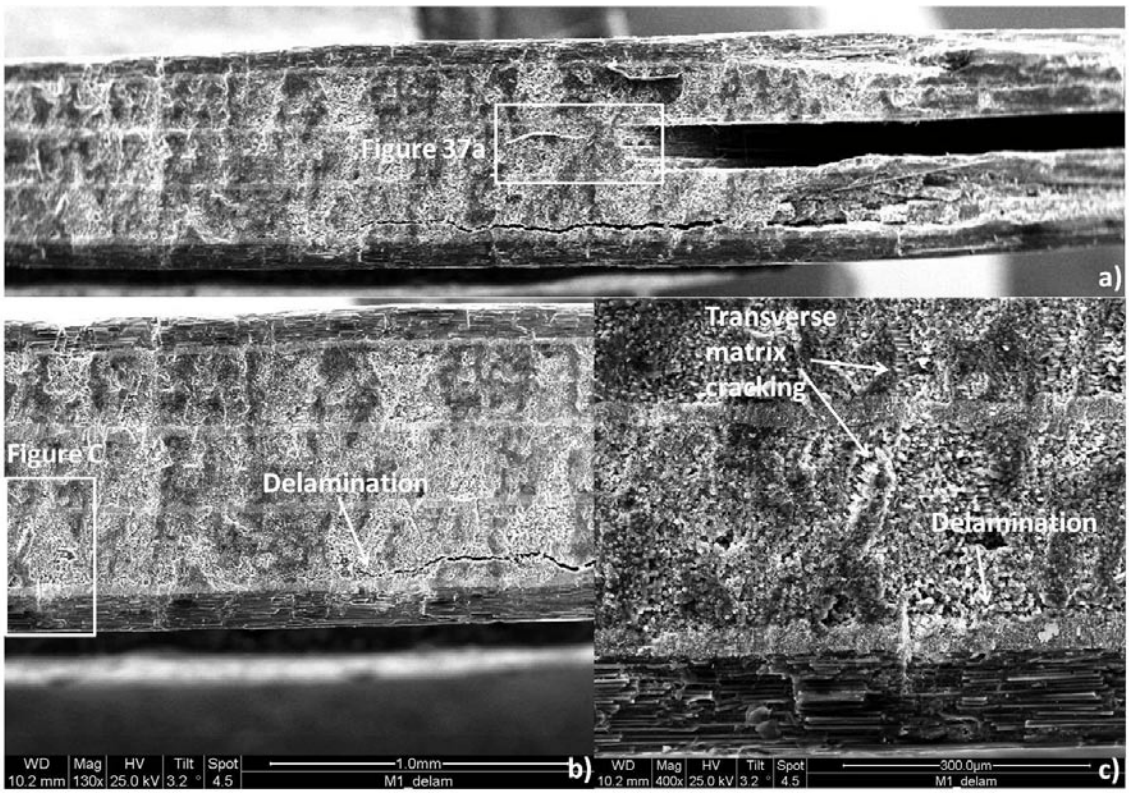

Figure 36. SEM photos of the Interlaminar Specimen: a) fracture surface; b) origin of delamination leading to fracture; c) 500x view of origin of fracture

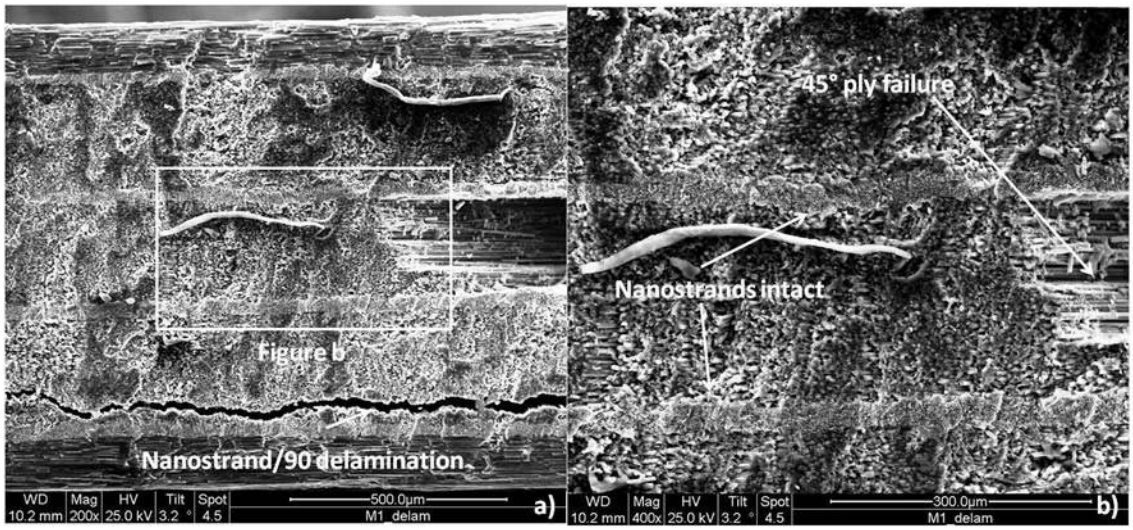

Figure 37. Additional SEM photos of the Interlaminar Specimen: a) 200x view of fracture surface; b) nickel nanostrands™ intact prior to failure

The two M55J/RS-3 exterior specimens had a symmetric balanced lay-up consisting of eight layers of carbon fiber M55J with a $[0/90/\pm45]_s$ orientation combined with 2 layers of nickel nanostrands™ as the first and last plies as previously indicated. Figures 38 and 39 show the width view and the thickness view of the fractured surfaces from both exterior samples. Again it is evident that the exterior specimens failed in the same manner as the control, mid-plane, and interlaminar specimens. SEM pictures were taken to validate the mode of failure of both exterior specimens as shown in Figures 40 to 43.

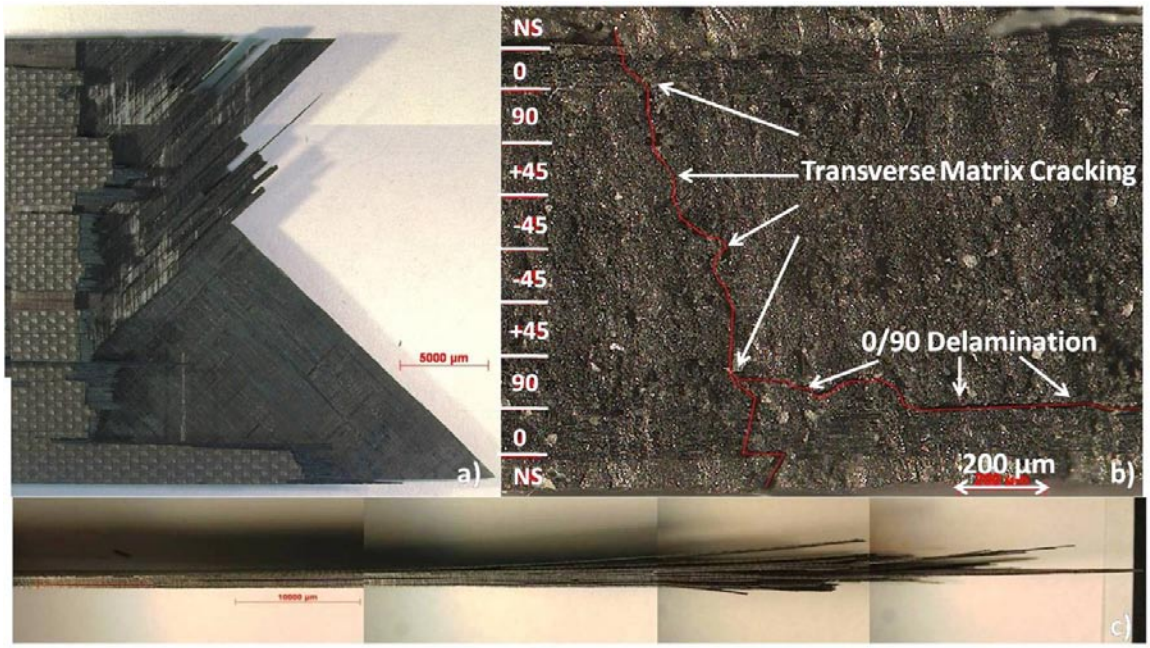

Figure 38. Fractured Exterior #1 Specimen: a) width view; b) thickness view at 100x; c) thickness view at 5x magnification

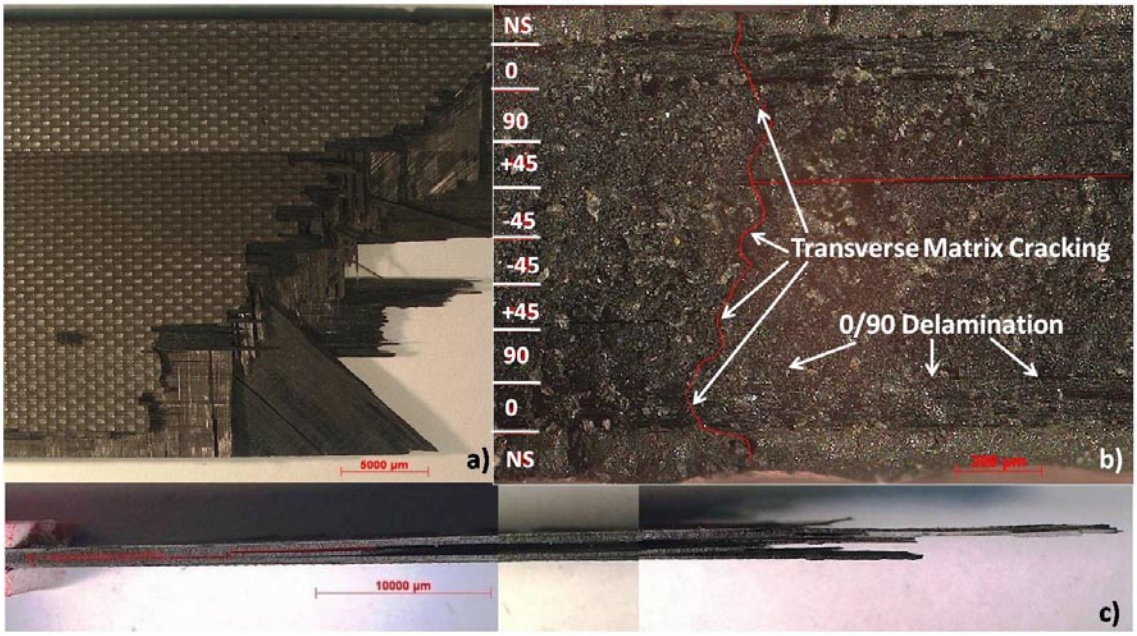

Figure 39. Fractured Exterior #2 Specimen: a) width view; b) thickness view at 100x; c) thickness view at 5x magnification

The SEM pictures of the two exterior samples indicate failure in the same manner as the control, mid-plane, and interlaminar specimens with the nickel nanostrands™ completely intact up to failure. The 90° plies failed first which resulted in delamination between the 0/90 plies which lead to transverse matrix cracking causing delamination in the ±45 plies that resulted in the shear failure of the composite. Complete ±45 shear and specimen failure on both specimens is shown in Figures 40 and 41. It is important to note that the once again, the nanostrands were undamaged up until the point of fracture. This fact further cements the conclusion that because the nanostrands were intact until fracture, the composite would maintain its ESD and EMI shielding capabilities until UTS, which was proved via the monotonic tension tests coupled with the EMI and resistivity measurements.

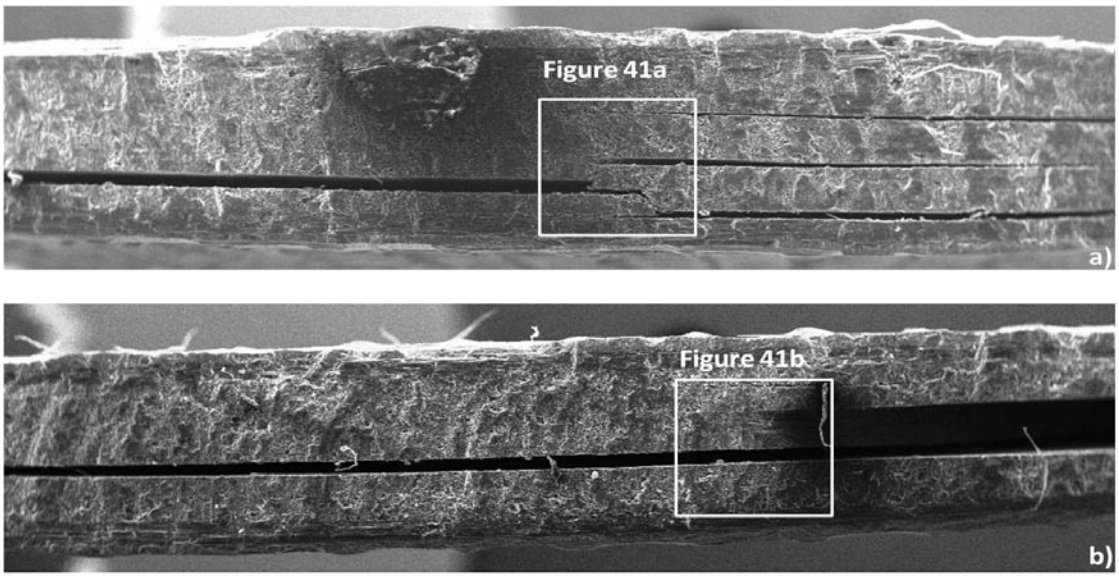

Figure 40. SEM Pictures of Fractured Exterior Specimens at 50x Magnification: a) exterior #1; b) exterior #2

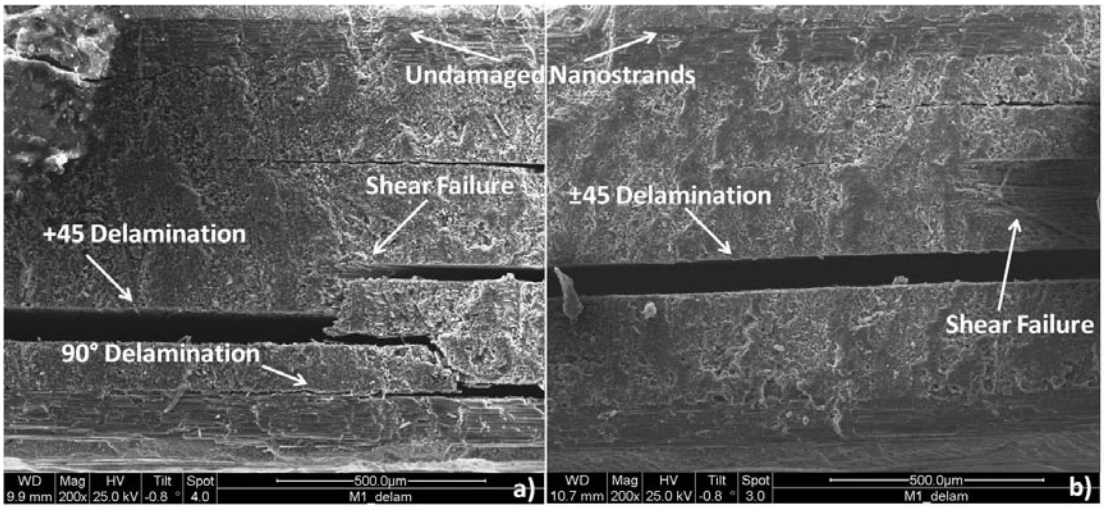

Figure 41. SEM Pictures of Fractured Exterior Specimens at 200x Magnification: a) exterior #1; b) exterior #2

A final SEM analysis on the irradiated 7.62 cm (3 in) specimens was required in order to determine if exposure to the space environment alone causes any unwanted damage to the composites such as matrix cracking or more importantly, delamination between plies. Again, each sample was irradiated with 1.2 MeV electrons which were

scanned across the surface utilizing a magnetic steering magnet in a 1.25 inch diameter spot across the midsection of the specimen. The total electron fluence was 1E14 electrons/cm^2; however, the interlaminar sample was accidentally irradiated with twice the fluence at 2E14 electrons/cm^2. Specimens were irradiated for approximately five minutes which produced a simulated five year exposure to the space environment. After the specimens were irradiated, they were each cut in half lengthwise by a diamond wet saw in order to examine the irradiated sections for any damage. The SEM analysis of each of the four specimens post exposure to the space environment resulted in no damage to any of the specimens. There was no evidence of delamination or matrix cracking after irradiation as shown in Figures 42 to 45.

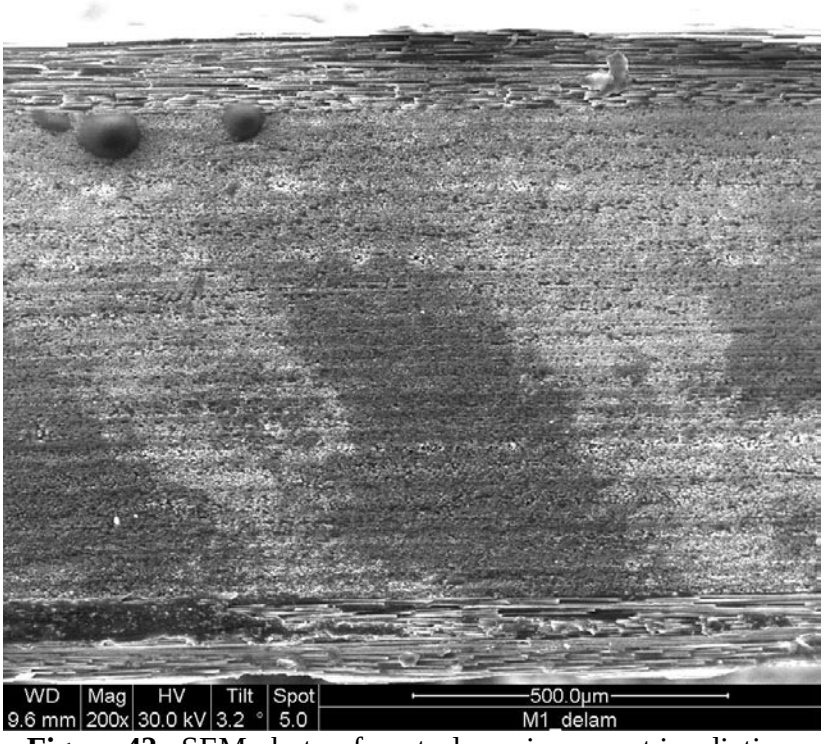

Figure 42. SEM photo of control specimen post irradiation

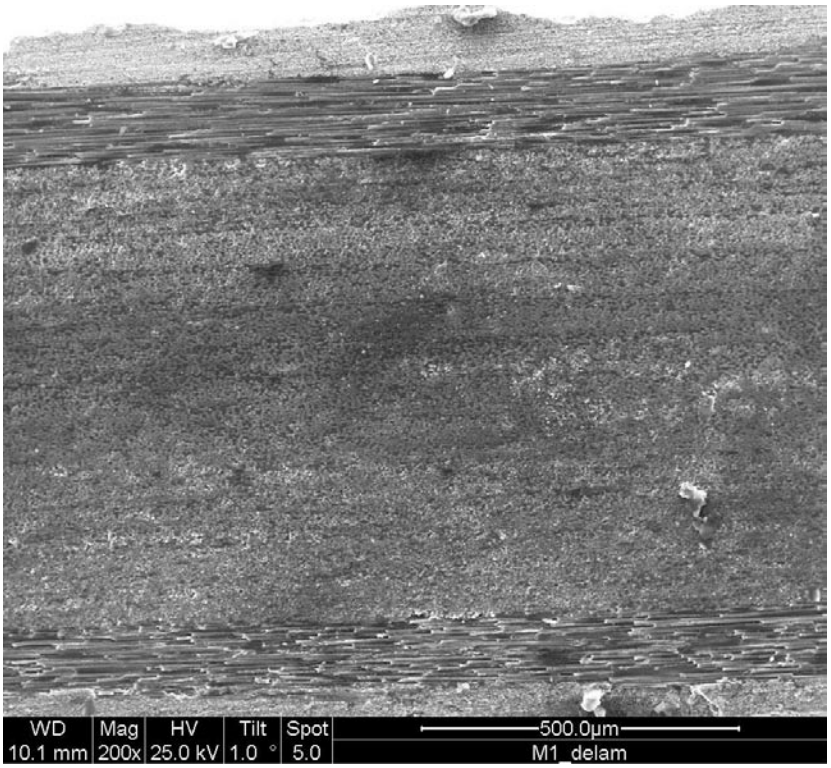

Figure 43. SEM photo of exterior specimen post irradiation

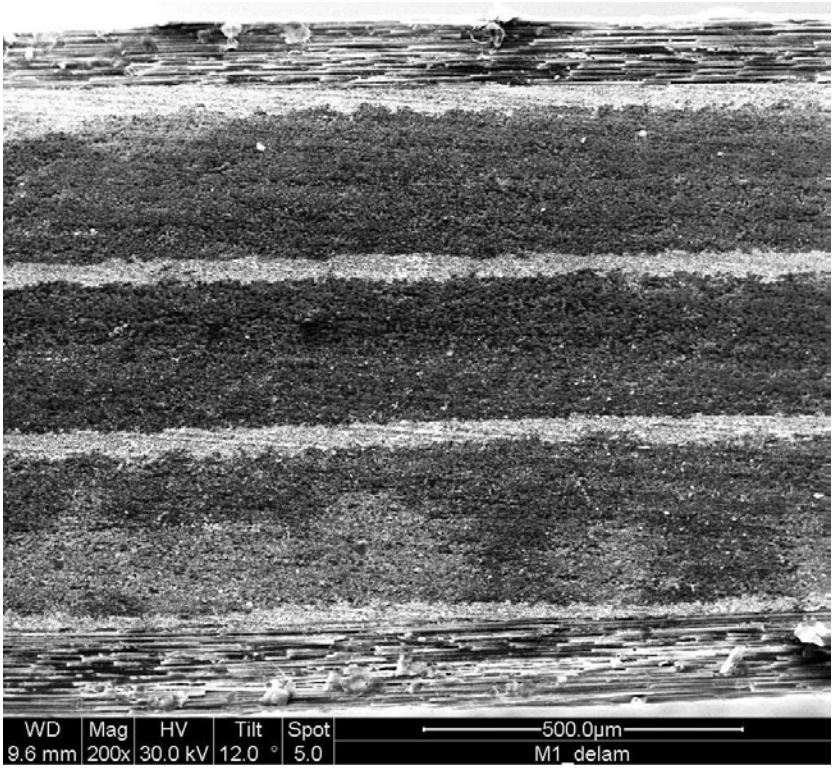

Figure 44. SEM photo of interlaminar specimen post irradiation

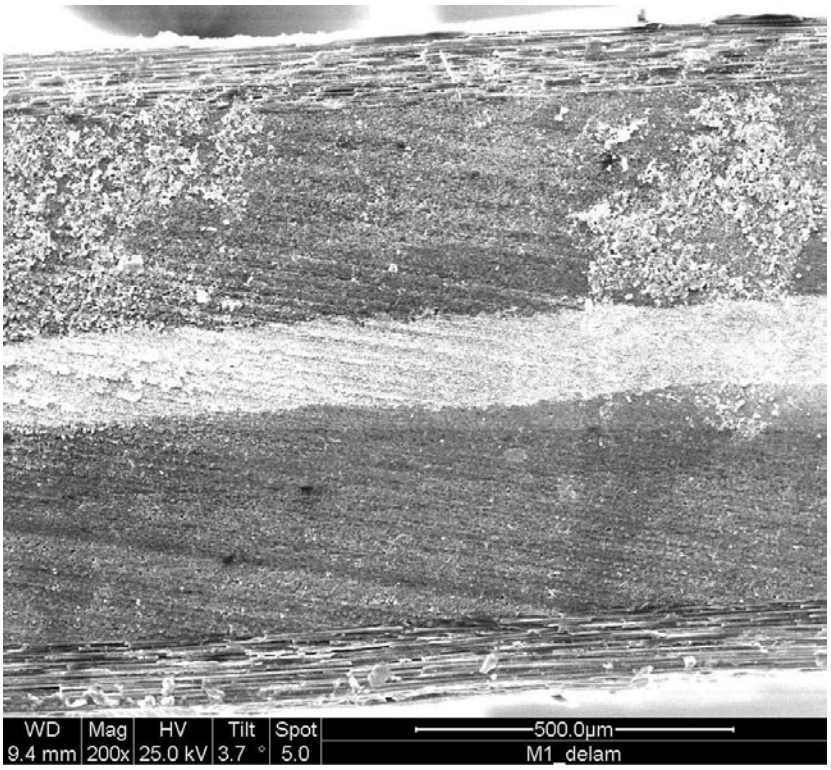

Figure 45. SEM photo of mid-plane specimen post irradiation

V. Conclusions and Recommendations

This chapter begins with a brief summary of the experiments conducted for this study and the analysis of their results. Next, the final conclusions of this study are presented and explained. Finally, potential topics for future studies are suggested.

5.1 Summary

The main objective of this study was to determine if a M55J/RS-3 composite (i.e. graphite fiber in a toughened polycyanate resin matrix) combined with nickel nanostrands™ would be suitable for use in satellite structure applications while simultaneously providing ESD and EMI shielding protection from the harmful space environment. This would further reduce the satellites' overall dry weight and eliminate the need for expensive additional secondary shielding materials to be applied, therefore dramatically reducing manufacturing and launch costs. Four different composite configurations were tested for their ultimate strength and EMI shielding protection properties before and after exposure to a representative five year space environment. The four configurations tested were a baseline control panel of M55J/RS-3 and three systems with different layers of nickel nanostrands™ added to the control specimen: exterior, interlaminar, and mid-plane. Please remember that the four different composite configurations are detailed in Table 3 and Figure 20. These four systems were additionally tested for their EMI shielding protection and resistivity properties before, during and after monotonic tension tests of increasing loads up to fracture to determine what affect the tensile loading conditions have on EMI shielding protection and resistivity. The test set up for these experiments was detailed in Chapter III.

5.2. Conclusions

From the analysis of the test results, the following conclusions can be drawn:

A. Effect of monotonic tensile loading on EMI shielding protection and sheet resistance

- The UTS was within a range of 414 MPa (60 ksi) to 496 MPa (72 ksi) as demonstrated by the four different composite configurations and the nanostrands did not have any effect on the strength (UTS) or stiffness (Young's modulus, E) of the baseline M55J/RS-3 composite.
- EMI shielding protection capability of the four different specimens was reasonably constant throughout the intermittent tensile loading conditions up to failure. The exterior specimens performed better than the interlaminar and mid-plane specimens and were 25% better at EMI shielding protection than the control specimen.
- Sheet resistance measurements before and after the application of increasing monotonic tensile loading conditions showed that exterior specimens are better at ESD protection. The interlaminar and mid-plane specimen's sheet resistance steadily increases after each monotonic tensile load whereas the exterior specimen's sheet resistance is constant. This is due to the fact that the highly conductive nanostrands on the exterior specimens carry the current directly across the external nanostrand surfaces without having to go through the thickness of the composite panel. Current must pass through the thickness of the interlaminar and mid-plane specimens because their external surfaces are the 0° plies of

M55J/RS-3. Since conductivity is of utmost importance in the space environment in order to be able to protect against charge buildup and subsequent ESD, the exterior specimens are superior to all in this regard.

B. Effect of space environment on UTS, Young's modulus, and EMI shielding protection

- The UTS and Young's modulus of the specimens does not change after exposure to the space environment. This is most likely due to the fact that the nickel nanostrands™ are able to provide protection from the composite's interaction with charged particles. This is crucial in the harmful space environment because the spacecraft structure must be strong (high UTS) and stiff (high E).
- The EMI shielding protection capabilities of the three nickel nanostrand™ specimens slightly degrades (2 ~ 7%) after exposure to a five year simulated space environment, however they still provide adequate EMI shielding protection.

C. Failure mechanisms

- The failure mechanisms for the four specimens are the same, regardless of composite configuration. The 90° plies failed first, which resulted in delamination between the 0/90 plies which leads to transverse matrix cracking causing delamination in the ±45 plies that resulted in ±45 shear and ultimate failure of the composite as shown schematically in Figure 46. It is important to note that the nanostrand layers remain intact up until

composite fracture which will be crucial in the harmful space environment.

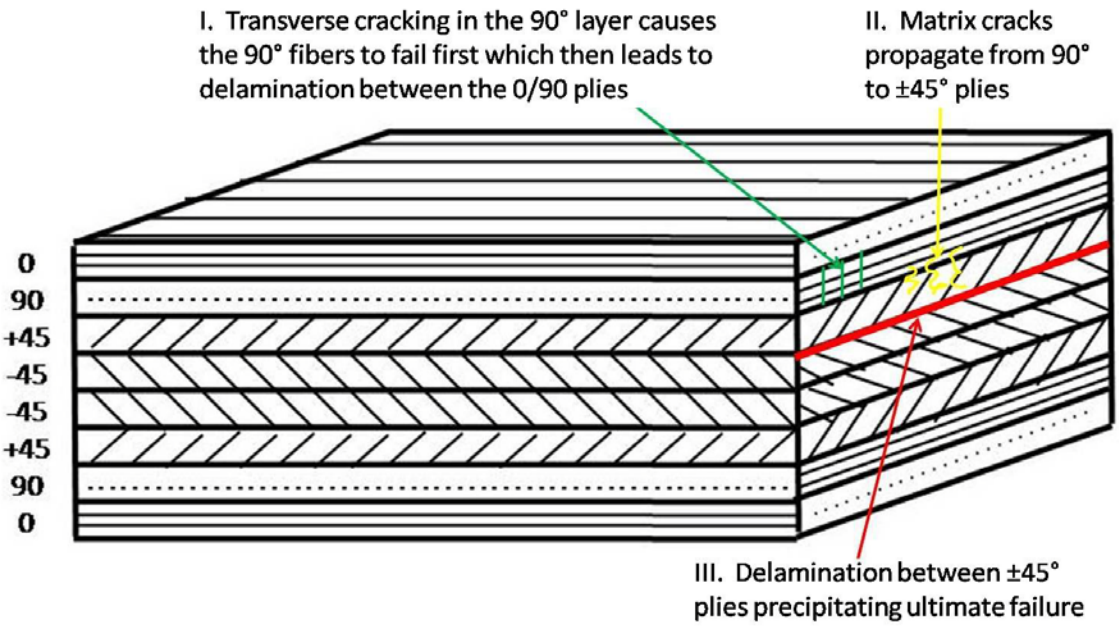

Figure 46. Failure Mechanism

5.3 Recommendations for Future Work

This research is the first step in the study of conductive nanocomposites for use in satellite structure applications. Continued research into materials other than nickel nanostrands™ for use in conductive nanocomposites is imperative to provide the best possible nanocomposite material combination for this application. This would lead to a broader sample size for comparisons and would lend itself to a better grasp of the significance of the research. The next step forward in this research effort is to perform fatigue tests on all samples and see how that affects the ESD and EMI shielding protection capabilities of the M55J/RS-3 nickel nanostrand™ composite configurations.

Appendix A: Stress-Strain Curves of 15.25 cm (6 in) Specimens

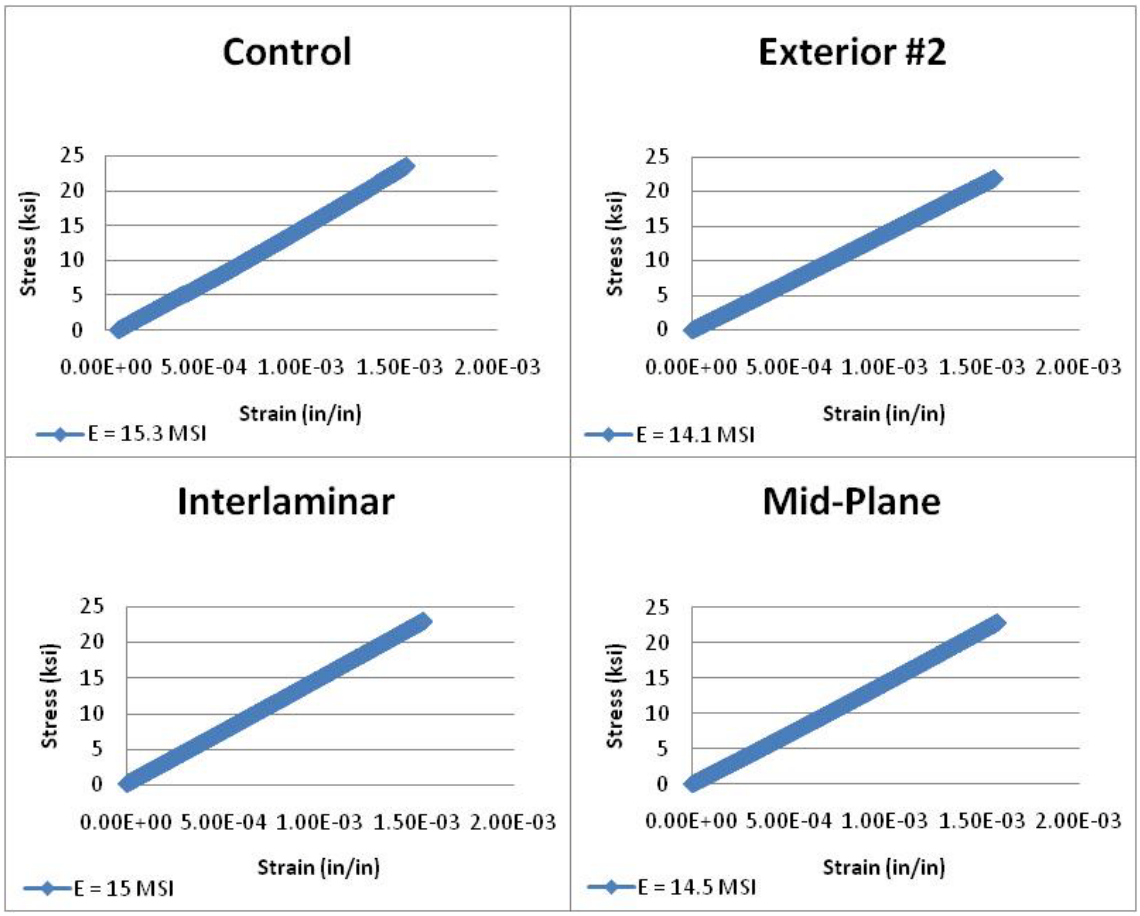

Figure 47. Stress-Strain Curves of 15.25 cm (6 in) Specimens at 159 MPa (23 ksi)

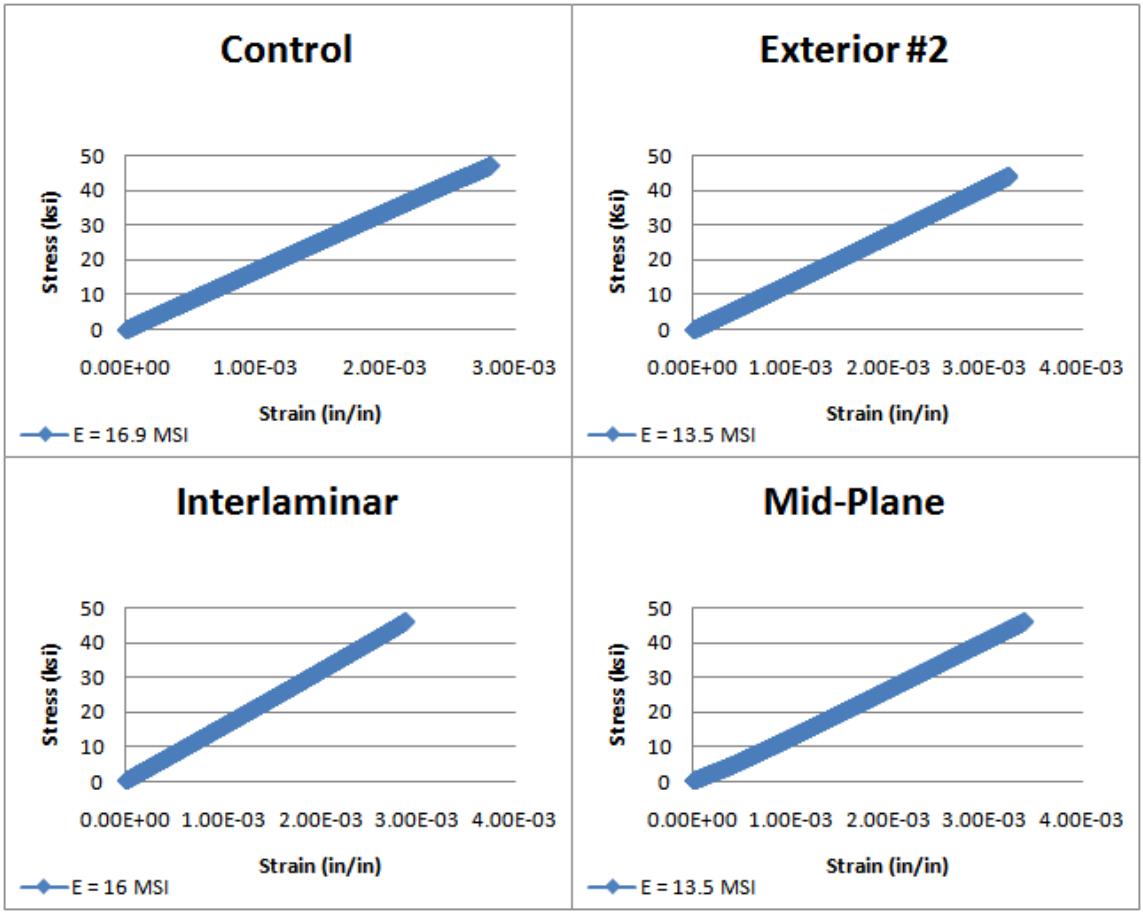

Figure 48. Stress-Strain Curves of 15.25 cm (6 in) Specimens at 324 MPa (47 ksi)

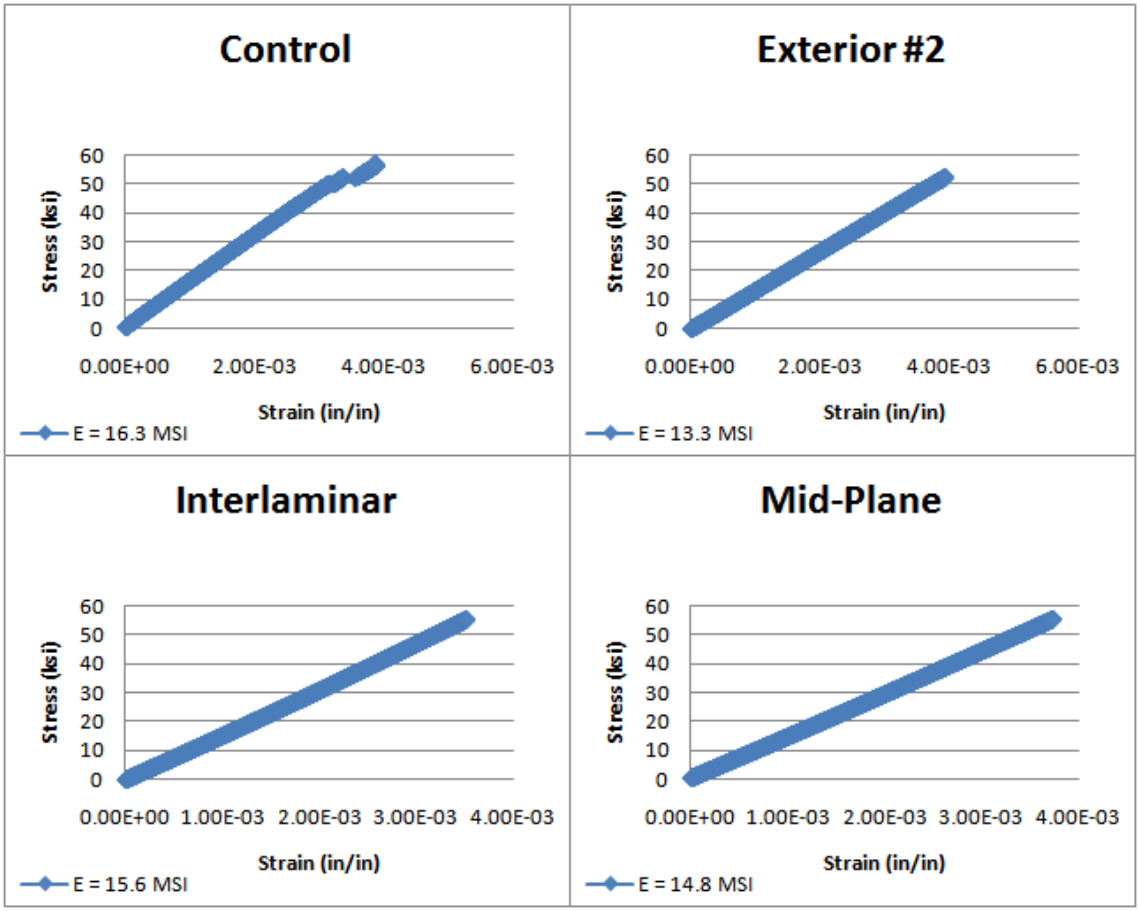

Figure 49. Stress-Strain Curves of 15.25 cm (6 in) Specimens at 386 MPa (56 ksi)

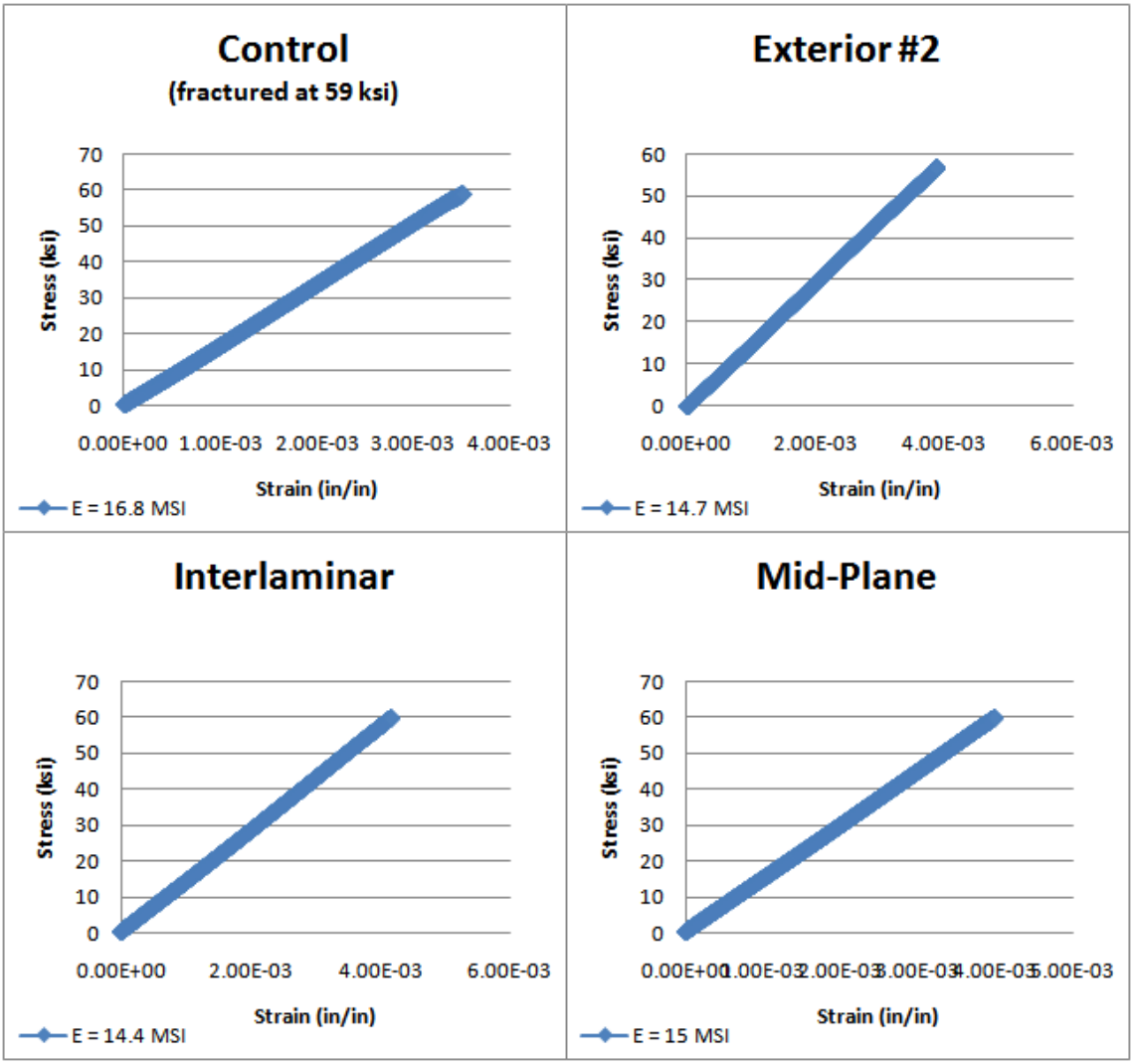

Figure 50. Stress-Strain Curves of 15.25 cm (6 in) Specimens at 407 MPa (59 ksi)

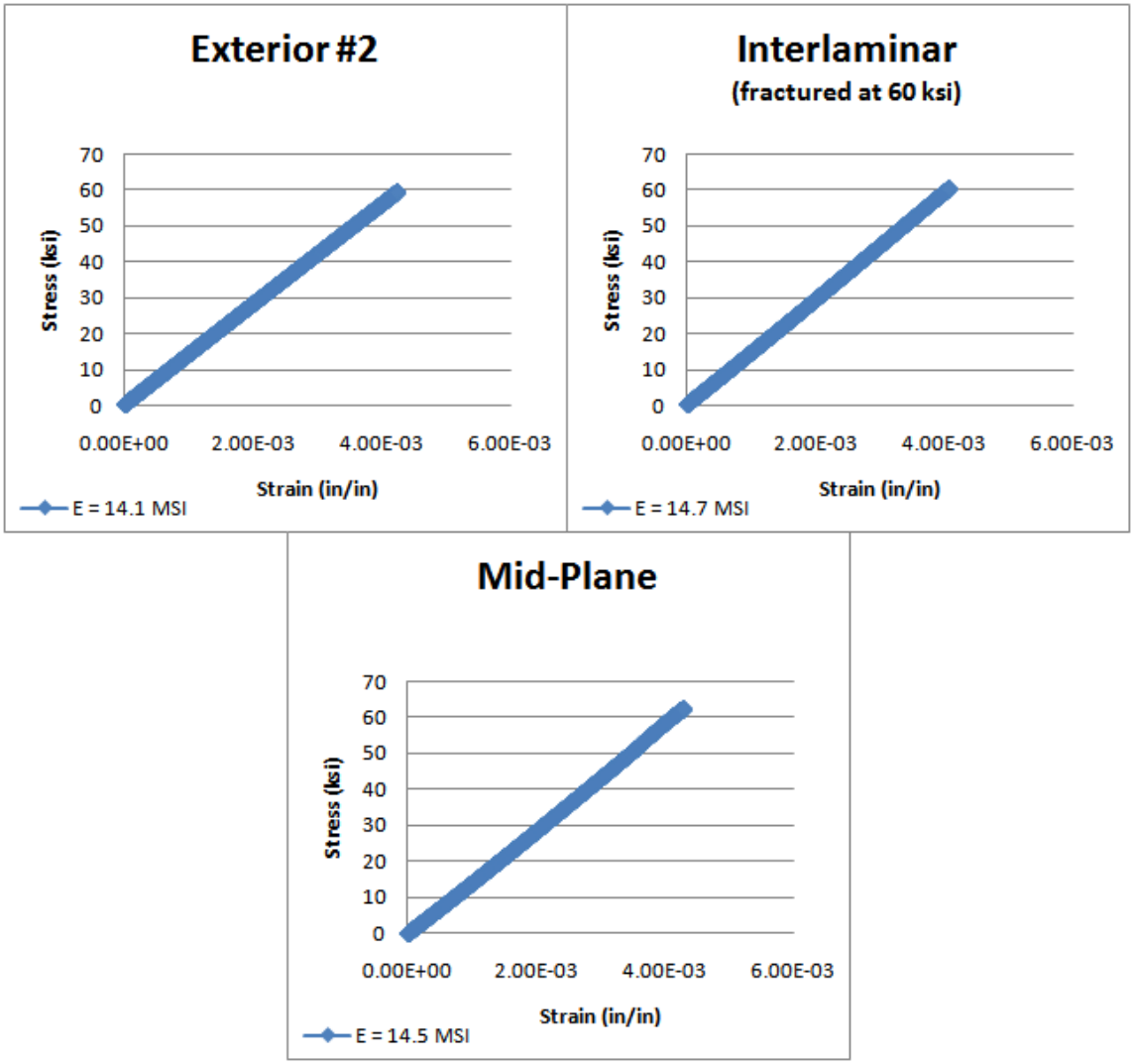

Figure 51. Stress-Strain Curves of 15.25 cm (6 in) Specimens at 427 MPa (62 ksi)

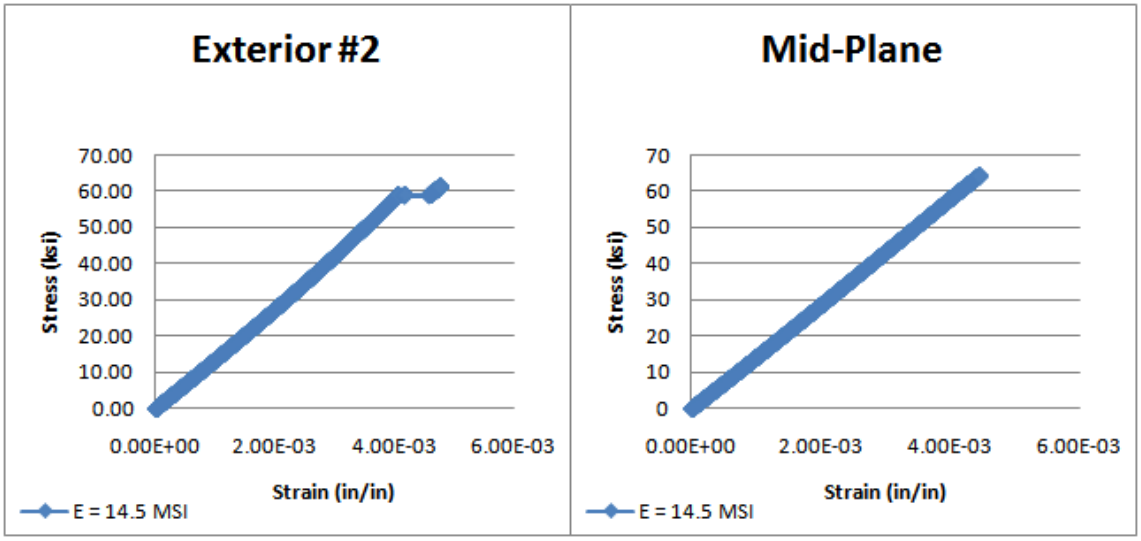

Figure 52. Stress-Strain Curves of 15.25 cm (6 in) Specimens at 441 MPa (64 ksi)

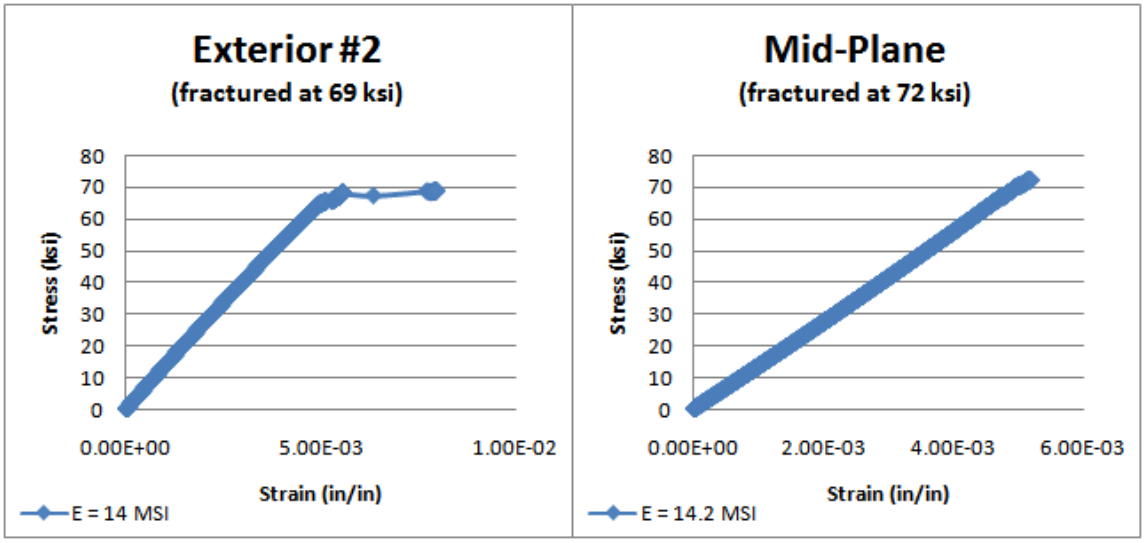

Figure 53. Stress-Strain Curves of 15.25 cm (6 in) Specimens to Failure (476 MPa (69 ksi) and 496 MPa (72 ksi)

Appendix B: Stress-Strain Curves of 7.62 cm (3 in) Specimens

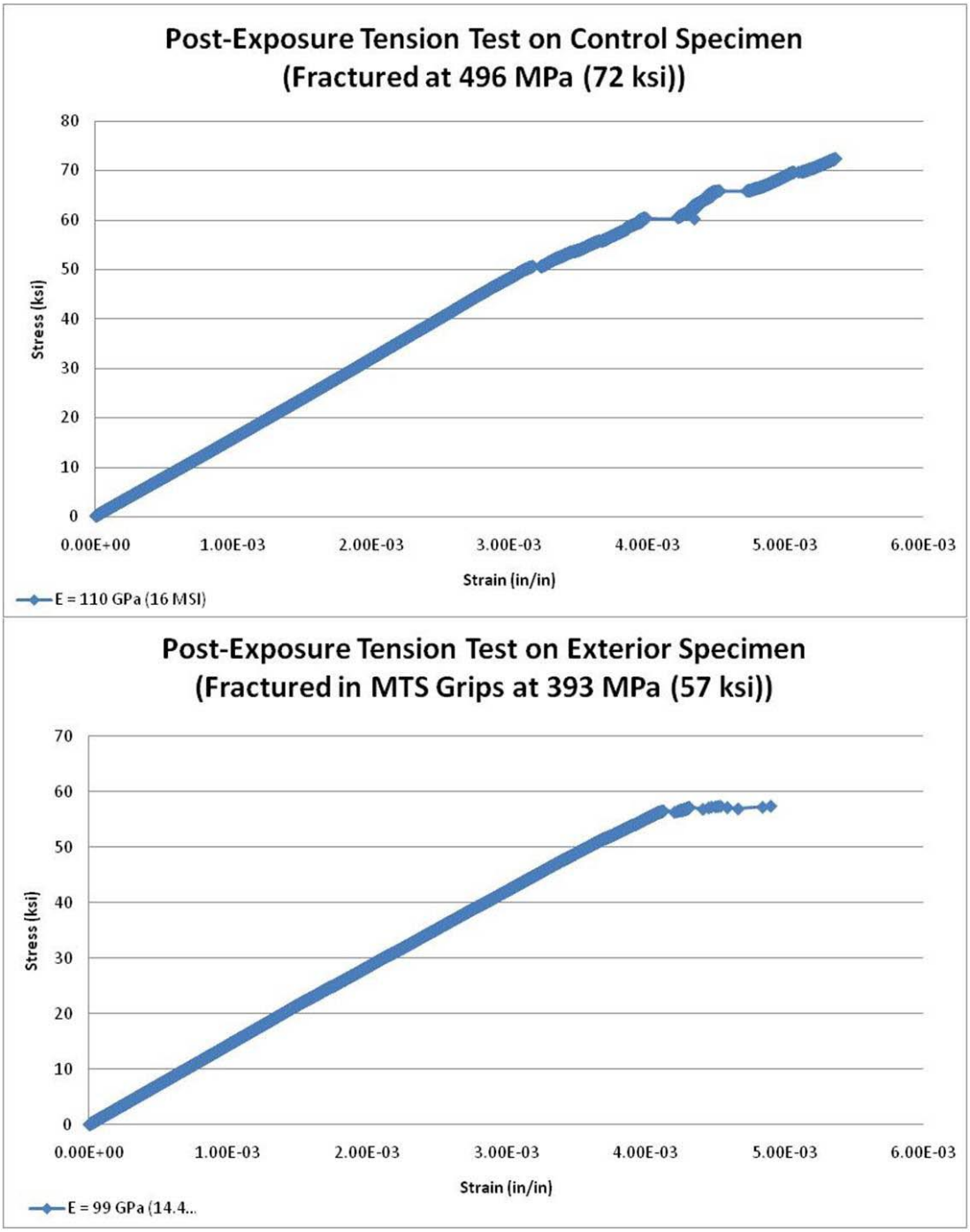

Figure 54. Stress-Strain Curves of Control & Exterior 7.62 cm Specimens

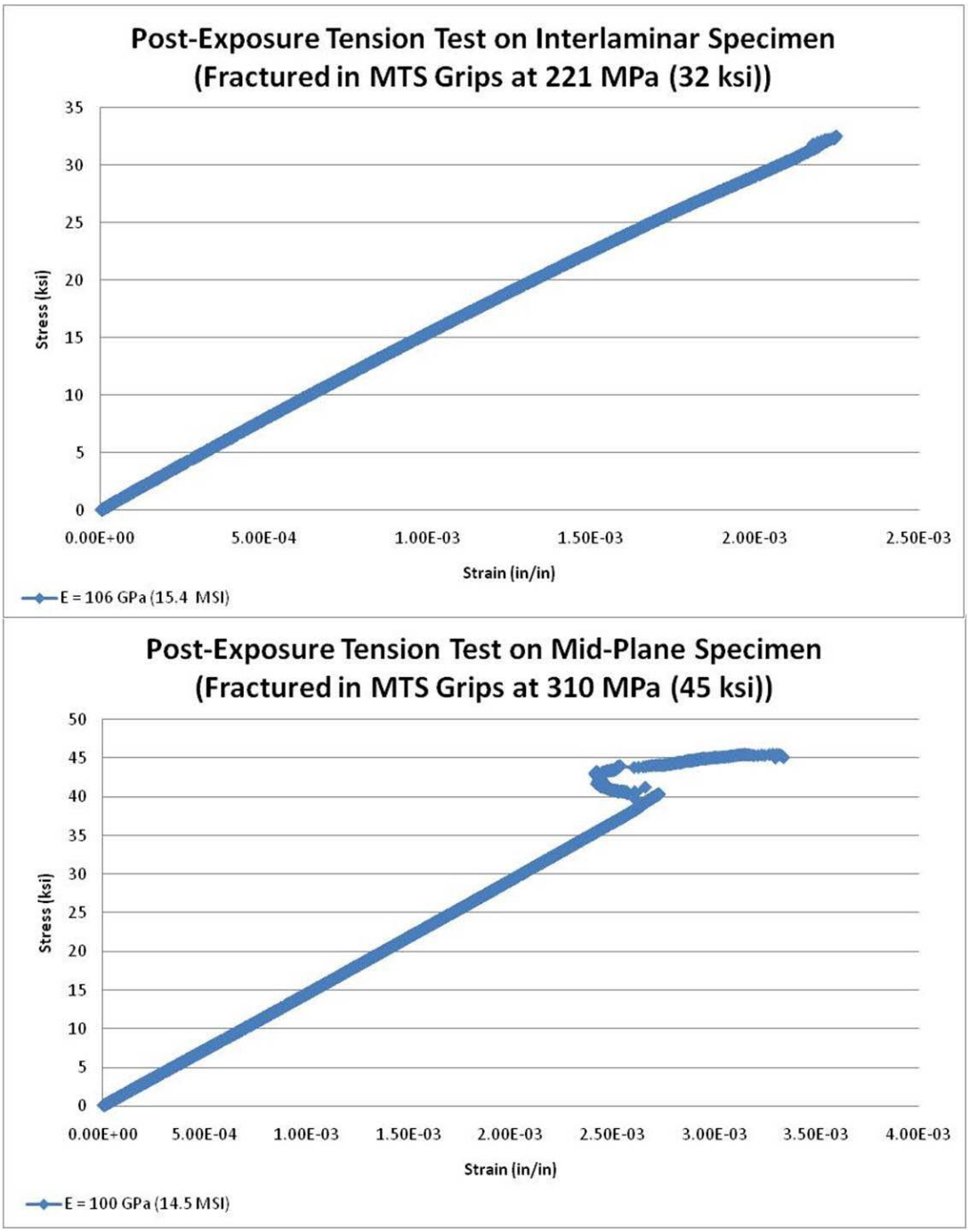

Figure 55. Stress-Strain Curves of Interlaminar & Mid-Plane 7.62 cm Specimens

Appendix C: Additional SEM Micrographs and Photos

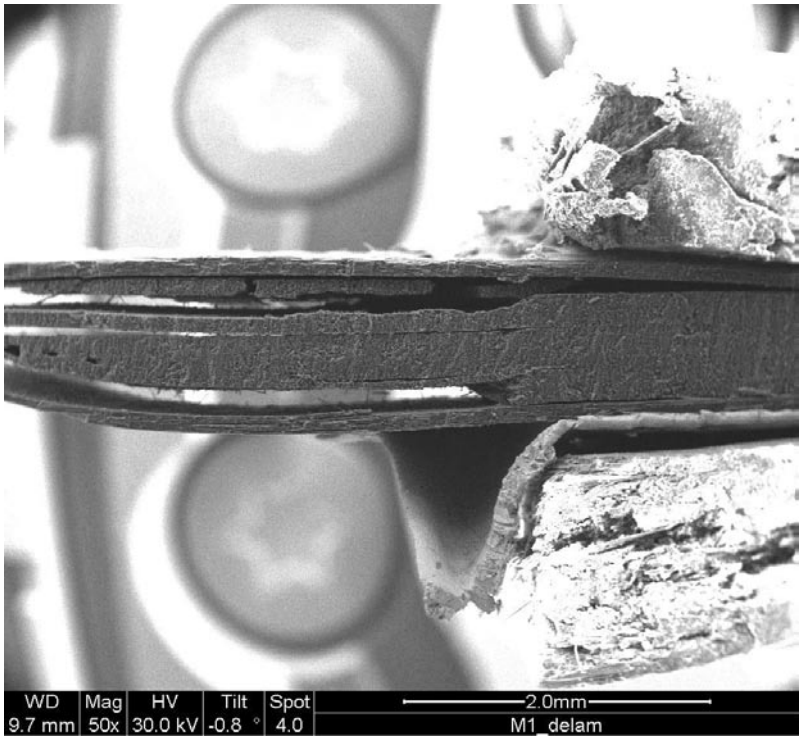

Figure 56. Fracture Surface of 15.25 cm Control Specimen, 50x

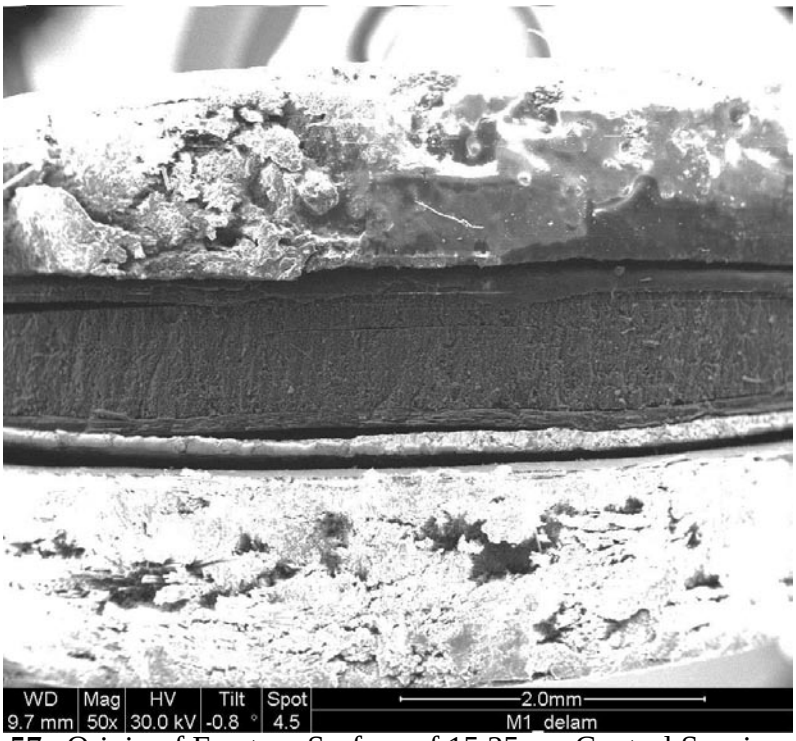

Figure 57. Origin of Fracture Surface of 15.25 cm Control Specimen, 50X

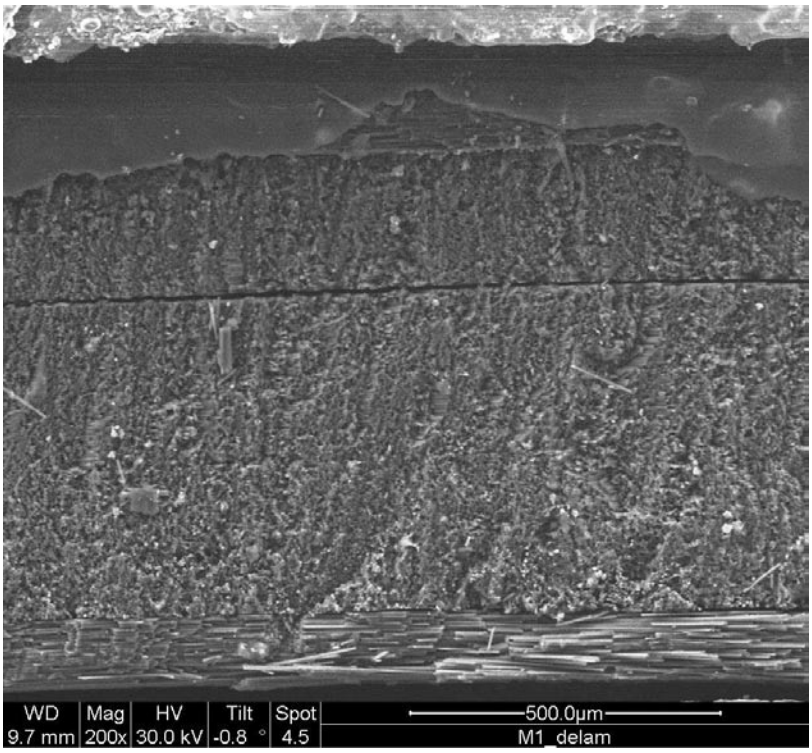

Figure 58. Origin of Fracture Surface of 15.25 cm Control Specimen, 200X

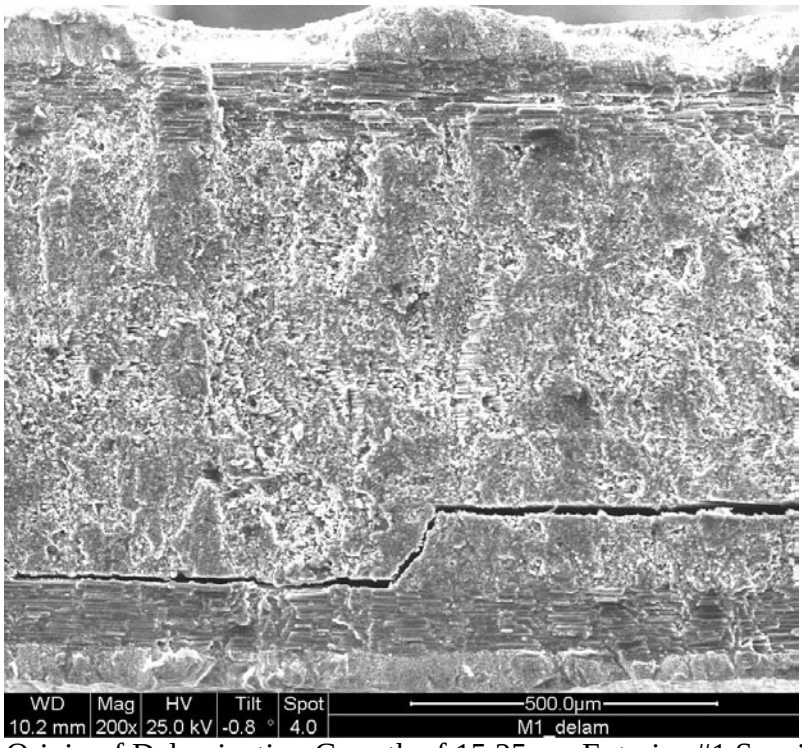

Figure 59. Origin of Delamination Growth of 15.25 cm Exterior #1 Specimen, 200X

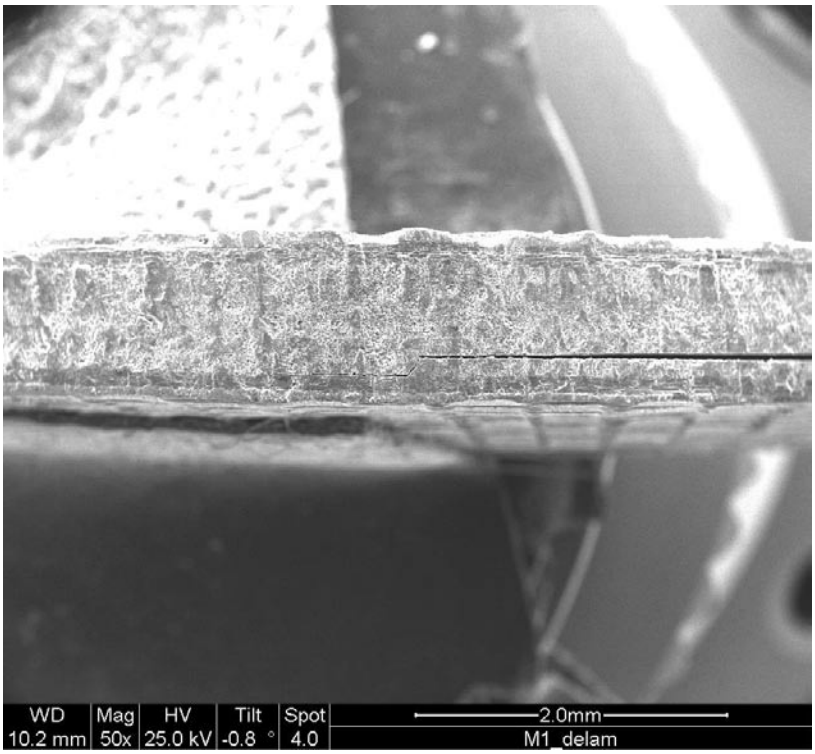

Figure 60. Origin of Delamination Growth of 15.25 cm Exterior #1 Specimen, 50X

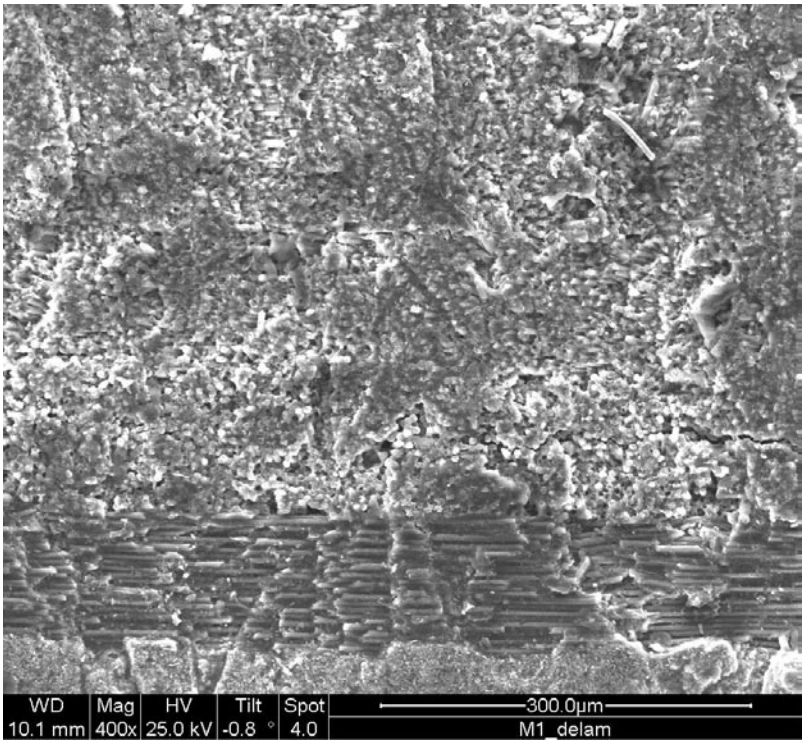

Figure 61. Origin of Failure of 15.25 cm Exterior #1 Specimen, 400X

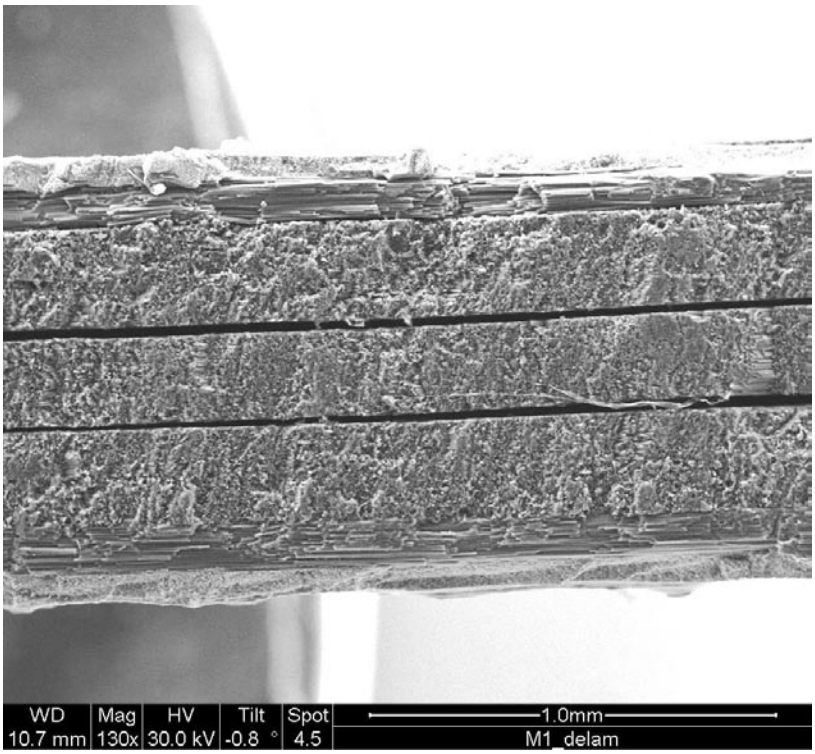

Figure 62. Delamination of 15.25 cm Exterior #2 Specimen, 130X

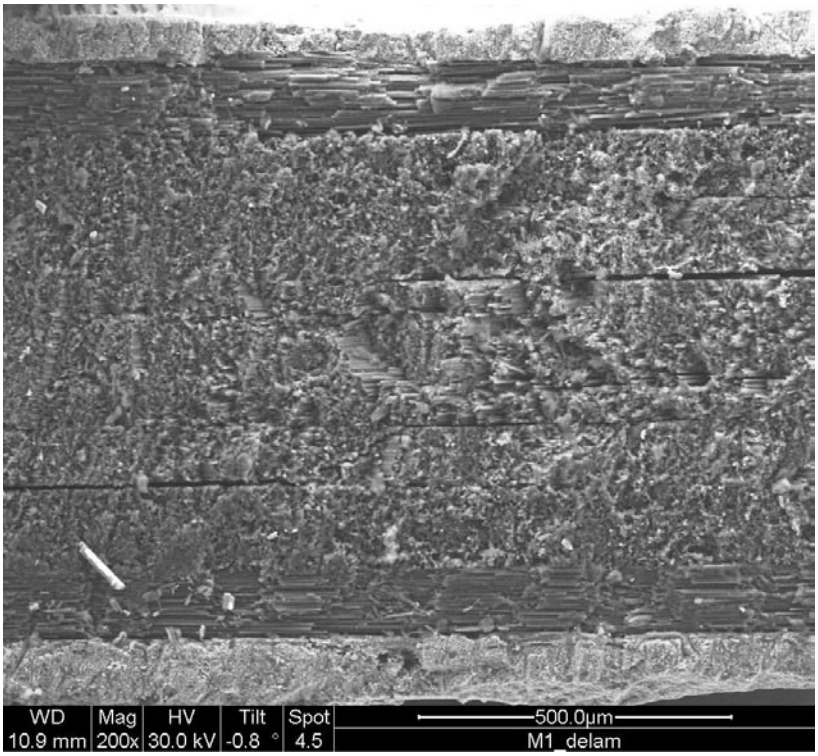

Figure 63. Matrix Cracks & Delamination of 15.25 cm Exterior #2 Specimen, 200X

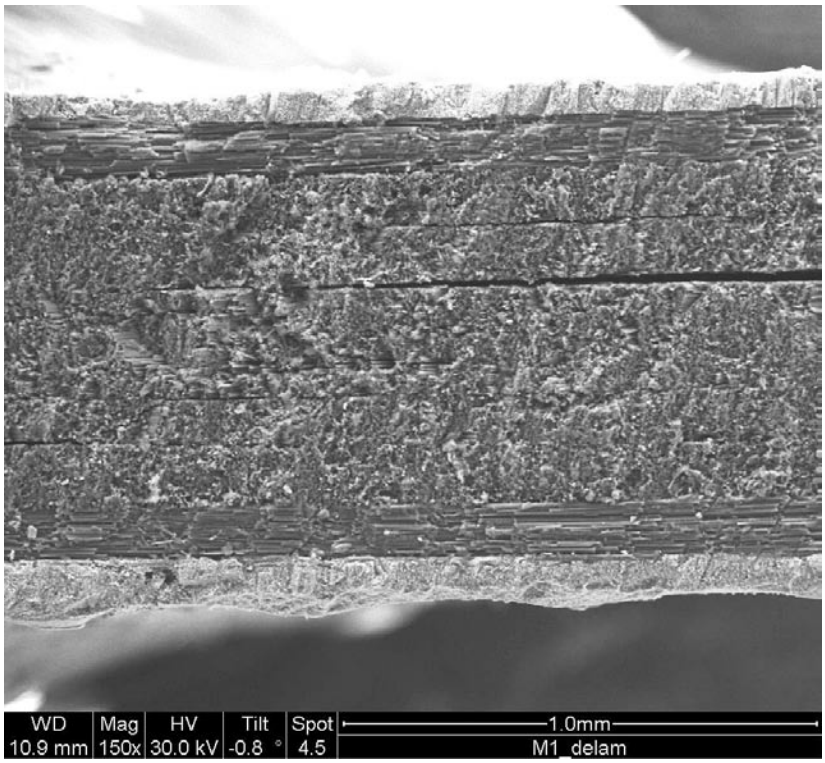

Figure 64. Origin of Failure of 15.25 cm Exterior #2 Specimen, 150X

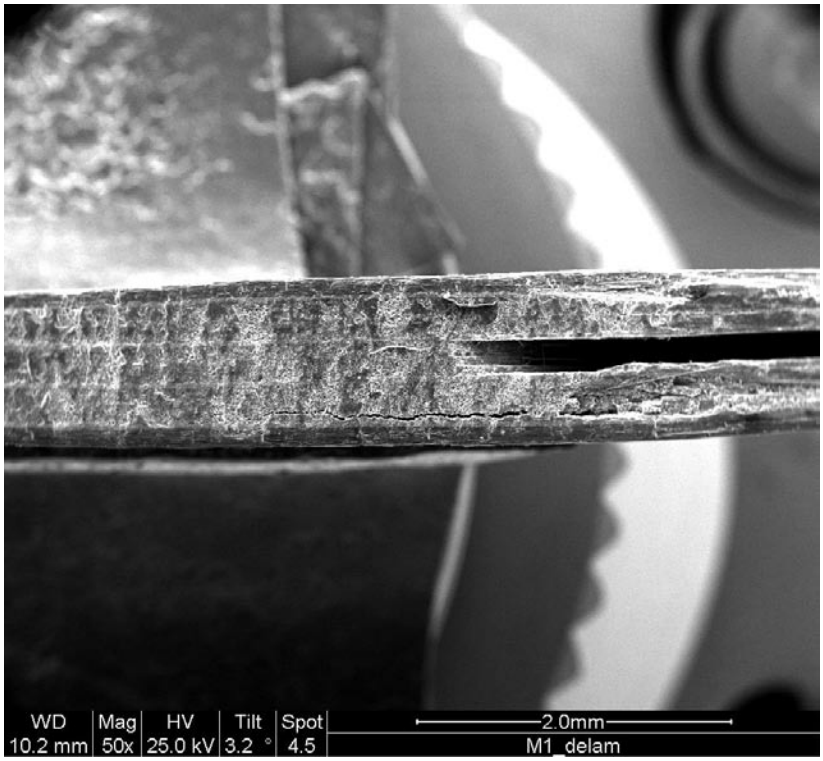

Figure 65. Fracture Surface of 15.25 cm Interlaminar Specimen, 50X

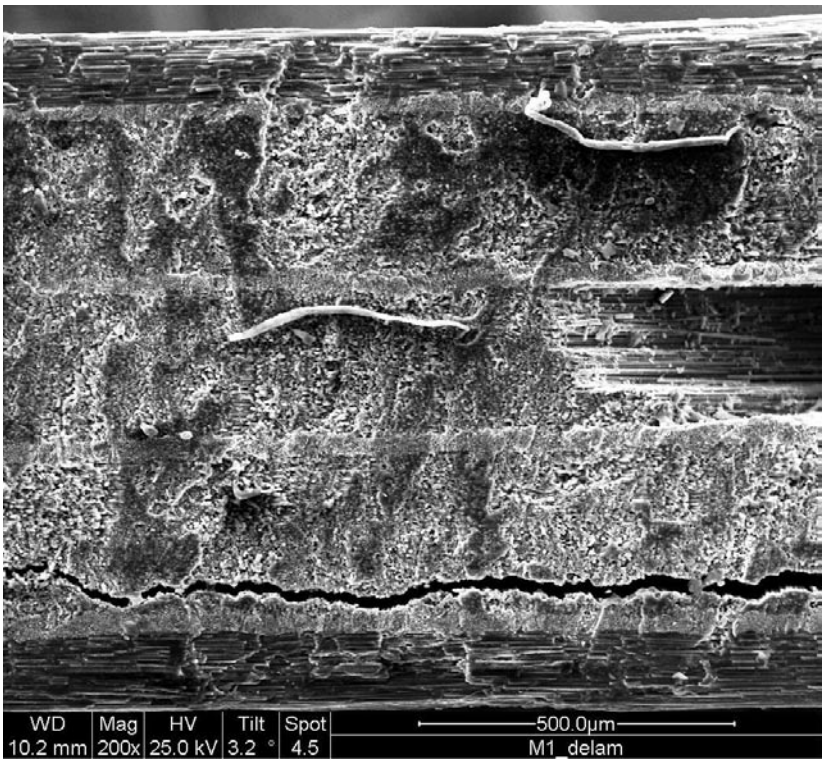

Figure 66. Fracture Surface of 15.25 cm Interlaminar Specimen, 200X

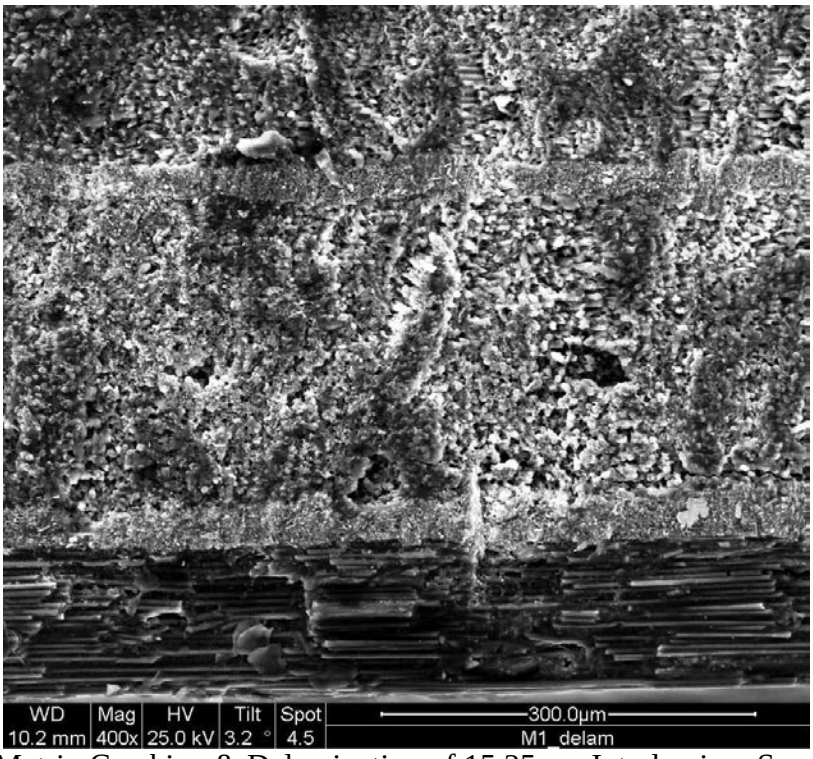

Figure 67. Matrix Cracking & Delamination of 15.25 cm Interlaminar Specimen, 400X

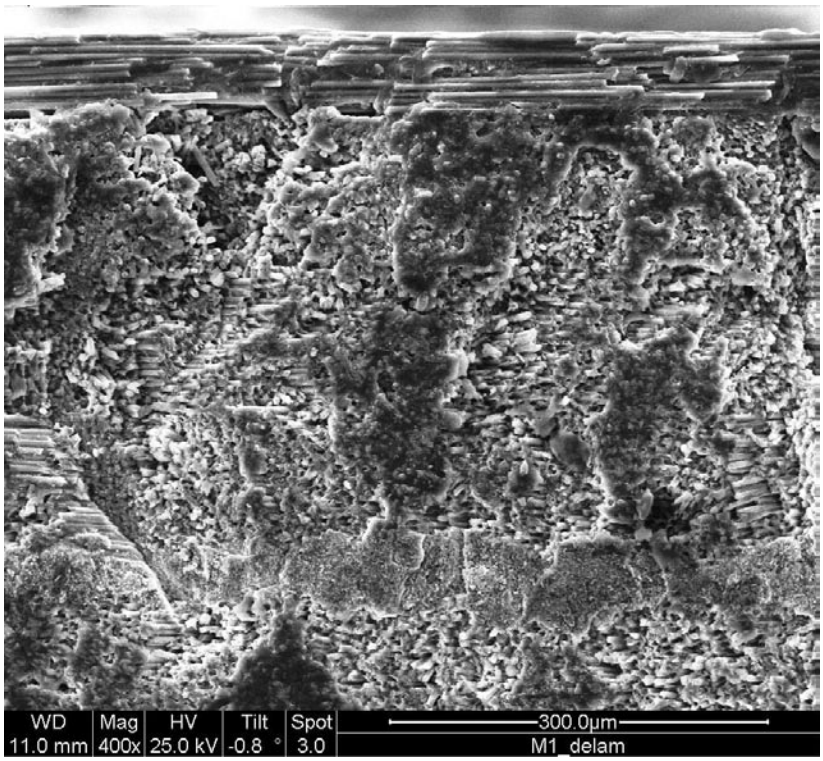

Figure 68. Matrix Cracking & Delamination of 15.25 cm Mid-Plane Specimen, 400X

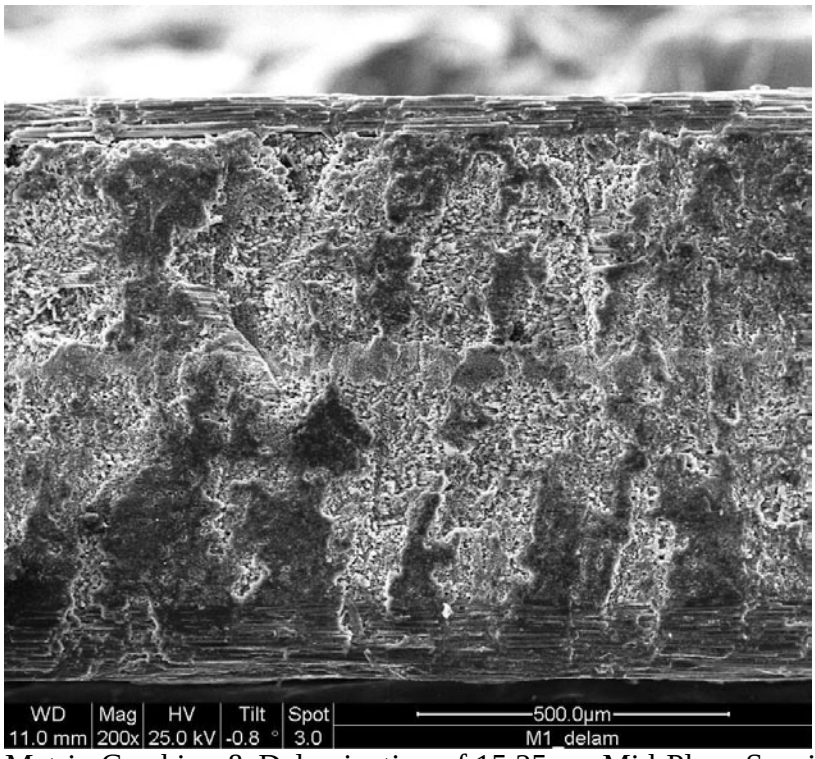

Figure 69. Matrix Cracking & Delamination of 15.25 cm Mid-Plane Specimen, 200X

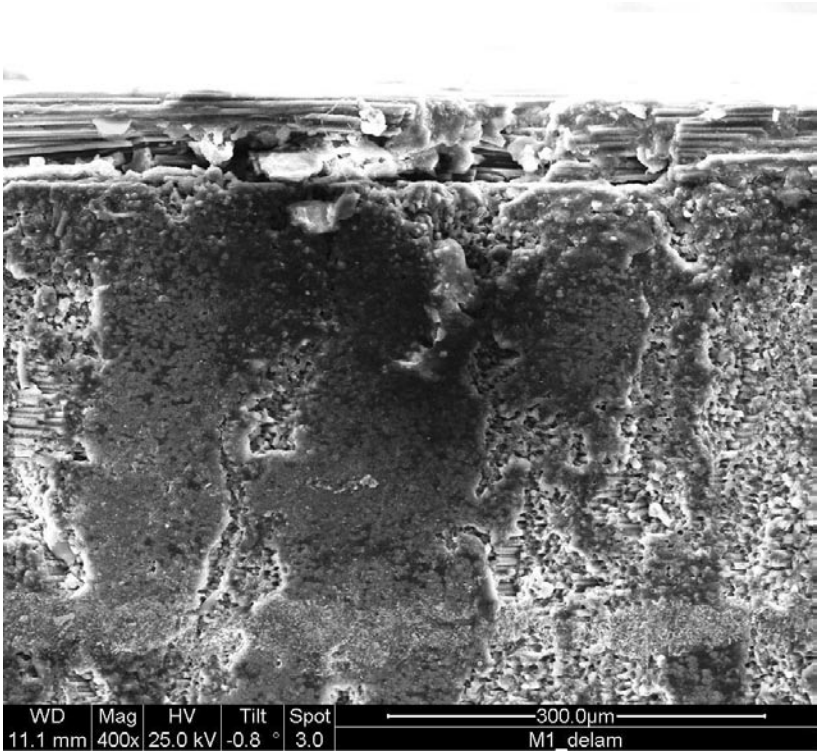

Figure 70. Matrix Cracking of 15.25 cm Mid-Plane Specimen, 400X

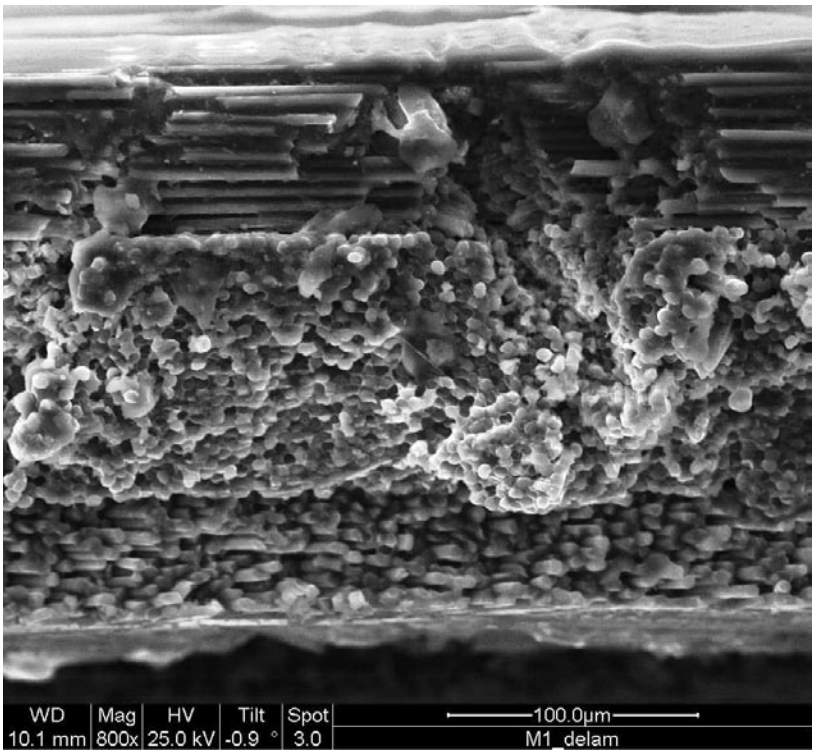

Figure 71. Fiber Failure of 15.25 cm Mid-Plane Specimen, 800X

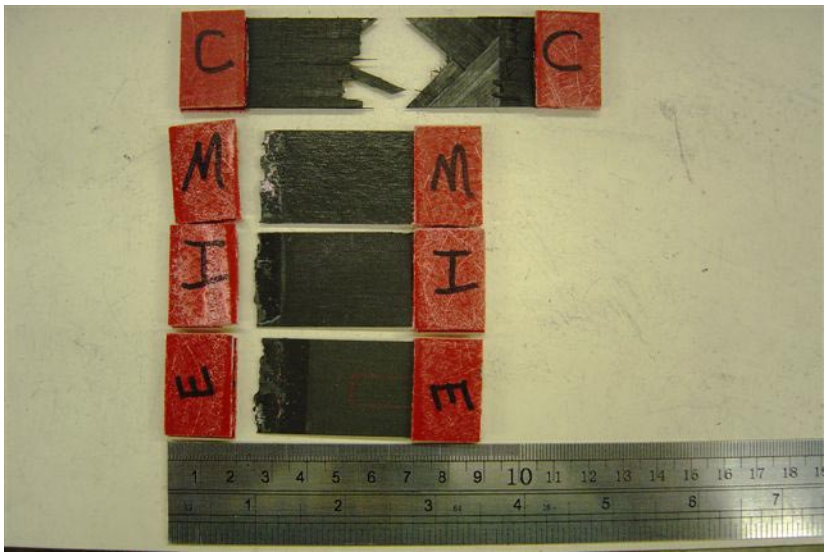

Figure 72. Fracture of 7.62 cm Irradiated Specimens

Bibliography

[1] M. D. Alexander. Nickel Nanostrands™ Expand Nanotechnology Engineering Capabilities. Available: http://www.afrl.af.mil.

[2] M. D. Alexander, H. Dowty, B. Black, C. Cerbus, J. Henes, G. Hansen, D. Widdof and M. Pettit, "Fabrication and Space Testing of Conductive Nanocomposites Containing Carbon Nanofibers and Ni Nanostrands," in *NSMMS Meeting,* 2006.

[3] D. F. Bahr, H. Kung, N. R. Moody and K. J. Wahl, *Mechanical Properties Derived from Nanostructuring Materials.* Pennsylvania: Materials Research Society, 2003.

[4] K. L. Bedingfield, R. D. Leach and M. D. Alexander, "Spacecraft Systems Failures and Anomalies Attributed to the Natural Space Environment," *NASA Reference Publication 1390,* 1996.

[5] L. Capes, E. Valentin, S. Esnouf, A. Ribayrol, O. Jost, A. Filoramo and J. N. Patillon, "High Yield Non-Destructive Purification of Single Wall Carbon Nanotubes Monitored by EPR Measurements," in *IEEE Conference on Nanostructures,* 2002, pp. 439-442.

[6] M. Chipara, D. L. Edwards, R. S. Benson and S. Philips, "Materials for space applications," in *MRS Symposium Proceedings Volume 851,* 2004.

[7] I. M. Daniel and O. Ishai, *Engineering Mechanics of Composite Materials.* , Second ed. New York: Oxford University Press, 2006, pp. 265-266.

[8] N. E. Dowling, *Mechanical Behavior of Materials.* New Jersey: Prentice Hall, 2007.

[9] J. R. Gaier, United States and National Aeronautics and Space Administration, *Prospects for using Carbon-Carbon Composites for EMI Shielding.* Washington, DC; Springfield, Va: National Aeronautics and Space Administration; For sale by the National Technical Information Service, 1990.

[10] J. R. Gaier, United States and National Aeronautics and Space Administration, *Intercalated Graphite Fiber Composites as EMI Shields in Aerospace Structures.* Washington, DC; Springfield, Va: National Aeronautics and Space Administration; National Technical Information Service, distributor, 1990.

[11] D. Gay, S. V. Hoa and S. W. Tsai, *Composite Materials Design and Applications.* New York: CRC Press, 2003.

[12] K. Green, J. Petrosky, D. Weeks and W. Carlos, "Identification of Gallium-Related Electron Paramagnetic Resonance in GaN Following 1.0 MeV Electron Irradiation," *Journal of Electronics,* 2006.

[13] G. Hansen, "High Aspect Ratio Sub-Micron and Nano-scale Metal Filaments," *SAMPE Journal,* vol. 41, 2005.

[14] G. Harris, J. Lennhoff, J. Nassif, M. Vinciguerra, P. Rose, D. Jaworski and J. Gaier, "Lightweight Highly Conductive Composites for EMI Shielding," *SAMPE Journal.,* vol. 36, pp. 59-63, 2000.

[15] H. Helvajian and E. Y. Robinson, *Micro- and Nanotechnology for Space Systems.* Los Angeles: The Aerospace Press, 1997.

[16] S. Ijima, "Helical Microtubules of Graphitic Carbon," *Nature Physics,* vol. 354, pp. 56-58, 1991.

[17] E. F. Knott, J. F. Shaeffer and M. T. Tuley, *Radar Cross Section.* Boston: Artech House, 1993.

[18] H. Lee, S. Mall, V. Nalladega, S. Sathish, A. Roy and K. Lafdi, "Characterization of Carbon Nanofiber Reinforced Epoxy Composite using Nanoindentation and AFM/UFM Techniques," *Polymer Composites,* vol. 14, pp. 549-562, 2006.

[19] N. Li, Y. Huang, F. Du, X. He, X. Lin, H. Gao, Y. Ma, F. Li, Y. Chen and P. C. Eklund, "Electromagnetic Interference (EMI) Shielding of Single-Walled Carbon Nanotube Epoxy Composites," *Nano Letters,* vol. 6, pp. 1141-1145, 2006.

[20] S. Mall, "Properties and Performance of Laminated Polymer Matrix Composites," in *Composites Engineering Handbook* P. K. Mallick, Ed. New York: Mercel Dekker, 1997, pp. 813-890.

[21] J. W. Molyneux-Child, "RFI/EMI Shielding Materials," *EMC Shielding Materials,* Boston: Newnes, 1997, pp. 175.

[22] D. G. Moris, *Mechanical Behavior of Nanostructured Materials.* New Hampshire: Trans Tech Publications, 1998.

[23] H. S. Nalwa, *Nanostructured Materials and Nanotechnology.* New York: Academic Press, 2002.

[24] S. P. Rawal, "Multifunctional Carbon Nanocomposite Coatings for Space Structures," in *AIAA SDM Conference,* 2006.

[25] S. P. Rawal and F. M. Kustas, "Evaluation of Carbon Nanofiber-Based Coating and Adhesives," *SAMPE Journal,* 2006.

[26] S. P. 1. Rea, D. 1. Wylie, D. 1. Linton, E. Orr and J. McConnell, "EMI shielding of woven carbon fibre composites," in *2004 High Frequency Postgraduate Student Colloquium,* 2004, pp. 205-10.

[27] M. J. Schulz, A. D. Kelkar and M. J. Sundaresan, *Nanoengineering of Structural, Functional, and Smart Materials.* New York: CRC Press, 2005.

[28] J. J. Sellers, *Understanding Space.* New York: McGraw-Hill, 2005, pp. 3-5, 79-89, 674-681.

[29] E. Silverman, "Space Environmental Effects on Spacecraft: LEO Materials Selection Guide," NASA, Tech. Rep. CR-4661, 1995.

[30] K. Strong and E. Silverman, "Nanocomposite Applications in On-Orbit Systems," in *NSMMS Meeting,* July 2006.

[31] T. F. Tascione, *Introduction to the Space Environment.* Florida: Krieger Publishing Company, 1994, pp. 133-144.

[32] W. 1. Zeng and S. T. 1. Tan, "Preparation and EMI shielding properties of nickel-coated PET fiber filled epoxy composites," *Polymer Composites,* vol. 27, pp. 24-9, 02. 2006.

Vita

Captain Benjamin T. Harder graduated from Tokay High School in Lodi, California. He entered undergraduate studies at the Georgia Institute of Technology in Atlanta, Georgia where he graduated with a Bachelor of Science degree in Materials Engineering in June 1999. He was commissioned through the Detachment 165 AFROTC at the Georgia Institute of Technology.

His first assignment was at Pensacola NAS as a student in Joint Navigator Training in August 1999. In May 2001, he was assigned to the Air Force Research Laboratory, Airbase Technologies Division, Tyndall AFB, Florida where he served as project officer on multiple research and development programs. In May 2004, he was assigned to the Ogden Air Logistics Center, Hill AFB, Utah where he served as a secondary power systems engineer on the F-16 followed by the position of Executive Officer to the Engineering Directorate. In August 2006, he entered the Graduate School of Engineering and Management, Air Force Institute of Technology. Upon graduation, he will be assigned to the Materials and Manufacturing Directorate of the Air Force Research Laboratory.

REPORT DOCUMENTATION PAGE

Form Approved
OMB No. 0704–0188

1. REPORT DATE (DD–MM–YYYY)	2. REPORT TYPE	3. DATES COVERED *(From — To)*
19-06-2008	Master's Thesis	August 2006 — June 2008

4. TITLE AND SUBTITLE

Evaluation of Nanocomposites as Lightweight Electronic Enclosures for Satellites' Applications

5a. CONTRACT NUMBER

5b. GRANT NUMBER

5c. PROGRAM ELEMENT NUMBER

6. AUTHOR(S)

Benjamin T. Harder, Captain, USAF

5d. PROJECT NUMBER

5e. TASK NUMBER

5f. WORK UNIT NUMBER

7. PERFORMING ORGANIZATION NAME(S) AND ADDRESS(ES)

Air Force Institute of Technology
Graduate School of Engineering and Management (AFIT/EN)
2950 Hobson Way
WPAFB OH 45433-7765

8. PERFORMING ORGANIZATION REPORT NUMBER

AFIT/GMS/ENY/08-J01

9. SPONSORING / MONITORING AGENCY NAME(S) AND ADDRESS(ES)

Intentionally Left Blank

10. SPONSOR/MONITOR'S ACRONYM(S)

11. SPONSOR/MONITOR'S REPORT NUMBER(S)

12. DISTRIBUTION / AVAILABILITY STATEMENT

APPROVED FOR PUBLIC RELEASE; DISTRIBUTION UNLIMITED

13. SUPPLEMENTARY NOTES

14. ABSTRACT

The United States military is exploring the use of nanocomposite materials for satellite structural applications. Current composite spacecraft structures are nonconductive and must have expensive shielding materials applied in order to protect the spacecraft from catastrophic damage that can be caused by electromagnetic interference (EMI) and/or electrostatic discharge (ESD) which are characteristics of the space environment. Conductive nanocomposites are being developed for spacecraft structures that will provide ESD and EMI shielding protection without the need for expensive secondary shielding materials. This thesis studied one such material consisting of M55J/RS-3 composite combined with nickel nanostrands™. Four different configurations were tested for their ultimate tensile strength (UTS) and EMI shielding properties before and after exposure to the space environment. The four configurations tested were a baseline panel consisting of M55J/RS-3 and three configurations with different layers of nickel nanostrands™ added to the control specimen: exterior, interlaminar, and mid-plane. These four were further tested for their EMI and resistivity properties before, during and after monotonic tension tests of increasing loads up to fracture. This study found that the UTS and Young's modulus (E) do not change after exposure to the space environment, EMI shielding of the exterior specimen is 25% better than the control specimen, sheet resistance measurements show that exterior specimens are 11% better at ESD protection than the control, and failure mechanisms are the same regardless of composite configuration: The 90° plies failed first, causing delamination in the 0/90 plies leading to transverse matrix cracking and delamination in the ±45 plies resulting in ultimate failure, and in all configurations the nanostrand layers were not damaged.

15. SUBJECT TERMS

Nanocomposites, Space Environment Protection, Monotonic Tension Testing, Composite Satellite Structures, Nickel Nanostrands™, Conductivity, Electromagnetic Interference Protection, Electrostatic Discharge Protection

16. SECURITY CLASSIFICATION OF:			17. LIMITATION OF ABSTRACT	18. NUMBER OF PAGES	19a. NAME OF RESPONSIBLE PERSON
a. REPORT	b. ABSTRACT	c. THIS PAGE			Shankar Mall, Ph.D.
U	U	U	UU	98	19b. TELEPHONE NUMBER (Include Area Code) (937) 255-3636, ext 4587; e-mail: Shankar.Mall@afit.edu